

Carnegie Mellon University

CARNEGIE INSTITUTE OF TECHNOLOGY

THESIS

SUBMITTED IN PARTIAL FULFILLMENT OF THE REQUIREMENTS

FOR THE DEGREE OF Doctor of Philosophy

TITLE Surfactant Mediated Tipstreaming as a Tool for Designed

Production of Sub-Micron Sized Droplets

PRESENTED BY Todd Moyle

ACCEPTED BY THE DEPARTMENT OF

Chemical Engineering

SHELLEY ANNA 4/24/2015

CO-ADVISOR DATE

LYNN WALKER 4/24/2015

CO-ADVISOR DATE

LORENZ BIEGLER 4/24/2015

DEPARTMENT HEAD DATE

APPROVED BY THE COLLEGE COUNCIL

VIJAYAKUMAR BHAGAVATULA 4/24/2015

DEAN DATE

Surfactant Mediated Tipstreaming as a Tool for Designed Production of Sub-Micron Sized Droplets

Submitted in partial fulfillment of the requirements for

The degree of

Doctor of Philosophy

In

The Department of Chemical Engineering

Todd M. Moyle

B.S. Chemical Engineering, University of Pittsburgh

Carnegie Mellon University

Pittsburgh, PA

April, 2015

ACKNOWLEDGEMENTS

First, I would like to thank my wife, Nichole, for her help and constant support during the often stressful time as a graduate student. She is always able to cheer me up and encourage me when I need it most. Her input, ideas, and suggestions have added greatly to my research. I am very lucky to have her and could not have done this without her.

I also want to thank my parents, Bette and David Moyle, for their support and encouragement to always do my best and work my hardest. I would like to thank all of the colleagues I've worked with over the past 5 years for teaching me new techniques and for giving me suggestions on various problems. Specifically, I want to thank Matt Reichert for teaching me proper laboratory techniques and Stephanie Kirby for being there to lend a hand when I needed it. Also, I want to thank everyone in the CFE office for making it a great place to work.

I would like to thank my advisors Shelley Anna and Lynn Walker for their guidance and suggestions through my graduate career. I have a great amount of respect and appreciation for everything I have learned from them. Lastly, I wish to thank Professors Bob Tilton, Aditya Khair, and Shawn Litster for serving on my thesis committee. Their input and ideas have been a useful guide for my research.

This work was financially supported by the National Science Foundation Grant no. CBET-1033814, the Thomas (E 1973) and Adrienne Klopach Graduate Fellowship in Engineering, and the Department of Chemical Engineering.

ABSTRACT

Microscale tipstreaming is a hydrodynamic phenomenon capable of producing submicron sized droplets within a microfluidic device. Tipstreaming is the ejection of small drops from a liquid thread formed by interfacial tension gradients and convective transport of surfactant. To use tipstreaming in potential applications, including nanoparticle synthesis, chemical detection and separation, occlusion therapy, and others, it is necessary to understand and be able to control the thread formation process. However, there are many technical challenges restricting successful implementation of microscale tipstreaming. This thesis provides several tools and solutions to overcome these technical challenges.

Modeling the tipstreaming phenomenon has allowed for prediction of conditions where tipstreaming is expected to occur for an arbitrary oil-water-surfactant system. This facilitates the use of tipstreaming to quickly estimate conditions where thread formation will be observed, reducing the need for experimentally determining the tipstreaming operating diagram. The key component of the model is the reliance on interfacial shape observations to simplify the fluid flow and surfactant transport equations. An active feedback control loop developed in this work is capable of eliminating the production of primary droplets and producing a continuous thread, and therefore a continuous droplet stream. Lastly, droplet size is characterized as a function of the surfactant concentration and liquid flow rates of the two phases leading to control over the size of the droplets being produced. Applying these tools to enhance tipstreaming is crucial in aiding its use in applications.

TABLE OF CONTENTS

ACKNOWLEDGEMENTS	ii
ABSTRACT	iii
TABLE OF CONTENTS	iv
LIST OF TABLES	vii
LIST OF FIGURES	viii
CHAPTER 1: INTRODUCTION	1
CHAPTER 2: BACKGROUND	6
2.1 APPLICATION AND PRODUCTION OF MICRON SIZED DROPLETS	6
2.2 TIPSTREAMING AND MICROSCALE TIPSTREAMING	10
2.3 MODELING INTERFACIAL DEFORMATIONS.....	15
2.4 ACTIVE CONTROL OF FLUID FLOW IN MICROFLUIDICS	18
CHAPTER 3: MATERIALS AND METHODS	31
3.1 DEVICE DESIGN AND FABRICATION.....	31
3.2 STEADY STATE TIPSTREAMING MATERIALS	37
3.3 CONTROLLER EQUIPMENT DESIGN AND MATERIALS.....	37
3.4 IMAGE ANALYSIS OF DROP SIZE	39
CHAPTER 4: A MODEL TO PREDICT OPERATING CONDITIONS FOR MICROSCALE TIPSTREAMING	44
4.1 INTRODUCTION	44
4.2 EXPERIMENTAL TIPSTREAMING OPERATING DIAGRAMS ..	45
4.3 MODELING INTERFACIAL FLOWS	48

4.4 PHYSICAL LIMITS APPLIED TO THE MODEL.....	60
4.4.1 GENERALIZED FRUMKIN EQUATION OF STATE	60
4.4.2 HENRY’S LAW FORMULATION	70
4.5 RESULTS AND DISCUSSION	73
4.6 CONCLUSIONS.....	79
CHAPTER 5: CONTROLLING THREAD FORMATION DURING TIPSTREAMING USING AN ACTIVE FEEDBACK CONTROL LOOP	85
5.1 INTRODUCTION	85
5.2 CONTROLLER DEVELOPMENT AND DESIGN	87
5.3 EXPERIMENTAL CONTROLLER OPTIMIZATION.....	92
5.4 RESULTS AND DISCUSSION	99
5.5 CONCLUSIONS.....	101
CHAPTER 6: REMOVAL OF PRIMARY DROPLETS GENERATED DURING TIPSTREAMING USING AN ON CHIP SEPARATOR	105
6.1 INTRODUCTION	105
6.2 BACKGROUND	107
6.3 MATERIALS AND SEPARATOR DESIGN	109
6.4 SEPARATOR RESULTS AND ANALYSIS	112
6.5 CONCLUSIONS.....	115
CHAPTER 7: TIPSTREAMING FROM THE REAR OF A DROPLET TRAVELING THROUGH A MICROCHANNEL	119
7.1 INTRODUCTION	119
7.2 EXPERIMENTAL METHODS AND DEVICE DESIGN.....	121

7.3 RESULTS AND DISCUSSION	124
7.3.1 ANALYSIS OF TIPSTREAMING FROM THE REAR OF A DROP	124
7.3.2 DEVELOPMENT OF OPERATING DIAGRAMS	133
7.4 CONCLUSIONS.....	138
CHAPTER 8: THE EFFECT OF OPERATING CONDITIONS ON THE SIZE OF DROPLETS GENERATED VIA TIPSTREAMING.....	143
8.1 INTRODUCTION	143
8.2 MATERIALS AND METHODS.....	147
8.3 RESULTS	149
8.3.1 OPTICAL MEASUREMENTS OF DROPLETS.....	149
8.3.2 MEASUREMENT OF HYDROGEL PARTICLES.....	158
8.4 DISCUSSION	163
8.5 CONCLUSIONS.....	167
CHAPTER 9: CONCLUSIONS	171
APPENDIX A: MATLAB CODE FOR THE TIPSTREAMING MODEL.....	176

LIST OF TABLES

Table 3.1. Geometry, fluid, and surfactant properties for microscale tipstreaming experiments reported here. Geometric dimensions are measured as described in the text. Viscosity and density values are as reported the by manufacturer. Surface tension and surfactant molecular properties are taken from (Alvarez, et al. 2012. JCIS)

Table 6.1 Separation efficiencies for each of the three flow rates tested. Percentages represent the percent of micron sized droplets which exited through the main exit channel.

LIST OF FIGURES

Figure 2.1 A series of images representing the four modes of droplet breakup observed within a flow focusing geometry including (a) geometry controlled, (b) microscale tipstreaming, (c) dripping, and (d) jetting. Reprinted with permission from Anna and Mayer, *Physics of Fluids*, Copyright 2006, AIP Publishing LLC.

Figure 3.1 (a) Schematic diagram of planar microfluidic flow focusing geometry. The continuous phase, mineral oil, flows into both of the outer channels with width w_c at a volumetric flow rate of $Q_c/2$. The dispersed phase liquid, water containing dissolved $C_{12}E_8$, flows into the inner channel with width $2a$ at a flow rate of Q_d . The three channels merge at a distance L upstream of the orifice. The two immiscible liquids flow together through the orifice with width w_{or} . The resulting droplet stream exits into an exit channel of width w_{out} . The entire device has a uniform depth h . (b) Image of interfacial shape, thread, and primary droplets during tipstreaming.

Figure 3.2 Light intensity profile for a droplet measured at the drop center. The solid line represents the measured light intensity profile, the \bullet points represents the measured droplet edges, and the $--$ line represents the average between the average background intensity and the minimum intensity, in this case zero. The inset is the image of the drop being analyzed. The ring indicates the fitted diameter based on the measured diameter.

Figure 4.1. Experimentally observed conditions corresponding to tipstreaming (\blacksquare) and non-tipstreaming break up modes (\square) as defined in the text at specific outer liquid flow rate and surfactant concentration values.

Figure 4.2. Schematic diagram illustrating the geometry used to model the interfacial shape during thread formation. The interfacial geometry and coordinate system are assumed to be axisymmetric about the center axis.

Figure 4.3. Simulated profiles for the interfacial tension and interfacial surfactant concentration along the conical interface with volumetric flow rate equal to $100 \mu\text{l}/\text{min}$ and bulk surfactant concentration equal to $7 \times 10^{-5} \text{ mol}/\text{l}$. All other parameters needed are reported in Table I. The inset schematically illustrates the effect of external flow on the surfactant concentration profile.

Figure 4.4. Boundary lines separating operating conditions that result in tipstreaming cone angles smaller than the lower limit, for three different hydraulic diameters of the flow focusing orifice. The region above and to the left of each line corresponds to cone apex angles below the lower limit. The remaining physicochemical properties correspond to the values listed in Table I.

Figure 4.5. Operating diagram depicting viable conditions for tipstreaming predicted by performing an interfacial mass balance and constrained by physical limits including device geometry considerations, a global surfactant mass balance, a global fluid mass balance, transition to jetting, and a minimum interfacial tension. Physicochemical parameters used correspond to those in Table I, and the $D_H = 60 \mu\text{m}$ case shown in Figure 4.4.

Figure 4.6. Comparison of predicted operating diagram for tipstreaming with conditions at which the tipstreaming mode of breakup is observed in experiments, shown in dimensional parameter space in Figure 4.1. Bulk concentration and flow rates are made dimensionless and defined in the text, and the predicted feasibility boundaries are estimated using the physicochemical parameters corresponding to the experiments and listed in Table I.

Figure 4.7. Approximate physical boundaries for the tipstreaming region obtained by linearizing the equation of state. The solid lines indicate the geometry boundary, the global surfactant mass balance boundary, and the jetting transition boundary. The dotted lines indicate the corresponding numerical model solutions using the nonlinear equation of state. The arrows indicate the directions the boundaries shift as a result of the linearization of the equation of state. The horizontal shading indicates the physical tipstreaming region predicted by the approximate boundaries. The diagonal shading indicates the feasible region predicted from the numerically calculated boundaries. The cross hatched pattern indicates overlap between these two regions.

Figure 5.1 (a) Image of steady state tipstreaming using constant volumetric flow rates for both the continuous and dispersed phase fluids. (b) Image of thread formation using the active feedback controller. The set point is located 220 microns downstream of the exit of the dispersed phase channel, the proportional constant is $K_p = 9.52 \times 10^{-7} \text{ V}/\mu\text{m}$, and the derivative constant is $K_d = 0$.

Figure 5.2 (a) Image of the interface captured during controlled tipstreaming. Both the set point and process values are measured from the left edge of the image in pixels. (b) The image shown in (a) post analysis, using built-in MATLAB commands to threshold and morphologically remove features smaller than 7000 connected pixels. (c) Image of the resulting interface after applying the built-in “edge find” command to (b) to determine the location of the tip of the interface.

Figure 5.3 Block diagram of the tipstreaming controller. A set point and control parameter(s) are selected using a LabVIEW user interface, and the interfacial tip position from the previous iteration is recorded. The controller adjusts the voltage

supplied to an electric-to-pneumatic transducer through a PCI data acquisition card. The transducer adjusts the pressure supplied to a pressurized reservoir vessel containing the dispersed phase liquid. The liquid flows into the microfluidic device, forming an interface within the flow focusing junction. The resulting interface is imaged to determine the position of the interface tip. The tip position is reported to the controller, completing an iteration of the control loop.

Figure 5.4 (a) Tip position as a function of time during control of the interface position for a typical experiment. The set point is located 220 microns downstream of the exit of the dispersed phase channel, the proportional constant is $K_p = 9.52 \times 10^{-7}$ V/ μm , and the derivative constant is $K_d = 0$. (b) Sample fast Fourier Transform of the oscillation data presented in (a). The maximum peak is observed at a frequency of 0.0029 Hz corresponding to a period of 345 seconds.

Figure 5.5 Histogram of interfacial tip location measurements obtained during control scheme operation. The set point is located 220 microns downstream from the exit of the dispersed phase channel, the proportional constant is $K_p = 9.52 \times 10^{-7}$ V/ μm , and the derivative constant is $K_d = 0$. The normal distribution corresponds to the mean and standard deviation of the data shown.

Figure 5.6 Standard deviation of the measured tip position as a function of the controller proportionality constant. Experiments using K_p values within the shaded regions result in unstable control of the interface. Unstable control of the interface results in the interface being forced upstream into the inlet channel, or the production of larger primary droplets. The set point for each experiment is located 220 microns downstream from the exit of the dispersed phase channel.

Figure 5.7 Standard deviation of the measured tip position as a function of the controller derivative constant. Experiments using K_d values within the shaded region results in unstable control of the interface. Unstable control of the interface results in the interface being forced upstream into the inlet channel, or the production of larger primary droplets. The set point for each experiment is located 220 microns downstream from the exit of the dispersed phase channel. The proportional constant is $K_p = 9.52 \times 10^{-7}$ V/ μm .

Figure 5.8 Standard deviation of the measured tip position as a function of the set point (SP). Experiments using SP values within the shaded regions result in unstable control of the interface. Unstable control of the interface results in the interface being forced upstream into the inlet channel, or the production of larger

primary droplets. The proportional constant is $K_p = 9.52 \times 10^{-7} \text{ V}/\mu\text{m}$. Derivative control is not used, $K_d = 0$.

Figure 6.1 (a) A schematic representation of the separator design including device dimensions. (b) Image of microfluidic separator geometry with illustrations representing the stream lines of the droplets. Fluid flows is from left to right. Both micron sized and primary droplets enter the geometry on the red streamline on the left. Deflection of the larger droplets onto the blue streamline results in droplet separation as the micron sized droplets remain on the red stream line.

Figure 6.2 Image of successful droplets separation. Larger primary droplets are deflected by the pillar obstacles into the secondary exit channel. The movement of the smaller droplets remain unaffected, traveling into the main exit channel.

Figure 7.1 Image of geometry controlled droplet production in a flow focusing geometry. Droplet diameters are $150 \mu\text{m}$ and channel width is $200 \mu\text{m}$.

Figure 7.2 Diagram of flow focusing geometry, additional microchannels, and merge point downstream of droplet production geometry.

Figure 7.3 Image of droplet traveling through a microchannel after acceleration. Thread formation occurs at the rear of the droplet as continuous phase flows past the drop.

Figure 7.4 Distance downstream of the acceleration point at which thread formation is observed as a function of the total liquid volumetric flow rate. The \blacklozenge represent a surfactant concentration of $0.2 \text{ mol}/\text{m}^3 \text{ C}_{12}\text{E}_8$, \bullet represent a surfactant concentration of $0.05 \text{ mol}/\text{m}^3 \text{ C}_{12}\text{E}_8$, and \blacksquare represent a surfactant concentration of $0.025 \text{ mol}/\text{m}^3 \text{ C}_{12}\text{E}_8$.

Figure 7.5 Values for measured droplet velocity and predicted maximum fluid velocity as a function of distance from the acceleration point for $Q_a = 150 \mu\text{l}/\text{min}$. The \bullet represent the measured droplet velocities and the solid line is the predicted maximum fluid velocity given by Eq. (7.5). The channel image illustrates the approximate location within the exit channel.

Figure 7.6 Estimated values of the capillary number at which tipstreaming occurs as a function of the total liquid volumetric flow rate. The \blacklozenge represent a surfactant concentration of $0.2 \text{ mol}/\text{m}^3 \text{ C}_{12}\text{E}_8$, \bullet represent a surfactant concentration of $0.05 \text{ mol}/\text{m}^3 \text{ C}_{12}\text{E}_8$, and \blacksquare represent a surfactant concentration of $0.025 \text{ mol}/\text{m}^3 \text{ C}_{12}\text{E}_8$.

Figure 7.7 Experimental operating diagram for tipstreaming from the rear of a droplet. The ● symbols represent conditions where tipstreaming from the rear of a droplet is observed, × represent conditions where no thread is observed at the exit channel of the device, and □ represent conditions where non-tipstreaming droplet breakup occurs immediately upon entering the acceleration point.

Figure 7.8 Experimental operating conditions reproduced from Figure 7.7 with three additional boundaries. The --- line is a boundary below which interfacial surfactant concentrations are too low to expect thread formation. The solid line is a line of constant capillary number of $Ca = 0.15$, below which thread formation is not observed. Lastly, the -- line is another line of constant capillary number, $Ca = 0.35$, above which droplet breakup within the acceleration point is observed.

Figure 8.1. Four images of tipstreaming thread formation and droplets resulting from breakup. Flow rate values for all four cases are $Q_c = 80 \mu\text{l}/\text{min}$ and $Q_d = 2 \mu\text{l}/\text{min}$. The surfactant concentration of $C_{12}E_8$ given in micromolar values is reported for each of the four cases.

Figure 8.2. On chip optically measured thread and droplet diameters as a function of flow rate ratio. The continuous phase flow rate is kept fixed at $Q_c = 80 \mu\text{l}/\text{min}$ and surfactant concentration is $300 \mu\text{mol}/\text{l}$. Model predicted thread sizes are determined at the location of the open symbols for different flow rate ratio values. The line is added to indicate the estimated model result between calculated points.

Figure 8.3. On chip optically measured droplet diameter as a function of surfactant concentration. The continuous and dispersed phase flow rates are kept fixed at $Q_c = 80 \mu\text{l}/\text{min}$ and $Q_d = 2 \mu\text{l}/\text{min}$. Model predicted thread sizes are determined at the location of the open symbols for different surfactant concentrations. The line is added to indicate the estimated model result between calculated points.

Figure 8.4. On chip optically measured droplet diameter as a function of flow rate magnitude. The flow rate ratio is kept constant such that $Q_d = Q_c / 40 \mu\text{l}/\text{min}$ and surfactant concentration is $300 \mu\text{mol}/\text{l}$. Model predicted thread sizes are determined at the location of the open symbols for different flow rate magnitudes at constant φ . The line is added to indicate the estimated model result between calculated points.

Figure 8.5. Tipstreaming operating diagram for both pure $C_{12}E_8$ system and for PEG-DA/ $C_{12}E_8$ system. The pure $C_{12}E_8$ operating diagram is reproduced from

data in Moyle *et al.* Physics of Fluids 2012. The shaded region represents conditions where tipstreaming is observed. Experiments using the PEG-DA/C₁₂E₈ are plotted over the original operating diagram. Filled symbols represent conditions where tipstreamed is observed and open symbols represent some other mode of droplet breakup occurring.

Figure 8.6. DLS measured post processed particle diameter as a function of flow rate ratio. The continuous phase flow rate is kept fixed at $Q_c = 80 \mu\text{l}/\text{min}$ and surfactant concentration is $80 \mu\text{mol}/\text{l}$. The error bars indicate one standard deviation in the particle size distributions measured using dynamic light scattering.

Figure 8.7 Dynamic light scattering intensity based size distributions determined using the mobile interface variant of the Stokes-Einstein relationship for flow rate ratios values of 1/40, 1/50, 1/60, and 1/80.

Figure 8.8. DLS and off chip optically measured post processed particle diameters as a function of surfactant concentration. The continuous and dispersed phase flow rates are kept fixed at $Q_c = 80 \mu\text{l}/\text{min}$ and $Q_d = 2 \mu\text{l}/\text{min}$. Filled in symbols represent measurements made using DLS and open symbols represent off chip optical measurements using a 90x magnification oil immersion objective.

CHAPTER 1**INTRODUCTION**

Microscale tipstreaming is a unique method to overcome the limiting length scale in microfluidics allowing for production of submicron-sized droplets. Tipstreaming is the creation of a thin thread from a highly curved fluid interface. The formation of the thread arises from a balance of viscous and surfactant effects acting on the fluid-fluid interface. Controlling and understanding the tipstreaming process is essential for its successful application in areas such as synthesis of nanoscale particles, manipulation of biomolecules, occlusion therapy, enzyme activity studies, and others.

The work presented in this thesis examines and resolves several technical challenges which have limited the use of tipstreaming as a robust tool to generate micron and sub-micron sized droplets. The three primary challenges examined are determining tipstreaming conditions for an arbitrary oil-water-surfactant system, eliminating the larger primary droplets, and size measurements of the micron sized droplets. Overcoming these technical challenges makes tipstreaming a more attractive technique to generate micron and sub-micron particles and droplets. The versatility of the materials, geometries, flow fields, and thread sizes available to tipstreaming suggests tipstreaming will potentially have a broad impact.

The first technical challenge examined is determining tipstreaming conditions for an arbitrary oil-water-surfactant system. Chapter 4 develops a semi-analytical model capable of predicting operating conditions for microscale tipstreaming. This limits the need for experimentally mapping operating diagrams

for different systems or geometries. The model relies on interfacial shape observations indicative of microscale tipstreaming to simplify the fluid flow and surfactant transport equations. The result is an interfacial mass balance of surfactant. Conditions where the mass balance can be satisfied define the operating conditions for microscale tipstreaming. Results from the model are compared with our own experimental results. Good agreement is found between model predictions and experiments. Scaling of each boundary that controls the feasible tipstreaming region is given. Finally, the model is able to guide selection of device geometry and surfactant properties to shift or expand the feasible region where microscale tipstreaming is expected.

The second technical challenge, removing the larger primary droplets, is the focus of both Chapter 5 and 6. Chapter 5 discusses the development of an active feedback control loop. This controller is capable of eliminating the production of primary droplets and producing a continuous thread, and therefore a continuous droplet stream. A proportional controller is designed to successfully control the position of the interface and generate a continuous thread. Analysis of the tip position as a function of time is performed to determine controller stability. Experimental controller optimization is used to find the optimal proportional gain constant and set point value to minimize fluctuations in the produced droplet sizes. An additional derivative component is incorporated in an attempt to increase controller stability, but this component is found to be ineffective. The generation of a continuous thread reduces the loss of potentially expensive feedstock chemicals as well as eliminates the need for size separation.

In Chapter 6, an alternative technique is developed to remove the larger primary droplets. This work discusses the development of an inline microfluidic separator capable of removing the larger primary droplets from the micron sized droplet stream. Multiple microfluidic devices producing droplets in parallel is a commonly suggested method to increase production rates. However, the controller discussed in Chapter 5 requires a significant amount of equipment for a single devices. Thus, an inline separator reduces the costs associated with parallelizing droplet production while eliminating the need for additional off chip size separation. The chip design offers a wide range of operating conditions over which separation can be achieved. The efficiency of the separator is examined for several conditions and found to capture between 80% and 95% of the smaller droplets produced while removing 100% of the primary droplets. The high degree of separation is maintained for several hours of droplet production.

The work in Chapter 7 investigates tipstreaming in a different geometry not previously reported. Tipstreaming is observed to occur at the rear of a large droplet traveling within a microchannel. This is observed in cases where the drop velocity is higher than the average fluid velocity in the microchannel. Large droplets are generated in a flow focusing geometry and accelerated within the exit channel by adding additional continuous phase liquid. As a result, fluid sweeps past the droplet driving the generation of Marangoni stresses similar to flow focusing based tipstreaming. A unique feature of tipstreaming from the rear of a droplets is thread formation occurs at different distances downstream of the acceleration point. Further examination shows deformations in the microchannel height result in

changes in droplet velocity within the exit channel. These results give insight into the effect of confinement on droplet breakup and thread formation. Additionally, basic criteria for observing tipstreaming from the rear of a drop are developed and used to generate an experimental operating diagram. These results provide further insight into tipstreaming mechanics and the effects of channel geometry.

Chapter 8 examines the effect tipstreaming conditions have on the size of the droplets resulting from thread breakup. The ability to alter the size of the small droplets produced would greatly increase the number of applications that would benefit from using tipstreaming. We have investigated droplet size as a function of the liquid flow rate ratio, surfactant concentration, and flow rate magnitudes. The result is a guide detailing a method to generate droplets of a desired size using different tipstreaming operating conditions. The ability to control droplet size using multiple parameters is advantageous due to the possibility of application specific constraints.

On chip optical measurements are used to provide insight into effect of varying operating conditions for larger threads. Significant size differences are observed for differing surfactant concentrations and flow rate ratios. The changes in size allow for designed control over the size of the drops generated by selecting tipstreaming operating conditions. Smaller droplet sizes are used to investigate the formation of hydrogel particles generated from the droplets produced via tipstreaming. Generating particles allows for off chip collection and size measurements using dynamic light scattering. Particle size follows similar trends to those measured optically and is also characterized as a function of operating

conditions. The combined results demonstrate a technique to control the size of droplets and particles being produced via tipstreaming.

Chapter 9 summarizes the conclusions and technical achievements of this work. These advances demonstrate tipstreaming as a useful technique to generate droplets and particles ranging in size from hundreds of nanometers to several microns. Many of the technical challenges preventing the use of tipstreaming have been addressed and resolved within this work. Together these developments and techniques facilitate the use of tipstreaming as a tool to generate monodisperse nanoscale materials.

CHAPTER 2**BACKGROUND****2.1 APPLICATION AND PRODUCTION OF MICRON SIZED DROPLETS**

Monodisperse micron and sub-micron sized droplets have the potential to be useful in a broad range of applications. These applications take advantage of the small droplet size and high surface to volume ratio. Micron sized drops are used to perform processes either hindered or unfeasible in larger droplets. A droplet with a diameter of a micron has a volume of a several hundred attoliters or $O(10^{-16})$ liters. These length scales begin to approach concentrations where a statistically finite number of individual molecules can be contained per drop. As an example, generating concentrations of an analyte on the order of a micromolar is easily attainable in a standard laboratory environment. Creating micron sized droplets from such a solution results in only a few hundred molecules of the analyte per drop.

Several applications have taken advantage of this concept to gain precise control over a system of interest. In particular, manipulation and containment of proteins and other biomolecules typically requires a high degree of control. Burnett *et al.* outlined a procedure to use micron sized droplet to contain and examine the structure of surfactant-protein aggregates[1]. Similarly, this approach has aided in the analysis of single enzyme molecule kinetics to determine individual molecular activity[2]. These applications exploited drop size to contain a system and allowed for enhanced analysis of the structure or activity. The size also allowed for greater control of reactions occurring within the drops. Recently, interest in using droplets

as reaction vessels has increased for expensive chemicals or cases with limited amounts of reagent[3]. Micron sized drops allow for enhanced system control in reactions such as nanoparticle synthesis[4-8] and in chemical separations[9].

In addition to greater control over the drop contents, transport characteristics of micron sized droplets has proven advantageous in several applications. Diffusive transport becomes geometry dependent if the length scale of a structure is on the order of the thickness of the diffusion layer. This occurs for highly curved interfaces under relevant analyte concentrations. Recently, experimental and scaling analysis of surfactant diffusion to highly curved interfaces have demonstrated and modeled this relationship[10, 11]. These results demonstrated the dependence dynamic processes can have on system geometry. The effect is important in analyzing the efficacy of micron sized drops in delivery of chemotherapy drugs[12] and increased transdermal uptake of pharmaceuticals into the blood stream[13].

Lastly, micron sized droplets have length scales relevant to physiological structures making them useful in treating diseases. As an example, micron droplets have recently been generated for use in occlusion therapy treatment of cancerous tumors[14, 15]. Occlusion therapy utilizes stable phase changing droplets made of perfluoropentane, a material with a boiling point of 29°C[14]. The droplets were generated via tipstreaming at room temperature and coated with a lipid and surfactant shell. Upon injection into the blood stream, the shell prevents premature droplet vaporization. An ultrasound is used to rupture the shell and induce a gas embolism in a specific area of the patient. For successful treatment, droplets must

be on the order of a micron in size so the resulting bubble adequately blocks blood flow to the targeted tumor.

Presented here are a few practical instances which require or benefit from the use of micron and sub-micron sized droplets. The diversity in techniques requires many different materials and drop sizes to fulfill all of the application specific requirements. However, standard production techniques are generally limited in monodispersity, drop material, or production costs. These and other applications would greatly benefit from a robust production technique able to generate a range of drop sizes using many different materials.

Numerous methods of generating micron sized drops have been examined, taking advantage of different principles, techniques, and material properties. Typically, production techniques are categorized as either active or passive emulsification. Active emulsification requires high energy input into a two phase system to generate interfacial area. This category includes ultrasonication[16-18], high shear processes[19, 20], or membrane emulsification[21-23]. The issue with these techniques is the lack of control over the droplet size. Jafari *et al.* examined several high energy emulsification processes and found polydispersity to be difficult to control due to over processing and re-coalescence[18, 20].

Passive emulsification techniques use various equipment geometries or chemical properties to form nanoscale structures. These methods typically have better control over droplet size and polydispersity but are either prohibitively expensive or system specific. Several classes of techniques are included in this category such as, phase inversion[24-27], self-assembly[28-30], sub-micron scale

emulsification devices[31-36], and instability based breakup[15, 37-61]. Phase inversion and self-assembly utilize the chemical structure of the material to form nanostructured material. These techniques have the ability to create highly monodisperse particles, droplet, and micelles[24, 25]. However, their use is limited in applications due to specific required chemistry of the components.

Devices with sub-micron sized features generate droplets based on geometry controlled breakup. These devices are typically fabricated from pulled capillaries or chemically etched channels, several hundred nanometers in depth. Capillary based devices are difficult and time consuming to generate since they require precise capillary pulling[37-42]. Additionally, clogging of the capillary tip with debris can render the device unusable. Chemically etching channels is a more robust technique for creating reproducible nanometer length scales[31, 32]. However, these devices are expensive to produce and have similar issues with channel clogging. As a result, used of these devices to generate micron sized drops has been limited.

Lastly, there are many techniques which utilize instabilities to generate micron sized droplet. Hydrodynamic instabilities including satellite droplet generation[62] and viscoelastic necking[52-54] are able to produce micron sized droplets. These drops form due to a capillary instability within the thin fluid bridge during breakup of larger droplets. Production rates for these droplets are very low compared to other passive techniques. Electro-hydrodynamic instabilities have been used to generate micron sized droplets[55, 61]. The most successful implementation of these techniques is electro-spraying which is used commercially

in electrospinning fibers and nanostructured coatings. [56-60, 63]. However, practical challenges arise including sustained droplet formation and drop collection during emulsification.

Due to the issues with implementing these techniques, we examine using microscale tipstreaming as a tool to generate micron sized droplets. This technique utilizes a hydrodynamic instability to generate droplets much smaller than the characteristic length scales of system. As a result, tipstreaming can generate micron sized droplets within microfluidic geometries which have reduced clogging and lower production costs. Additionally, the device design is conducive to drop collection, post process stabilization, and parallelizing. These features and others suggest tipstreaming as a viable source of micron sized droplets.

2.2 TIPSTREAMING AND MICROSCALE TIPSTREAMING

Microscale tipstreaming resembles tipstreaming from isolated droplets in unbounded media experiencing shear or elongational flows. Taylor was the first to observe tipstreaming during his analysis of a single droplet deformed in shear and uniaxial elongational flow fields[49]. In this early study, Taylor attributed the formation of highly curved points at the drop poles to impurities within the system. Similar elongational flow field experiments were performed by Grace which established tipstreaming occurs at a low viscosity ratio between the two fluids[64]. As with the experiments performed by Taylor, surfactant was not intentionally added to the system. However, interfacial tension dynamics were reported indicating impurities again played a role in generating the observed tipstreaming.

Stone *et al.* performed elongational flow experiments over a similar range of viscosity ratios as Grace[65]. However, the system examined by Stone *et al.* did not exhibit dynamic interfacial tension and tipstreaming was not observed[66].

De Bruijn first established the importance of surfactant and the experimental conditions necessary for tipstreaming in isolated droplets [48]. Tipstreaming criteria included interfacial surfactant coverages between 10% and 90% of the maximum interfacial concentration along with a small viscosity ratio for the two liquids, $\lambda \equiv \mu_i / \mu_o \leq 0.1$. The subscript *i* and *o* refer to the inner, dispersed phase and outer, continuous phase liquids, respectively. On the basis of experimental observations, de Bruijn proposed the currently accepted mechanism for tipstreaming. As a flow field is applied, viscous forces act to deform the interface while interfacial tension resists deformation. The external flow field sweeps surfactant adsorbed to the interface toward the two droplet poles causing local accumulation. The increase in interfacial surfactant concentration near the poles locally decreases the interfacial tension. To maintain the stress balance at the interface, the local curvature at the droplet poles must increase in response to the interfacial tension decrease. At high curvatures, viscous forces pull a thread from the tip, which breaks up into droplets due to a capillary instability [40, 67-70]. The parent droplets considered by de Bruijn were on the order of 0.5 mm in diameter and produced thread droplets 10 to 20 microns in diameter. Janssen *et al.* reported similar tipstreaming requirements as de Bruijn for different surfactant and droplet systems[71, 72].

Microscale tipstreaming closely resembles the phenomenon analyzed by de Bruijn. Microscale tipstreaming utilizes a microfluidic flow focusing geometry to generate the flow profile necessary for tipstreaming. In this geometry, the dispersed phase and continuous phase liquids flow into three separate microchannels. These three channels merge and the immiscible liquids are forced to flow through a contraction. The contraction results in an elongational flow that promotes pinch-off of dispersed phase droplets. Several different modes of droplet production have been observed in this type of geometry[43, 44, 73]. Figure 2.1, reproduced from Anna and Mayer, shows the four different classifications of droplet breakup observed in a flow focusing geometry. Initial characterization of some of these droplet modes was performed by Anna *et al.*[73]. Within this work, the effect of flow rate magnitude and flow rate ratio was shown to have a large impact on droplet production characteristics.

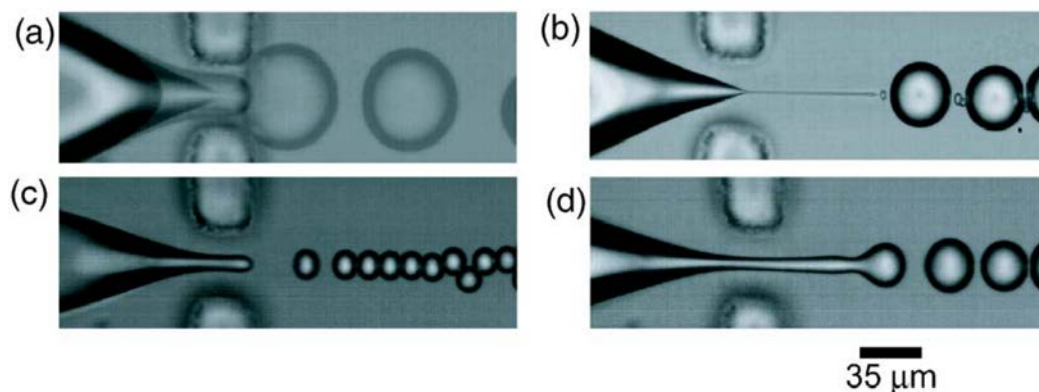


Figure 2.1 A series of images representing the four modes of droplet breakup observed within a flow focusing geometry including (a) geometry controlled, (b) microscale tipstreaming, (c) dripping, and (d) jetting. Reprinted with permission from [43], Copyright 2006, AIP Publishing LLC.

The mode of breakup depicted in Figure 2.1 b closely resembles tipstreaming observed in isolated drops. Microscale tipstreaming produces a

continuous stream of micron sized droplets periodically interrupted by the formation of larger primary droplets. Because of the similar features, Anna and Mayer referred to the breakup mode as microscale tipstreaming[43]. Based on microscale tipstreaming experiments, they concluded the mechanisms for microscale and isolated droplet tipstreaming are identical. First, their work demonstrates that the presence of surfactant is necessary to observe microscale tipstreaming. Within a specific range of surfactant concentrations, tipstreaming is observed at flow rates between the squeezing and dripping breakup modes. In addition, the viscosity ratio is required to be $\lambda \leq 0.1$ for microscale tipstreaming, and the capillary number range is approximately $0.2 < Ca < 0.6$, consistent with de Bruijn's results[43]. Therefore, it is concluded that the phenomena observed in microfluidic geometries is the same as that observed in isolated drops.

In conjunction with experimental work, Anna and Mayer also developed a preliminary model for microscale tipstreaming of which the basis is similar to the tipstreaming model we present in Chapter 4. The model developed by Anna and Mayer utilizes geometric arguments about the cone shape to determine the expected flow profile. An approximation of the flow profile was used to capture the features of the elongational flow profile. The flow profile was then used to estimate the viscous stresses acting on the interface. An expected interfacial tension profile was determined which is needed to balance the viscous stresses on the interface. This model, however, does not include mass transport effects for soluble surfactants and was unable to predict tipstreaming conditions. The model developed by Anna and

Mayer was significant since the basis is similar to the tipstreaming model developed within this work.

In addition to surfactant concentration and flow rate ratio effects studied by Anna and Mayer, other experimental parameters have been examined including viscosity ratio, geometry, and surfactant type[44, 45, 47, 52, 74]. Lee *et al.* expanded upon the initial work investigating microscale tipstreaming. This included investigating the role of device geometry and viscosity of the continuous phase. The authors also developed relationships for thread length as a function of time and characteristic time scales for droplet formation. Additionally, they outlined the construction of basic operating diagrams for tipstreaming and determined scaling relationships for thread length. In subsequent work from the same authors, the effect of a viscoelastic disperse phase was examined[75]. These experiments also exhibit the production of long threads as a result of a tipstreaming like mechanism.

Microscale tipstreaming has also been observed in a number of systems and geometries other than the flow focusing geometry. Ward *et al.* demonstrated tipstreaming was able to occur as the result of interfacial reactions which generate surfactant. Oleic acid added to the continuous phase mineral oil reacted with sodium hydroxide in the dispersed phase to form surfactant at the interface. Under specific reactant concentrations and flow rate conditions, tipstreaming was observed. This suggests the dynamics of interfacial reactions can have an important role in droplet breakup. Lastly, Jeong *et al.* have experimentally investigated tipstreaming in order to produce polymer nanoparticles. A specific surfactant

system and a more complicated microfluidic device were used to produce droplets of water and low molecular weight poly(ethylene glycol) diacrylate. UV induced crosslinking of the polymer resulted in the formation of stable nanoparticles. While only two tipstreaming production conditions were tested, a drop size dependence on these conditions was observed. Several other thread generation techniques have also been studied that use different mechanisms, some of which do not involve surfactant [38, 42, 52, 55, 76] while others do not use microscale geometries [46, 77].

2.3 MODELING INTERFACIAL DEFORMATION

In addition to experiments, tipstreaming has been investigated analytically and numerically for both insoluble and soluble surfactants[50, 51, 77-83]. Modeling tipstreaming is a complex challenge due to the large difference in length scales, interfacial deformations, and surfactant dynamics. The first theoretical investigation incorporating interfacial tension dynamics in drop deformation was investigated by Flumerfelt for small deformations in shear and elongational flow fields[84]. Stone and Leal later expanded the range of deformations studied using boundary integral simulations and convective surfactant transport on the drop interface[85]. The results of this analysis indicated a critical capillary number needed to obtain un-steady droplet deformation. Droplet deformation mechanisms were identified including surfactant convection, surfactant diffusion, and Marangoni stresses. However, this analysis was limited in its ability to resolve droplet breakup and did not incorporate soluble surfactant.

Milliken *et al.* expanded on Stone and Leal's initial analysis, studying different droplet viscosities, time dependent drop motion, and surfactant solubility[78, 79]. Several simulations within this work generated interfacial shapes with sharp points which the authors suggested indicate the onset of tipstreaming. Eggleton *et al.* numerically examined the thread formation process more rigorously using boundary integral methods. Their results found required surface coverages and viscosity ratios consistent with de Bruijn's criteria[80-82]. They also found sharp gradients in interfacial tension were required to observe thread formation. Lastly, the results estimated the ratio of daughter to parent droplet size which is similar to those observed experimentally. These results confirmed the tipstreaming mechanism proposed by de Bruijn and demonstrate the importance of surfactant dynamics in tipstreaming analysis.

With the advancement in simulation techniques, the development of hybrid simulations attempted to more accurately describe the surfactant and interface dynamics. Bazhlekov *et al.* reported a dual simulation scheme used for analysis of tipstreaming like droplet deformation in pure shear flow[50]. Their work combined both boundary integral and finite volume simulation to determine droplet shape and fluid flow profiles. This techniques enabled them to report breakup mode transition values for capillary numbers as a function of operating parameters. Booty and Siegel also used a combined analytic and numerical approach to investigate conditions for tipstreaming[83]. In this work, they used slender body theory to determine the droplet shape, however numerical techniques were implemented in the droplet pole region with high interfacial curvature. Thread formation

requirements and interfacial tension gradients reported in their results were similar to previous studies. The majority of studies reported thus far have been restricted to insoluble surfactants. However, the role soluble surfactants have in relaxing Marangoni stresses is critical to the analysis of tipstreaming.

Booty and Siegel have since developed a hybrid numerical method to include the effects of soluble surfactant[86]. This model utilized boundary integral simulations to solve the free boundary problem while incorporating a singular perturbation analysis to analyze surfactant dynamics in highly concentrated regions. This technique has recently been used to generate the first computationally resolved instance of tipstreaming with soluble surfactants[87]. The results of those simulations have been compared to work presented in this thesis. Good agreement is seen between our experimental results and semi-analytic model of tipstreaming and the numerical results they presented despite the differences in the examined systems.

Several studies have also focused on analysis of the thread size generated via tipstreaming. An analytical model has been developed that studies the conical structure observed during chemical-reaction driven tipstreaming at the end of a capillary [51, 77]. This analysis developed self-similar solutions for the conical interface shape and asymptotically matches them to solutions for a thread that is necessary to alleviate the singularity at the cone apex. These results yielded estimates of the thread sizes, but could not predict the range of operating parameters that would result in tipstreaming. Experiments and boundary element simulations have also been used to predict thread size in a similar phenomenon for droplet

breakup in concentric capillary tubes [42]. The mechanism governing droplet breakup in those experiments and simulations did not use surfactants and is thus different from the one described in this work.

These numerical and analytical model results support the tipstreaming mechanism and demonstrate the ability to solve the complex problem of a deforming interface coupled with surfactant adsorption. However, there are at least three significant reasons why microscale tipstreaming is difficult to model using numerical methods. In contrast to most existing numerical studies that examine perturbations of interfacial concentration about equilibrium, tipstreaming in microfluidics involves rapid generation of new interface such that surface coverages are low and perturbations should be considered to be about a nearly clean interface. The continuous and periodic nature of microscale tipstreaming requires the determination of the transient interfacial shape and accurate determination of droplet breakup conditions. Finally, the external elongational flow field is more complicated in rectangular microfluidic devices.

2.4 ACTIVE CONTROL OF FLUID FLOW IN MICROFLUIDICS

The use of active control techniques in microfluidics continues to increase as microfluidic devices develop towards true laboratory on a chip capabilities. Currently, there are many applications which have benefited from successful implementation of control systems. These techniques implement feedback control systems to actively regulate process variables. Systems of interest include manipulation of flow fields[88-91], temperature[92, 93], pH[94, 95], and electrical

fields[96-98]. In the context of the work presented within this thesis, it is most relevant to discuss the manipulation of flow fields within microfluidics.

In general, control systems measure a process value for which a desired set point is determined. A control variable is altered to adjust the process value closer to the desired set point. In common control algorithms, the change made to the control variable depends on the magnitude of the difference between the process value and set point. Flow field manipulations generally attempt to control the position of particles, drops, or interfaces within microfluidics. These systems use position as the process value to be controlled. The position relative to a set point is determined via image processing to obtain process values relative to a set point. A control variable is then used to adjust the flow field and alter the position of the particle, drop, or interface. Two common control variables include the liquid flow rates into the device and the flow resistance of different exit channels. Successive iteration of a control loop drives the process value to the set point resulting in flow field control within microfluidics.

One of the first examples of this type of control was demonstrated by Kuczynski *et al.* to control the position of a laminar flow interface[91]. In their work, the lateral position of the interface was controlled via a proportional-integral-derivative controller. Upon changing the desired set point, the controller altered the flow rates of each phase to adjust the interface position to the new desired location. The system exhibited a rapid response time of less than 0.1 seconds and was capable of maintaining the interface position.

Another significant advancement in controlling fluid flow fields was the development of a hydrodynamic trap within microfluidics by Tanyeri *et al.*[89]. This work attempted to maintain the position of a particle within the stagnation point of an elongational flow field. Image analysis of the particle center of mass was used to adjust the flow stagnation point position and steer the particle to the trap center. A unique feature of the system was the rapid response time required for trapping and releasing particles. To quickly adjust the position of the stagnation point, flow resistance in one exit channel was used as the control variable. A multilayer microfluidic device was fabricated to incorporate the adjustable resistance feature. The resistance to flow in one of the two extensional axes channels was altered using a membrane valve. The membrane valve located over the exit channel allowed for pressure supplied to the valve to act as the control variable. Increasing the pressure within the valve decreased the cross sectional area of the exit channel increasing the resistance to flow. This control technique resulted in a much faster response of the system than flow rate alterations. The result was effective control and trapping of particles within a microfluidic device.

Lastly, controllers have been implemented to actively manipulate droplet positions within microfluidics. Maddala *et al.* developed a technique to sort and synchronize droplets containing different amounts of dye[90]. Coalescence of the two droplet streams was then used as a proof of concept in initiating chemical reactions. This was accomplished through imaging analysis and control over flow resistance in the exit channels. A unique feature of this work was the use of model predictive control to aid in the synchronization of two droplet streams. Control

over droplet movement was achieved for short time periods. Flow field manipulation is an important capability and is relevant to many processes in microfluidics. Increased uses of active controllers within microfluidics will continue as more complicated processes are attempted in microfluidic devices. The ideas and techniques developed within these studies serve as the basis for the controller design reported in Chapter 5 of this work.

1. Burnett, G.R., et al., *Fluorescence correlation spectroscopy of water-in-oil microemulsions: an application in specific characterisation of droplets containing biomolecules*. Colloids and Surfaces A-Physicochemical and Engineering Aspects, 2004. **250**(1-3): p. 171-178.
2. Stamatis, H., et al., *Kinetic-study of lipase-catalyzed esterification reactions in water-in-oil microemulsions*. Biotechnology and Bioengineering, 1993. **42**(8): p. 931-937.
3. Song, H., D.L. Chen, and R.F. Ismagilov, *Reactions in droplets in microfluidic channels*. Angewandte Chemie-International Edition, 2006. **45**(44): p. 7336-7356.
4. Sager, W.F.C., *Controlled formation of nanoparticles from microemulsions*. Current Opinion in Colloid & Interface Science, 1998. **3**(3): p. 276-283.
5. Rahy, A., et al., *Nano-emulsion use for the synthesis of polyaniline nano-grains or nano-fibers*. Polymers for Advanced Technologies, 2011. **22**(5): p. 664-668.
6. Porras, M., et al., *Ceramic particles obtained using W/O nano-emulsions as reaction media*. Colloids and Surfaces a-Physicochemical and Engineering Aspects, 2005. **270**: p. 189-194.
7. Ye, C.X., et al., *Preparation and Characterization of Organic Nano-Titanium Dioxide/Acrylate Composite Emulsions by in-situ Emulsion Polymerization*. Journal of Macromolecular Science Part a-Pure and Applied Chemistry, 2011. **48**(4): p. 309-314.
8. Baek, J.H., et al., *Preparation of monodispersed and nano-sized spherical SiO₂ particles by emulsion method*, in *Designing, Processing and Properties of Advanced Engineering Materials, Pts 1 and 2*, S.G. Kang and T. Kobayashi, Editors. 2004, Trans Tech Publications Ltd: Zurich-Uetikon. p. 1161-1164.
9. Okubo, Y., et al., *Liquid-liquid extraction for efficient synthesis and separation by utilizing micro spaces*. Chemical Engineering Science, 2008. **63**(16): p. 4070-4077.
10. Alvarez, N.J., Walker, L. M., and Anna, S. L., *A Microtensiometer To Probe the Effect of Radius of Curvature on Surfactant Transport to a Spherical Interface*. Langmuir, 2010. **26**(16): p. 13310-13319.
11. Alvarez, N.J., L.M. Walker, and S.L. Anna, *Diffusion-limited adsorption to a spherical geometry: The impact of curvature and competitive time scales*. Physical Review E, 2010. **82**(1).

12. Constantinides, P.P., et al., *Formulation development and antitumor activity of a filter-sterilizable emulsion of paclitaxel*. *Pharmaceutical Research*, 2000. **17**(2): p. 175-182.
13. Kotyla, T., et al., *Increased bioavailability of a transdermal application of a nano-sized emulsion preparation*. *International Journal of Pharmaceutics*, 2008. **347**(1-2): p. 144-148.
14. Bardin, D., et al., *High-speed, clinical-scale microfluidic generation of stable phase-change droplets for gas embolotherapy*. *Lab on a Chip*, 2011. **11**(23): p. 3990-3998.
15. Martz, T.D., et al., *Microfluidic Generation of Acoustically Active Nanodroplets*. *Small*, 2012. **8**(12): p. 1876-1879.
16. Kanda, T., et al., *Design and Evaluation of Emulsion Generation Device Using Ultrasonic Vibration and Microchannel*. *Japanese Journal of Applied Physics*, 2011. **50**(7).
17. Jafari, S.M., Y.H. He, and B. Bhandari, *Production of sub-micron emulsions by ultrasound and microfluidization techniques*. *Journal of Food Engineering*, 2007. **82**(4): p. 478-488.
18. Jafari, S.M., Y.H. He, and B. Bhandari, *Nano-emulsion production by sonication and microfluidization - A comparison*. *International Journal of Food Properties*, 2006. **9**(3): p. 475-485.
19. Hong, J.S. and C. Kim, *Generation of sub-micron-sized droplets, by continuous extensional flow*. *Journal of Non-Newtonian Fluid Mechanics*, 2010. **165**(11-12): p. 681-686.
20. Jafari, S.M., Y. He, and B. Bhandari, *Optimization of nano-emulsions production by microfluidization*. *European Food Research and Technology*, 2007. **225**(5-6): p. 733-741.
21. Ebrahimi, M., et al., *Development and production of oil-in-water vehicles - sub-micron emulsion using tubular ceramic membranes*. *Desalination*, 2008. **224**(1-3): p. 40-45.
22. Liu, W., X.L. Yang, and W.S.W. Ho, *Preparation of Uniform-Sized Multiple Emulsions and Micro/Nano Particulates for Drug Delivery by Membrane Emulsification*. *Journal of Pharmaceutical Sciences*, 2011. **100**(1): p. 75-93.
23. Oh, D.H., et al., *Effect of process parameters on nanoemulsion droplet size and distribution in SPG membrane emulsification*. *International Journal of Pharmaceutics*, 2011. **404**(1-2): p. 191-197.

24. Anton, N. and T.F. Vandamme, *Nano-emulsions and Micro-emulsions: Clarifications of the Critical Differences*. Pharmaceutical Research, 2011. **28**(5): p. 978-985.
25. Bremond, N., H. Domejean, and J. Bibette, *Propagation of drop coalescence in a two-dimensional emulsion: a route towards phase inversion*. Physical Review Letters, 2011. **106**(21): p. 214502.
26. Porras, M., et al., *Studies of formation of W/O nano-emulsions*. Colloids and Surfaces a-Physicochemical and Engineering Aspects, 2004. **249**(1-3): p. 115-118.
27. Solans, C., et al., *Nano-emulsions*. Current Opinion in Colloid & Interface Science, 2005. **10**(3-4): p. 102-110.
28. Hermans, T.M., et al., *Self-assembly of soft nanoparticles with tunable patchiness*. Nat Nano, 2009. **4**(11): p. 721-726.
29. Choi, A.-J., et al., *Characterization of Capsaicin-Loaded Nanoemulsions Stabilized with Alginate and Chitosan by Self-assembly*. Food and Bioprocess Technology, 2011. **4**(6): p. 1119-1126.
30. Meszaros, M., A. Eisenberg, and R.B. Lennox, *Block copolymer self-assembly in two dimensions: nanoscale emulsions and foams*. Faraday Discussions, 1994. **98**(0): p. 283-294.
31. Shui, L.L., A. van den Berg, and J.C.T. Eijkel, *Scalable attoliter monodisperse droplet formation using multiphase nano-microfluidics*. Microfluidics and Nanofluidics, 2011. **11**(1): p. 87-92.
32. Kobayashi, I., et al., *Preparation of monodisperse water-in-oil-in-water emulsions using microfluidization and straight-through microchannel emulsification*. Journal of the American Oil Chemists Society, 2005. **82**(1): p. 65-71.
33. Knoblauch, M., et al., *A galinstan expansion femtosyringe for microinjection of eukaryotic organelles and prokaryotes*. Nature Biotechnology, 1999. **17**(9): p. 906-909.
34. Laforge, F.O., et al., *Electrochemical attosyringe*. Proceedings of the National Academy of Sciences of the United States of America, 2007. **104**(29): p. 11895-11900.
35. Byun, C.K., et al., *Electroosmosis-based nanopipettor*. Analytical Chemistry, 2007. **79**(10): p. 3862-3866.

36. Rodolfa, K.T., et al., *Nanoscale pipetting for controlled chemistry in small arrayed water droplets using a double-barrel pipet*. Nano Letters, 2006. **6**(2): p. 252-257.
37. Ganan-Calvo, A.M., et al., *Straightforward production of encoded microbeads by Flow Focusing: Potential applications for biomolecule detection*. International Journal of Pharmaceutics, 2006. **324**(1): p. 19-26.
38. Ganan-Calvo, A.M. and J.M. Montanero, *Revision of capillary cone-jet physics: Electrospray and flow focusing*. Physical Review E, 2009. **79**(6): p. 066305.
39. Ganan-Calvo, A.M. and P. Riesco-Chueca, *Jetting-dripping transition of a liquid jet in a lower viscosity co-flowing immiscible liquid: the minimum flow rate in flow focusing*. Journal of Fluid Mechanics, 2006. **553**: p. 75-84.
40. Herrada, M.A., A.M. Ganan-Calvo, and P. Guillot, *Spatiotemporal instability of a confined capillary jet*. Physical Review E, 2008. **78**(4): p. 046312.
41. Lopez-Herrera, J.M., A.M. Ganan-Calvo, and M. Perez-Saborid, *One-dimensional simulation of the breakup of capillary jets of conducting liquids. Application to EHD spraying*. Journal of Aerosol Science, 1999. **30**(7): p. 895-912.
42. Castro-Hernandez, E., F. Campo-Cortes, and J.M. Gordillo, *Slender-body theory for the generation of micrometre-sized emulsions through tip streaming*. Journal of Fluid Mechanics, 2012. **698**: p. 423-445.
43. Anna, S.L. and H.C. Mayer, *Microscale tipstreaming in a microfluidic flow focusing device*. Physics of Fluids, 2006. **18**(12): p. 121512.
44. Lee, W., L.M. Walker, and S.L. Anna, *Role of geometry and fluid properties in droplet and thread formation processes in planar flow focusing*. Physics of Fluids, 2009. **21**(3).
45. Jeong, W.C., et al., *Controlled generation of submicron emulsion droplets via highly stable tip-streaming mode in microfluidic devices*. Lab on a Chip, 2012. **12**(8): p. 1446-1453.
46. Fernandez, J.M. and G.M. Homsy, *Chemical reaction-driven tip-streaming phenomena in a pendant drop*. Physics of Fluids, 2004. **16**(7): p. 2548-2555.
47. Ward, T., M. Faivre, and H.A. Stone, *Drop Production and Tip-Streaming Phenomenon in a Microfluidic Flow-Focusing Device via an Interfacial Chemical Reaction*. Langmuir, 2010. **26**(12): p. 9233-9239.

48. De Bruijn, R.A., *Tipstreaming of drops in simple shear flows*. Chemical Engineering Science, 1993. **48**(2): p. 277-284.
49. Taylor, G.I., *The formation of emulsions in definable fields of flow*. Proceedings of the Royal Society of London Series a-Mathematical and Physical Sciences, 1934. **146**(A858): p. 0501-0523.
50. Bazhekov, I.B., P.D. Anderson, and H.E.H. Meijer, *Numerical investigation of the effect of insoluble surfactants on drop deformation and breakup in simple shear flow*. Journal of Colloid and Interface Science, 2006. **298**(1): p. 369-394.
51. Krechetnikov, R., *Structure of Marangoni-driven singularities*. Physics of Fluids, 2012. **24**(2): p. 022111.
52. Lee, W., Walker, L. M., and Anna, S. L., *Competition Between Viscoelasticity and Surfactant Dynamics in Flow Focusing Microfluidics*. Macromolecular Materials and Engineering, 2011. **296**(3-4): p. 203-213.
53. Oliveira, M.S.N., R. Yeh, and G.H. McKinley, *Iterated stretching, extensional rheology and formation of beads-on-a-string structures in polymer solutions*. Journal of Non-Newtonian Fluid Mechanics, 2006. **137**(1-3): p. 137-148.
54. Bhat, P.P., et al., *Formation of beads-on-a-string structures during breakup of viscoelastic filaments*. Nature Physics, 2010. **6**(8): p. 625-631.
55. Collins, R.T., Jones, J. J., Harris, M. T., and Basaran, O. A., *Electrohydrodynamic tip streaming and emission of charged drops from liquid cones*. Nature Physics, 2008. **4**(2): p. 149-154.
56. Gundabala, V.R., N. Vilanova, and A. Fernandez-Nieves, *Current-Voltage Characteristic of Electrospray Processes in Microfluidics*. Physical Review Letters, 2010. **105**(15).
57. Forbes, T.P., F.L. Degertekin, and A.G. Fedorov, *Regime Transition in Electromechanical Fluid Atomization and Implications to Analyte Ionization for Mass Spectrometric Analysis*. Journal of the American Society for Mass Spectrometry, 2010. **21**(11): p. 1900-1905.
58. Gamero-Castano, M., *Energy dissipation in electrosprays and the geometric scaling of the transition region of cone-jets*. Journal of Fluid Mechanics, 2010. **662**: p. 493-513.
59. Gamero-Castano, M., *Characterization of the electrosprays of 1-ethyl-3-methylimidazolium bis(trifluoromethylsulfonyl) imide in vacuum*. Physics of Fluids, 2008. **20**(3).

60. Gu, J.B., et al., *DROPLET SIZE DISTRIBUTIONS OF ADJUVANT-AMENDED SPRAYS FROM AN AIR-ASSISTED FIVE-PORT PWM NOZZLE*. *Atomization and Sprays*, 2011. **21**(3): p. 263-274.
61. Shah, M., O. Galkin, and P.G. Vekilov, *Localized Generation of Attoliter Protein Solution Droplets by Electrofocused Liquid-Liquid Separation*. *Journal of Physical Chemistry B*, 2009. **113**(20): p. 7340-7346.
62. Tan, Y.C. and A.P. Lee, *Microfluidic separation of satellite droplets as the basis of a monodispersed micron and submicron emulsification system*. *Lab on a Chip*, 2005. **5**(10): p. 1178-1183.
63. Clampitt, R., *Advances in Molten-Metal Field-Ion Sources*. *Nuclear Instruments & Methods in Physics Research*, 1981. **189**(1): p. 111-116.
64. Grace, H.P., *DISPERSION PHENOMENA IN HIGH-VISCOSITY IMMISCIBLE FLUID SYSTEMS AND APPLICATION OF STATIC MIXERS AS DISPERSION DEVICES IN SUCH SYSTEMS*. *Chemical Engineering Communications*, 1982. **14**(3-6): p. 225-277.
65. Stone, H.A., B.J. Bentley, and L.G. Leal, *An Experimental-Study of Transient Effects in the Breakup of Viscous Drops*. *Journal of Fluid Mechanics*, 1986. **173**: p. 131-158.
66. Bentley, B.J. and L.G. Leal, *AN EXPERIMENTAL INVESTIGATION OF DROP DEFORMATION AND BREAKUP IN STEADY, TWO-DIMENSIONAL LINEAR FLOWS*. *Journal of Fluid Mechanics*, 1986. **167**: p. 241-283.
67. Rayleigh, L., *On the capillary phenomena of jets*. *Proceedings of the Royal Society of London*, 1879. **29**: p. 71-97.
68. Tomotika, S., *Breaking up of a drop of viscous liquid immersed in another viscous fluid which is extending at a uniform rate*. *Proceedings of the Royal Society of London Series a-Mathematical and Physical Sciences*, 1936. **153**(A879): p. 0302-0318.
69. Hardt, S., F. Jiang, and F. Schonfeld, *A computational analysis of the hydrodynamic instability of a liquid jet focused into a converging microchannel*. *International Journal of Multiphase Flow*, 2005. **31**(6): p. 739-756.
70. Janssen, P.J.A., Meijer, H. E. H., and Anderson, P. D., *Stability and breakup of confined threads*. *Physics of Fluids*, 2012. **24**(1): p. 012102.
71. Janssen, J.J.M., A. Boon, and W.G.M. Agterof, *Influence of dynamic interfacial properties on droplet breakup in plane hyperbolic flow*. *Aiche Journal*, 1997. **43**(6): p. 1436-1447.

72. Janssen, J.J.M., A. Boon, and W.G.M. Agterof, *Influence of dynamic interfacial properties on droplet breakup in simple shear flow*. *Aiche Journal*, 1994. **40**(12): p. 1929-1939.
73. Anna, S.L., N. Bontoux, and H.A. Stone, *Formation of dispersions using "flow focusing" in microchannels*. *Applied Physics Letters*, 2003. **82**(3): p. 364-366.
74. Lee, W., *Microscale thread formation as a mechanism to generate submicron droplets*, 2010, Ph.D. thesis, Department of Chemical Engineering, Carnegie Mellon University: Pittsburgh, PA. p. 186.
75. Lee, W., L.M. Walker, and S.L. Anna, *Competition Between Viscoelasticity and Surfactant Dynamics in Flow Focusing Microfluidics*. *Macromolecular Materials and Engineering*, 2011. **296**(3-4): p. 203-213.
76. Suryo, R. and O.A. Basaran, *Tip streaming from a liquid drop forming from a tube in a co-flowing outer fluid*. *Physics of Fluids*, 2006. **18**(8): p. 082102.
77. Krechetnikov, R. and G.M. Homsy, *On physical mechanisms in chemical reaction-driven tip-streaming*. *Physics of Fluids*, 2004. **16**(7): p. 2556-2566.
78. Milliken, W.J., H.A. Stone, and L.G. Leal, *The effect of surfactant on the transient motion of newtonian drops*. *Physics of Fluids A-Fluid Dynamics*, 1993. **5**(1): p. 69-79.
79. Milliken, W.J. and L.G. Leal, *The Influence of Surfactant on the Deformation and Breakup of a Viscous Drop - the Effect of Surfactant Solubility*. *Journal of Colloid and Interface Science*, 1994. **166**(2): p. 275-285.
80. Eggleton, C.D. and K.J. Stebe, *An adsorption-desorption-controlled surfactant on a deforming droplet*. *Journal of Colloid and Interface Science*, 1998. **208**(1): p. 68-80.
81. Eggleton, C.D., Y.P. Pawar, and K.J. Stebe, *Insoluble surfactants on a drop in an extensional flow: a generalization of the stagnated surface limit to deforming interfaces*. *Journal of Fluid Mechanics*, 1999. **385**: p. 79-99.
82. Eggleton, C.D., T.M. Tsai, and K.J. Stebe, *Tip streaming from a drop in the presence of surfactants*. *Physical Review Letters*, 2001. **87**(4): p. 048302.
83. Booty, M.R. and M. Siegel, *Steady deformation and tip-streaming of a slender bubble with surfactant in an extensional flow*. *Journal of Fluid Mechanics*, 2005. **544**: p. 243-275.

84. Flumerfelt, R.W., *Effects of Dynamic Interfacial Properties on Drop Deformation and Orientation in Shear and Extensional Flow-Fields*. Journal of Colloid and Interface Science, 1980. **76**(2): p. 330-349.
85. Stone, H.A. and L.G. Leal, *The Effects of Surfactants on Drop Deformation and Breakup*. Journal of Fluid Mechanics, 1990. **220**: p. 161-186.
86. Booty, M.R. and M. Siegel, *A hybrid numerical method for interfacial fluid flow with soluble surfactant*. Journal of Computational Physics, 2010. **229**(10): p. 3864-3883.
87. Wang, Q.M., M. Siegel, and M.R. Booty, *Numerical simulation of drop and bubble dynamics with soluble surfactant*. Physics of Fluids, 2014. **26**(5).
88. Tanyeri, M., E.M. Johnson-Chavarria, and C.M. Schroeder, *Hydrodynamic Trap for Single Cells and Micro- and Nanoparticles*. Biophysical Journal, 2011. **100**(3): p. 623-623.
89. Tanyeri, M., et al., *A microfluidic-based hydrodynamic trap: design and implementation*. Lab on a Chip, 2011. **11**(10): p. 1786-1794.
90. Maddala, J., et al., *Design of a model-based feedback controller for active sorting and synchronization of droplets in a microfluidic loop*. Aiche Journal, 2012. **58**(7): p. 2120-2130.
91. Kuczynski, B., P.R. LeDuc, and W.C. Messner, *Pressure-driven spatiotemporal control of the laminar flow interface in a microfluidic network*. Lab on a Chip, 2007. **7**(5): p. 647-649.
92. Lao, A.I.K., et al., *Precise temperature control of microfluidic chamber for gas and liquid phase reactions*. Sensors and Actuators a-Physical, 2000. **84**(1-2): p. 11-17.
93. de Mello, A.J., et al., *Precise temperature control in microfluidic devices using Joule heating of ionic liquids*. Lab on a Chip, 2004. **4**(5): p. 417-419.
94. Welch, D. and J.B. Christen, *Real-time feedback control of pH within microfluidics using integrated sensing and actuation*. Lab on a Chip, 2014. **14**(6): p. 1191-1197.
95. Eddington, D.T., et al., *An organic self-regulating microfluidic system*. Lab on a Chip, 2001. **1**(2): p. 96-99.
96. Juarez, J.J., et al., *Multiple electrokinetic actuators for feedback control of colloidal crystal size*. Lab on a Chip, 2012. **12**(20): p. 4063-4070.
97. Shih, S.C.C., et al., *A feedback control system for high-fidelity digital microfluidics*. Lab on a Chip, 2011. **11**(3): p. 535-540.

98. Gong, J. and C.J. Kim, *All-electronic droplet generation on-chip with real-time feedback control for EWOD digital microfluidics*. *Lab on a Chip*, 2008. **8**(6): p. 898-906.

CHAPTER 3**MATERIALS AND METHODS****3.1 DEVICE DESIGN AND FABRICATION**

Tipstreaming at the microscale is accomplished with the aid of a flow-focusing geometry, shown in Figure 3.1 a. In this geometry, the dispersed phase and continuous phase liquids flow into three separate microchannels. These three channels merge and the immiscible liquids are forced to flow through an orifice. The geometry results in an elongational flow field that promotes pinch-off of the dispersed phase into droplets. The volumetric flow rates, liquid viscosities, and the presence of surfactant, have all been shown to influence the mode of droplet breakup[1-4].

The tipstreaming mode of droplet breakup is observed when operating a flow-focusing device within a specific range of bulk surfactant concentrations, continuous phase flow rates, and flow rate ratios[5, 6]. When the phenomenon is observed, a thin thread of dispersed phase liquid is generated from the pointed tip of a nearly stationary larger drop of dispersed phase liquid held just upstream of the contraction. The thread breaks up into micron scale droplets. The thread generation is periodically interrupted by the production of larger primary drops, as shown in Figure 3.1 b. During thread formation, the pointed tip of the upstream interface is highly curved and its shape remains approximately stationary.

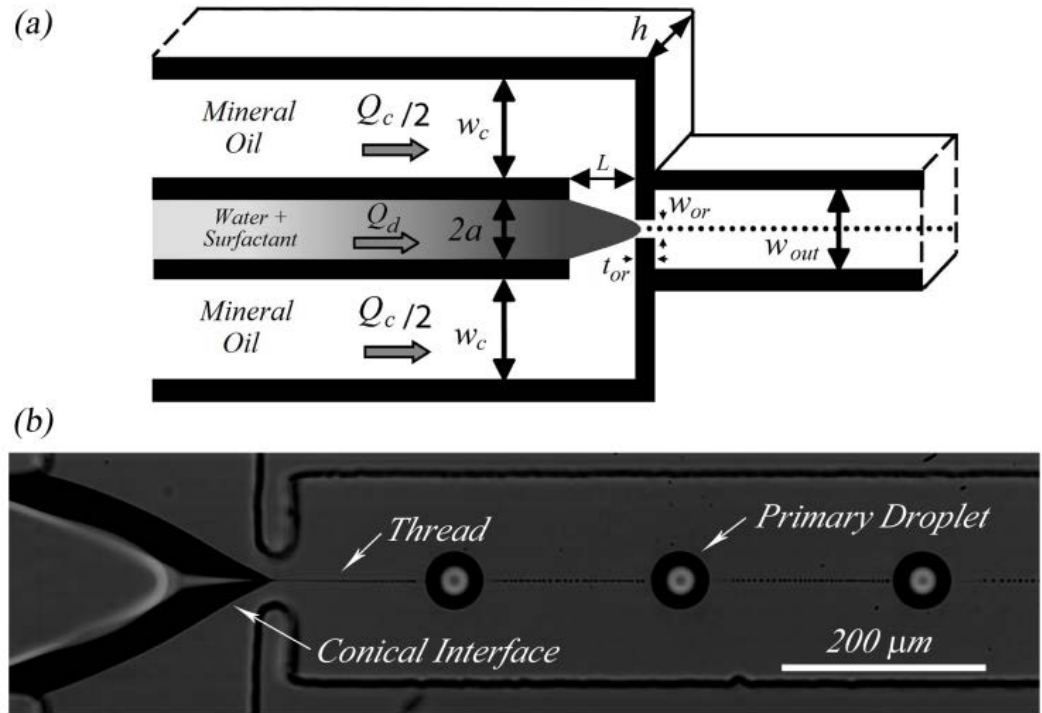


Figure 3.1 (a) Schematic diagram of planar microfluidic flow focusing geometry. The continuous phase, mineral oil, flows into both of the outer channels with width w_c at a volumetric flow rate of $Q_c/2$. The dispersed phase liquid, water containing dissolved $C_{12}E_8$, flows into the inner channel with width $2a$ at a flow rate of Q_d . The three channels merge at a distance L upstream of the orifice. The two immiscible liquids flow together through the orifice with width w_{or} . The resulting droplet stream exits into an exit channel of width w_{out} . The entire device has a uniform depth h . (b) Image of interfacial shape, thread, and primary droplets during tipstreaming.

Experiments considered in this study all use a planar microfluidic flow-focusing geometry. Microfluidic flow focusing devices are fabricated using standard soft lithography techniques[7, 8]. In this method, a negative mold of the microfluidic channel network is first generated. This mold is fabricated on a 3” silicon wafer (Cz growth method, P/Boron dopant, one side polish, 1-10 Ω -cm resistivity, 15 ± 2 mils). First, the wafer is cleaned in a three step process of sequential rinsing with acetone, isopropanol and deionized water. This process is repeated three time to ensure the wafer is clean. A layer of UV curable SU-8 3050

(Microchem Corp.) photoresist epoxy is then spin coated on to the wafer. The spin coater (Laurell Technologies 150 mm Spin Coater Model WS-650Mz-23NPP) settings are selected to produce a constant film thickness of 155 microns. This requires a two cycle spin coat. The first cycle is at 500 RPM with a ramp speed of 85 RPM/s and a time of 20 seconds. The second cycle is at 1000 RPM with a ramp speed of 340 RPM/s and a time of 30 seconds. Actual measurements of the mold and devices are subsequently used to determine the exact height of the device channels.

A soft bake of the wafer is then performed to remove excess solvent from the photoresist layer, increasing the resolution of the lithography process. The wafer is heated on a temperature controlled hotplate to 65°C at a rate of 300°C/hr and held there for 5 minutes. The temperature is then increased to 95°C, heated at a rate of 300°C/hr, and held at the new temperature for 15 minutes. During the soft bake, the wafer is rotated by 90° every 3 minutes to ensure an even heat distribution.

Lithography masks for the microfluidic network are designed using DraftSight (Dassault Systèmes) to generate a CAD drawing of the flow focusing geometry diagramed in Figure 3.1. The design is commercially printed (CAD/Art Services, Inc.) on a transparency at 20,000 dpi resolution. The mask is aligned on top of the wafer once it has completed the soft bake and cooled to room temperature. A light filter is placed on top of the wafer and mask to eliminate wavelengths from the UV light source below 380 nm. This prevents uneven curing and promotes uniform channel walls. A UV light source (OAI 150 200W UV Exposure System,

3.14 mW) is used to cure the epoxy exposed by the mask for 90 seconds. The UV exposure generates free radicals within the epoxy.

A post bake is then performed, reacting the epoxy and free radicals, to generate a negative of the microfluidic network. The post bake uses a similar temperature ramping procedure. The temperature is again set to 65°C at a rate of 300°C/hr and, once reached, held there for 1 minute, after which the temperature is increased to 95°C at a rate of 300°C/hr and held there for 5 minutes. Once the post bake is completed, the unreacted SU-8 is removed by placing the wafer in a container with circulating SU-8 Developer (Microchem Corp.) for 30 minutes. The cured SU-8 pattern remains behind, bonded to the silicon wafer surface. Finally, the mold is rinsed with isopropanol to remove any developer and given 24 hours to fully cure before use.

The microfluidic devices are fabricated in poly(dimethylsiloxane) (PDMS) (Dow Sylgard 184). The uncured PDMS oligomer and catalyst are mixed together in a ratio of 10:1 and poured onto the mold generated from the soft lithography process. The PDMS and mold are placed into a 60°C oven for 3 hours to cure. Once cured, the patterned device can be removed from the mold. The molded channels are bonded to a flat PDMS slab via an air plasma bonding procedure[7]. This ensures that all four channel walls have identical wetting behavior. The plasma bonding procedure produces a hydrophilic surface on the PDMS[9, 10]. To aid the production of water in oil emulsions, a hydrophobic surface is desired. The hydrophobic nature of the PDMS is recovered by heating the bonded device to 180 °C for 1 hour[11].

Dimensions within the 2D lateral plane, see Figure 3.1 a, of the device are measured optically. The continuous phase oil has the potential to swell PDMS and alter the geometry. To account for this effect, oil is allowed to flow through all channels for 30 minutes before lateral geometry measurements are taken. The dimensions after swelling are listed in Table 3.1. Camera resolution limits the uncertainty to $\pm 1 \mu\text{m}$ for the values reported in the table. The uniform depth of the device, also given in Table 3.1, is measured prior to bonding using a contact profilometer (Veeco Dektak) with an uncertainty of $\pm 5 \mu\text{m}$. PDMS swelling is assumed to have a negligible influence on the device depth. The hydraulic diameter of the orifice, $D_H = 2w_{or}h / (w_{or} + h)$, is also reported in Table 3.1.

Table 3.1. Geometry, fluid, and surfactant properties for microscale tipstreaming experiments reported here. Geometric dimensions are measured as described in the text. Viscosity and density values are as reported the by manufacturer. Surface tension and surfactant molecular properties are taken from [12].

Property Description	Symbol	Value
<i>Geometric Dimensions</i>		
Width of continuous phase feed channels	w_c	285 μm
Half width of dispersed phase feed channel	a	94 μm
Length from channel merge point to orifice	L	230 μm
Width of orifice	w_{or}	38 μm
Width of outlet channel	w_{out}	195 μm
Thickness of orifice	t_{or}	20 μm
Depth of microchannel	h	141 μm
Hydraulic diameter of the orifice	D_H	60 μm
<i>Fluid Properties</i>		
Viscosity of continuous phase	μ_o	40 cP
Viscosity of dispersed phase	μ_i	1 cP
Ratio of water to oil viscosities	λ	0.025
Density of continuous phase	ρ_o	830 kg/m^3
Density of dispersed phase	ρ_i	1000 kg/m^3
Oil-water clean interfacial tension	γ_0	62 mN/m
<i>Surfactant Properties</i>		
Maximum interfacial surfactant packing concentration	Γ_∞	2.25 $\mu\text{mol/m}^2$
Generalized Frumkin van der Waals interaction parameter	κ	10.3
Generalized Frumkin nonlinear fitting parameter	n	0.460
Kinetic desorption rate constant	α	$6.86 \times 10^{-6} \text{ s}^{-1}$
Kinetic adsorption rate constant	β	22.1 $\text{m}^3/(\text{s mol})$

3. 2 STEADY STATE TIPSTREAMING MATERIALS

De-ionized water is the dispersed phase liquid for all experiments. The continuous phase liquid is light mineral oil (Fisher Scientific O1211). Liquid properties, viscosity ratio, and the clean interfacial tension value, γ_0 , for these liquids are given in Table 3.1 [6]. Two syringe pumps (Harvard Apparatus PHD2000) independently control the flow rates of each liquid phase. A Y-fitting (Small Parts) splits the oil flow to the two continuous phase feed channels in the device. Droplet breakup is visualized and recorded using an inverted microscope (Nikon Ti-U) with an attached high speed camera (Phantom v9.1). For all experiments considered here, the ratio of the dispersed to continuous phase volumetric flow rates is small $\varphi \equiv Q_d / Q_c \leq 1 / 40$. For thread formation, it has been established that the flow ratio must be small, $\varphi \ll 1$ [5]. This ratio was selected because it has been used in other experimental parametric studies of tipstreaming [5, 6]. Unless otherwise noted, the non-ionic, water-soluble surfactant, octaethylene glycol monododecyl ether ($C_{12}E_8$) (Sigma Aldrich P8925-1G, used as received), is used at various concentrations dissolved in the dispersed phase liquid.

3. 3 CONTROLLED THREAD FORMATION MATERIALS

The microfluidic devices used in the controlled experiments of Chapter 5 are fabricated using methods and device designs identical to those previously described in this Chapter. The dispersed and continuous phase liquids are supplied to the device using two different delivery methods. The continuous phase liquid, light mineral oil (Fisher Scientific O1211) containing dissolved Span 80 (Sigma

Aldrich S6760, used as received), is supplied via two syringe pumps (Harvard Apparatus PHD2000) each containing separate 60 ml syringes. The total flow rate of the continuous phase liquid into the device, Q_c , is kept constant at $Q_c = 100 \mu\text{l}/\text{min}$ for all controller experiments. The concentration of Span 80 in the oil phase is kept fixed at $C_{\text{Span 80}} = 1.8 \times 10^{-3} \text{ mol/l}$ for all controller experiments. These operating conditions are selected because they are comparable to reported steady state tipstreaming conditions for a similar oil-water-surfactant system[13]. Note that in Ref. [13], Span 80 concentrations are reported erroneously in units of μM and should be reported as mM . The present conditions are also similar to tipstreaming conditions reported for other surfactants[14, 15].

The dispersed phase liquid is supplied to the device through a pressurized reservoir consisting of a 500 ml Pyrex® container. Two holes are drilled in the plastic screw cap lid with 1/4 in OD stainless steel tubing inserted into each hole and fixed in place with epoxy cement to create an airtight seal. Swagelok® fittings (1/4 in stainless steel female connector) are attached at the ends of the tubing. Attached to the fittings are adapters to female Luer-Lock® fittings where syringe needles can be attached. The reservoir is filled to a volume of approximately 250 ml with the dispersed phase liquid (deionized water). A short section of tubing is fitted onto the needle on the interior of the container with the other end submerged in the dispersed phase liquid. The exterior needle is fitted with a longer section of tubing connected to the microfluidic device. The remaining exterior Luer-Lock® fitting is connected to an electric-to-pneumatic transducer (ControlAir

Inc. Type 550X) using 1/4 in OD plastic tubing and an additional Luer-Lock® fitting. This allows the pressure within the vessel to be controlled via electrical signal to the electric-to-pneumatic transducer. The transducer is supplied with 60 psi of pressure from a compressed nitrogen gas cylinder. This delivery method allows for a simple electrical signal generated by LabVIEW (National Instruments Corp., Austin, TX) to regulate the pressure of the vessel and thus alter the flow rate of the dispersed phase liquid into the device[16].

3.4 IMAGE ANALYSIS OF DROP SIZE

Drop sizes are determined using a custom image analysis technique to determine drop diameter as a function of the position in the drop stream. Images of the drops resulting from thread breakup are first taken on chip during a steady state tipstreaming experiment. This is accomplished using the same inverted microscope and attached high speed camera previously described. To obtain accurate sizes, images are recorded at 30x magnification using a 15 microsecond camera exposure time and the highest light intensity available. Analysis of the images begins by determining the number of frames between subsequent threads. The tipstreaming process is highly regular resulting in a constant number of video frames between subsequent threads. The number of frames between threads is determined manually for a given set of experimental conditions. Image analysis is only performed once per thread, thus the frames in-between threads are removed.

Once the non-analyzed images are removed, individual image analysis begins. The image analysis program vertically scans each pixel row in an image to

determine the vertical light intensity profile. The curvature of the drop interface causes diffraction of light resulting in sharp decreases in the light intensity. For each row, a thresholding criteria is used to determine if a droplet is located in a given row of pixels. The minimum intensity must be ten percent lower than the average background intensity for a drop to be considered present in the pixel row. Pixel rows without drops are used to indicate spaces between different drops in the thread.

Droplets span multiple vertical pixel rows in an image. Thus, multiple cross sectional measurements are made for each drop. However, the actual drop diameter must be measured through the drop center. The vertical pixel row which measures the drop center yields the maximum measured cross section distance for a given drop. Thus, the drop diameter is defined as the maximum measured drop cross section. Figure 3.2 shows a characteristic light intensity profile for a droplet 27 pixels in diameter.

The size of the drop is determined by the number of pixels between the first and last sharp intensity change, indicated by the black points. The exact values are measured from where the intensity profile obtains a value halfway between the average background intensity and the minimum intensity of the image. Converting from pixel length to microns requires a conversion factor. The physical distance a pixel covers is measured independently using a stage micrometer. For 30x magnification, the measured conversion factor is 0.37 microns per pixel ± 0.1 microns per pixel. One entire thread is contained within a single video frame. As a result, droplet diameter as a function of position within the original thread can be

easily determined. Once the entire thread is analyzed, results are recorded and analysis of the subsequent thread begins. For measurements presented in this work, a minimum of one hundred threads are analyzed for each set of conditions reported. Typically this includes diameter measurements of 1500 to 2500 droplets.

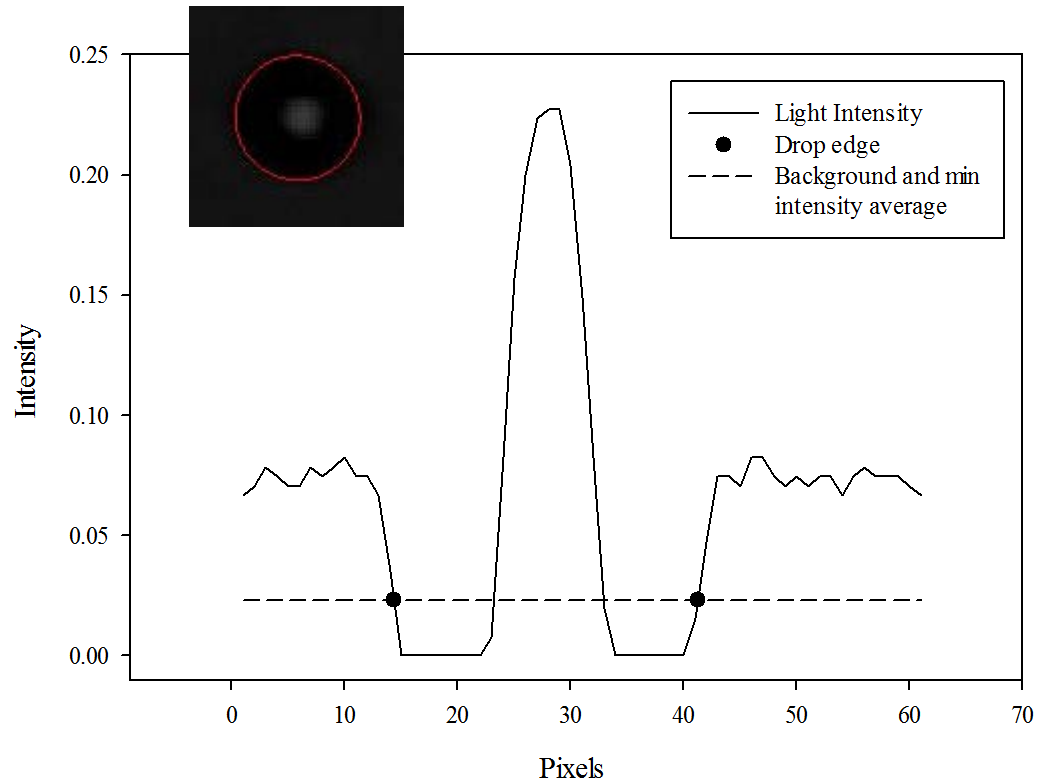


Figure 3.2 Light intensity profile for a droplet measured at the drop center. The solid line represents the measured light intensity profile, the ● points represents the measured droplet edges, and the -- line represents the average between the average background intensity and the minimum intensity, in this case zero. The inset is the image of the drop being analyzed. The ring indicates the fitted diameter based on the measured diameter.

1. Ganan-Calvo, A.M. and P. Riesco-Chueca, *Jetting-dripping transition of a liquid jet in a lower viscosity co-flowing immiscible liquid: the minimum flow rate in flow focusing*. Journal of Fluid Mechanics, 2006. **553**: p. 75-84.
2. Garstecki, P., et al., *Formation of droplets and bubbles in a microfluidic T-junction - scaling and mechanism of break-up*. Lab on a Chip, 2006. **6**(3): p. 437-446.
3. Utada, A.S., Fernandez-Nieves, A., Stone, H. A., and Weitz, D. A., *Dripping to jetting transitions in coflowing liquid streams*. Physical Review Letters, 2007. **99**(9): p. 094502.
4. Anna, S.L., N. Bontoux, and H.A. Stone, *Formation of dispersions using "flow focusing" in microchannels*. Applied Physics Letters, 2003. **82**(3): p. 364-366.
5. Anna, S.L. and H.C. Mayer, *Microscale tipstreaming in a microfluidic flow focusing device*. Physics of Fluids, 2006. **18**(12): p. 121512.
6. Lee, W., L.M. Walker, and S.L. Anna, *Role of geometry and fluid properties in droplet and thread formation processes in planar flow focusing*. Physics of Fluids, 2009. **21**(3).
7. Duffy, D.C., et al., *Rapid prototyping of microfluidic systems in poly(dimethylsiloxane)*. Analytical Chemistry, 1998. **70**(23): p. 4974-4984.
8. Whitesides, G.M. and A.D. Stroock, *Flexible methods for microfluidics*. Physics Today, 2001. **54**(6): p. 42-48.
9. Bhattacharya, S., Datta, A., Berg, J. M., and Gangopadhyay, S., *Studies on surface wettability of poly(dimethyl) siloxane (PDMS) and glass under oxygen-plasma treatment and correlation with bond strength*. Journal of Microelectromechanical Systems, 2005. **14**(3): p. 590-597.
10. Bormashenko, E., et al., *Physical mechanisms of interaction of cold plasma with polymer surfaces*. Journal of Colloid and Interface Science, 2015. **448**(0): p. 175-179.
11. Hillborg, H., et al., *Crosslinked polydimethylsiloxane exposed to oxygen plasma studied by neutron reflectometry and other surface specific techniques*. Polymer, 2000. **41**(18): p. 6851-6863.
12. Alvarez, N.J., Lee, W., Walker, L. M., and Anna, S. L., *The effect of alkane tail length of C(i)E(8) surfactants on transport to the silicone oil-water interface*. Journal of Colloid and Interface Science, 2011. **355**(1): p. 231-236.

13. Lee, W., Walker, L. M., and Anna, S. L., *Competition Between Viscoelasticity and Surfactant Dynamics in Flow Focusing Microfluidics*. *Macromolecular Materials and Engineering*, 2011. **296**(3-4): p. 203-213.
14. Lee, W., *Microscale thread formation as a mechanism to generate submicron droplets*, 2010, Ph.D. thesis, Department of Chemical Engineering, Carnegie Mellon University: Pittsburgh, PA. p. 186.
15. Moyle, T.M., L.M. Walker, and S.L. Anna, *Predicting conditions for microscale surfactant mediated tipstreaming*. *Physics of Fluids*, 2012. **24**(8): p. 082110-21.
16. Ward, T., et al., *Microfluidic flow focusing: Drop size and scaling in pressure versus flow-rate-driven pumping*. *Electrophoresis*, 2005. **26**(19): p. 3716-3724.

CHAPTER 4**A MODEL TO PREDICT OPERATING CONDITIONS FOR
MICROSCALE TIPSTREAMING****4.1 INTRODUCTION**

Monodisperse droplets smaller than 1 μm in diameter have the potential to be more effective for applications than larger droplets created with traditional microfluidic techniques[1]. However, soft lithography mold fabrication typically limits the smallest diameter of these droplets to greater than 10 μm [2-6]. Micron-sized droplets in microfluidic flows have been produced using a surfactant-mediated tipstreaming mechanism[7-10]. Although the basic mechanism has been validated through experiments and numerical simulations, there is little understanding of how to obtain tipstreaming and control the droplet size for arbitrary surfactant-oil-water systems. There are no simple analytical models or scaling relationships that can enable design and control of the process. The goal of this work is to develop a semi-analytical model and scaling approximations that are able to predict the surfactant concentrations and liquid flow rates that result in microscale tipstreaming.

In this Chapter, we will use a combination of experimental observation and dimensional analysis to develop a simplified model describing the boundaries of the operating space in which tipstreaming occurs. We present microscale tipstreaming experiments and describe the conditions at which the phenomenon is observed. We then outline the dimensional analysis that allows for simplifications to the governing equations and boundary conditions. We use these simplifications to develop a semi-analytical model for the conditions at which tipstreaming can

occur, along with approximate scaling arguments representing the primary phase boundaries. We compare predictions with experiments and discuss implications of our results.

4.2 EXPERIMENTALLY GENERATED OPERATING DIAGRAMS FOR TIPSTREAMING

Experimental procedures and techniques used for experiments presented here are described in Chapter 3 of this work. The $C_{12}E_8$ surfactant is selected because the relevant molecular parameters for adsorption at the oil-water interface have been measured[11]. The relationship between surface tension and bulk concentration for $C_{12}E_8$ is well characterized by the generalized Frumkin isotherm model for both air-water and oil-water interfaces[11-14]. The generalized Frumkin isotherm is given by

$$\hat{\Gamma} = \frac{1}{1 + \frac{\alpha}{\beta C_{\infty}} \exp(\kappa(\hat{\Gamma})^n)} , \quad (4.1)$$

where α , β , κ , and n are defined in Table 3.1 . Here, $\hat{\Gamma} \equiv \Gamma / \Gamma_{\infty}$ is the dimensionless interfacial surfactant concentration normalized by the maximum packing interfacial concentration. $C_{12}E_8$ surfactant property values at the oil-water interface are taken from[11] and listed in Table 3.1. Bulk surfactant concentrations, C_{∞} , of $15\mu\text{M}$ (1.5×10^{-5} mol/l) to 1.5 mM (1.5×10^{-3} mol/l) are used. The presence of surfactant at these concentrations does not significantly alter the dispersed phase viscosity.

A series of experiments are performed varying bulk surfactant concentration and volumetric flow rates. All experiments presented in this Chapter use a flow rate ratio value of $\phi = 1/40$. At each flow rate, the conditions are held constant for 30 minutes prior to analysis. The amount of time was selected because visible changes in droplet formation could be noticed up to 15 minutes after flow rates were altered. Thus, double this time was used to ensure the system was at steady state. Droplet breakup is designated as either tipstreaming or another breakup mode[7]. We apply specific criteria to determine whether tipstreaming is exhibited at a given set of conditions. Tipstreaming is defined as the formation of a very thin thread pulled from the pointed tip of the liquid-liquid interface. The high degree of curvature means the interface must maintain a cone-like shape during thread formation. Maintaining this conical interfacial shape for enough time to form a thread that breaks up into multiple droplets is necessary for a breakup mode to be considered tipstreaming. Formation of a thread that only forms a single satellite droplet is not defined as tipstreaming.

Flow focusing experiments are used to determine an experimental operating diagram delineating conditions at which microscale tipstreaming occurs. Volumetric flow rates are tested sequentially at a given surfactant concentration, increasing in magnitude from low to high values. At several concentrations, experiments are repeated from high to low flow rate values to check for hysteresis effects, and none are observed. The break up mode is designated as either tipstreaming or another breakup mode based on criteria described above. The resulting operating diagram for the flow focusing geometry and $C_{12}E_8$ surfactant

solution is given in Figure 4.1. This figure is a plot of bulk surfactant concentration versus outer phase volumetric flow rate. The solid square symbols represent conditions at which tipstreaming is observed while open symbols represent conditions at which a different mode of droplet breakup is exhibited. The total outer phase liquid flow rate in these experiments is 40 times greater than the inner phase liquid flow rate.

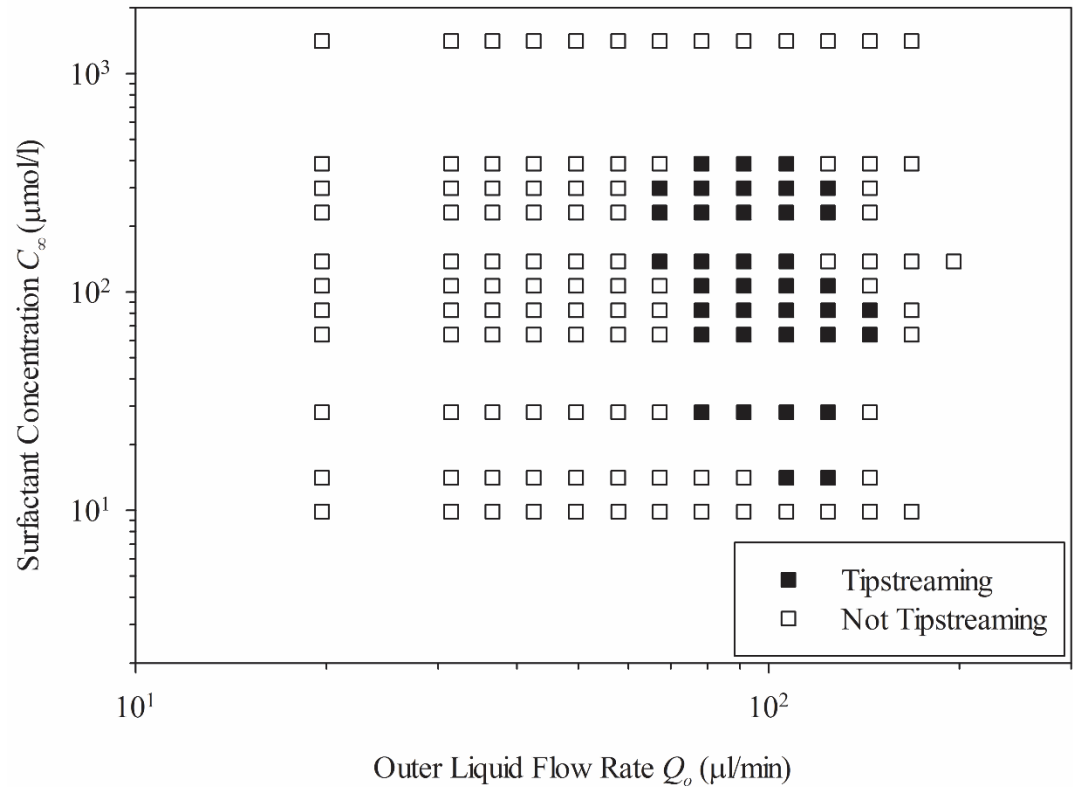


Figure 4.1. Experimentally observed conditions corresponding to tipstreaming (■) and non-tipstreaming break up modes (□) as defined in the text at specific outer liquid flow rate and surfactant concentration values.

Results indicate a bounded region in which tipstreaming is observed to occur. In tipstreaming, the outer phase liquid flow rate bounds are $64 < Q_o < 144$ $\mu\text{l/min}$. The surfactant concentration bounds are $10 < C_\infty < 400$ $\mu\text{mol/l}$. Outside

the tipstreaming region, other droplet breakup modes occur and have been studied previously[7, 15, 16]. The conditions that result in tipstreaming are comparable to those previously reported for microscale tipstreaming with C₁₂E₈ surfactant[7, 8]. Figure 4.1 is an experimental tipstreaming operating diagram specific to this combination of surfactant, device geometry and liquid pair. A model that can define the boundaries of the tipstreaming region would reduce testing needed to determine the influence of altering these parameters, and would help to generalize the results for arbitrary surfactant-oil-water systems.

4.3 MODELING INTERFACIAL FLOWS

Interfacial flows coupled with adsorbed interfacial surfactant and surfactant transport have been modeled previously[17-22]. Our governing equations describing fluid flow, interfacial boundary conditions, and surfactant transport for microscale tipstreaming are identical to those used in the previous studies. However, our choice of scaling variables differs slightly to better reflect the relevant experimental conditions. At experimental microscale tipstreaming conditions, the Reynolds number $Re \equiv (\rho_o a V) / \mu_o$ is $0.3 < Re < 0.8$ calculated using an average velocity through the orifice $V = Q_o / (w_o h)$ based on the continuous phase volumetric flow rate and the droplet length scale a . Additionally, both inner and outer phases are assumed to be Newtonian liquids. Therefore, we assume that fluid flow in both the inner and outer liquids can be described by the Stokes equations and continuity in the two phases, given by

$$\hat{\nabla}^2 \hat{\mathbf{v}}_i = \hat{\nabla} \hat{p}_i, \quad \hat{\nabla} \cdot \hat{\mathbf{v}}_i = 0, \quad (4.2)$$

$$\hat{\nabla}^2 \hat{\mathbf{v}}_o = \hat{\nabla} \hat{p}_o, \quad \hat{\nabla} \cdot \hat{\mathbf{v}}_o = 0, \quad (4.3)$$

where $\hat{\mathbf{v}}$ is the dimensionless velocity and \hat{p} is the dimensionless pressure, as denoted by the overhat. The velocity is normalized by the average velocity through the orifice, V . The pressure is scaled by the viscous scaling $(\mu V)/a$ where μ_i is used for the inner phase and μ_o is used for the outer phase scaling. The gradients ∇ are scaled using the upstream capillary length a .

Continuity of velocity at the liquid-liquid interface requires the inner and outer phase fluid velocities to be equal at every point on the interface. Additionally, a stress balance on the interface requires

$$\frac{\mu_o a G}{RT\Gamma_\infty} \left(\underline{\hat{\mathbf{T}}^o} - \lambda \underline{\hat{\mathbf{T}}^i} \right) \cdot \mathbf{n} + \hat{\nabla}_s \hat{\gamma} - \hat{\gamma} \mathbf{n} \left(\hat{\nabla}_s \cdot \mathbf{n} \right) = 0. \quad (4.4)$$

Here, $\underline{\mathbf{T}}$ is the stress tensor, γ is the interfacial tension, \mathbf{n} is the unit normal vector for the interface pointing outward into the continuous phase, ∇_s is the surface gradient operator, R is the ideal gas constant, and T is the temperature. The convective time scale, G^{-1} , is given by a , the characteristic radius of the interface, divided by the average velocity in the orifice, $G^{-1} \equiv (aw_{or}h)/Q_o$. The stress tensors are normalized by μG with the inner and outer stress tensors using the inner and outer viscosities respectively. Surface gradients scale with the upstream capillary length a . The equilibrium interfacial tension value, γ_{Eq} , is commonly used to scale the interfacial tension in the literature [19]. However, we have chosen to scale interfacial tension by $RT\Gamma_\infty$ since this characteristic value arises from scaling the generalized Frumkin equation of state and represents the maximal change in

interfacial tension that may arise when interfacial tension gradients develop on the interface. The normalization of Eq. (4.4) described above leads to the appearance of the dimensionless parameter $\text{Ma} \equiv (\text{RT}\Gamma_\infty) / (\mu_o a G)$, which is the ratio of the convection time scale G^{-1} to the surface relaxation time scale $(\mu_o a) / (\text{RT}\Gamma_\infty)$ also known as the solutal Marangoni number [23].

The interfacial tension is related to the interfacial surfactant concentration and is therefore coupled with surfactant transport through an interfacial equation of state. The generalized Frumkin equation of state is given by

$$\hat{\gamma} - \frac{\gamma_0}{\text{RT}\Gamma_\infty} = \left[\ln(1 - \hat{\Gamma}) - \frac{\kappa n}{n+1} (\hat{\Gamma})^{n+1} \right], \quad (4.5)$$

where γ_0 , κ , and n are defined in Table 3.1 . The interfacial surfactant concentration is governed by an evolution equation arising from the interfacial surfactant mass balance written as

$$\frac{\partial \hat{\Gamma}}{\partial \hat{t}} + \hat{\mathbf{V}}_s \cdot (\hat{\Gamma} \hat{\mathbf{v}}) + 2\hat{H} (\mathbf{n} \cdot \hat{\mathbf{v}}) \hat{\Gamma} - \frac{1}{\text{Pe}_s} \hat{\mathbf{V}}_s^2 \hat{\Gamma} = \frac{j_n}{\Gamma_\infty G} \quad (4.6)$$

where $\hat{\mathbf{v}}$ is the interfacial velocity normalized by the average velocity within the orifice V , t is normalized by the convective time scale, G^{-1} , \hat{H} is the mean interfacial curvature normalized by the inverse of the capillary radius, a^{-1} , and j_n is the flux of surfactant to the interface from the bulk. Though Eq. (4.1) describes the interfacial surfactant coverage at equilibrium, Eq. (4.6) is required to describe the dynamics of the interface. Bulk and surface Péclet numbers, Pe and Pe_s , are defined as[19]

$$\text{Pe} = \frac{a^2 G}{D}; \quad \text{Pe}_s = \frac{a^2 G}{D_s}, \quad (4.7)$$

where D is the bulk diffusivity and D_s is the surface diffusivity, which is assumed to be of the same order of magnitude as the bulk diffusivity for soluble surfactants[24, 25]. The flux of surfactant from the bulk, j_n , is governed by serial processes of advection-diffusion, $j_n = -D\mathbf{n} \cdot \nabla C|_s$ and adsorption-desorption kinetics [26], described by the generalized Frumkin rate equation, $j_n = \Gamma_\infty [\beta C(1 - \hat{\Gamma}) - \alpha \hat{\Gamma} \exp(\kappa \hat{\Gamma}^n)]$ which is obtained from an Arrhenius rate formulation similar to that of the Frumkin rate equation[27]. Here, C is the local surfactant concentration in bulk. The Biot number is the ratio of the convective time scale, G^{-1} and the time scale for desorption, α^{-1} [19].

Eggleton *et al.* have argued that surfactant transport to an interface is kinetically controlled if $\text{Bi}(\text{Pe}\delta) \ll 1$, where δ is the normalized planar depletion depth, $\delta \equiv \Gamma_\infty / C_\infty a$ [19]. Experimentally, microscale tipstreaming occurs at very small values of this parameter group, $10^{-6} < \text{Bi}(\text{Pe}\delta) < 10^{-3}$, using the parameter values listed in Table 3.1. This indicates that kinetic rates of adsorption are significantly slower than those of diffusion during microscale tipstreaming. As a result, surfactant concentration gradients within the bulk fluid are neglected and the concentration adjacent to the interface is assumed equal to the bulk concentration. The time scale for soluble surfactant kinetics has been developed by Pan *et al.*[27]. For C_{12}E_8 , adsorption kinetics are much faster than desorption kinetics, $\beta C_\infty \gg \alpha$. Additionally, the experimental convection rate for tipstreaming is orders of

magnitude larger than the desorption rate. This indicates that surfactant will be convected off the interface onto a thread or primary drop before it has time to desorb from the interface. As a result, the flux of surfactant onto the interface can be simplified to $j_n = \beta C_\infty \Gamma_\infty (1 - \hat{\Gamma})$. Thus desorption is neglected and the kinetic time scale simplifies to the adsorption time scale $(\beta C_\infty)^{-1}$.

Although these considerations of kinetic, diffusion, and convection time scales allow for some simplifications in Eq. (4.6), solving Eqs. (4.1) through (4.6) simultaneously remains difficult due to the spatial and temporal dependence of the interfacial shape and the surfactant concentration. A primary difficulty in solving these equations lies in the unknown interfacial shape and the coupling of shape deformations with the flow field. However, during thread formation in microscale tipstreaming, the interfacial shape is observed to remain approximately stationary. This observation is used to simplify the governing equations for a fixed interfacial shape.

The goal of this analysis is to determine conditions at which tipstreaming can occur. Rather than seeking a solution to the governing fluid dynamics equations, we seek to describe conditions at which the key features of tipstreaming can be obtained. A unique feature of tipstreaming that is not seen in any other droplet break up mode is that the interface establishes a stationary conical shape from which a thin thread is emitted, as shown in Fig. 1b. In what follows, we seek conditions that allow a conical interface to be maintained. Note that the equations used to develop the following model are expressed in dimensional form for simplicity.

We assume that the interface is a right circular cone with apex angle θ_c . We model the conical shape in axisymmetric spherical coordinates, placing the origin at the projected cone apex. The device geometry and conical interface shape are shown in the axisymmetric coordinate system in Figure 4.2. The location of the origin is determined by the cone apex angle, θ_c , since the opening of the cone is pinned upstream at the end of the dispersed phase feed channel.

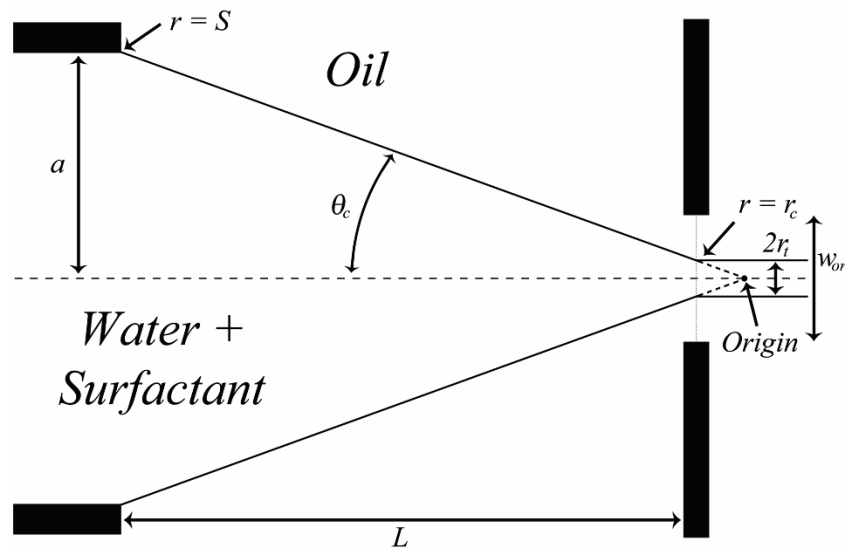


Figure 4.2. Schematic diagram illustrating the geometry used to model the interfacial shape during thread formation. The interfacial geometry and coordinate system are assumed to be axisymmetric about the center axis.

In this coordinate system, maintaining the conical shape requires the interfacial velocity to be purely radial. To alleviate velocity and stress singularities arising as $r \rightarrow 0$, we impose a cut off radius r_c , mimicking the experimentally observed cone-to-thread transition that occurs near the middle of the orifice. Therefore, the interface is located at a constant angle $\theta = \theta_c$ and is defined radially from $r = S$, the point on the interface where the three phase contact line is pinned

at the end of the inner channel upstream of the orifice, to the cut off radius r_c . Defining the cut off radius at the center of the orifice relates the cone apex angle θ_c to r_c , and the thread radius r_t geometrically. However, the value of θ_c is unknown and must be determined by imposing additional physical constraints.

To maintain the conical shape, the normal and tangential stresses on the interface must balance. The velocity field near the conical interface needs to be known to determine the viscous stresses acting on the interface. Creeping flow in axisymmetric spherical coordinates can be expressed in terms of the stream function, which satisfies Stokes' equations[28]. The general solution for the stream function is available for axisymmetric flows in spherical coordinates[29]. The fixed conical shape of the interface requires the velocity in the direction normal to the interface to be zero, or $v_\theta = 0$ at $\theta = \theta_c$. Thus, on the conical interface the flow is purely radial, requiring the stream function to be independent of the radial distance, r . Upon applying this constraint, the form of the stream function at the interface becomes

$$\psi = \frac{C_1}{2}(\cos^3 \theta - \cos \theta) . \quad (4.8)$$

The relationship between the stream function and the velocity components along with Eq. (4.8) leads to a form of the velocity given by

$$v_r = \frac{C_1}{2r^2}(3\cos^2 \theta - 1) . \quad (4.9)$$

Though this form is only valid on the interface, $\theta = \theta_c$, we assume that flow on either side of the interface is predominantly radial. To avoid solving the entire flow field, the form of the velocity field given in Eq. (4.9) will be used to obtain local

gradients in velocity in the regions adjacent to the interface. This assumption of predominantly radial flow near the interface is supported by particle tracking experiments[7]. Continuity of velocity at the interface requires this result to be independent of the fluid phase. At the cone-to-thread transition point within the orifice, $r = r_c$, the outer flow is assumed to be plug flow since the length of the orifice is not sufficient to attain fully developed flow[30]. To obtain a value for the constant C_1 , the interfacial velocity is set equal to the plug flow velocity within the orifice, $v_r|_{r=r_c} = -Q_o / (w_{or}h)$. Note that v_r is less than zero, implying that flow is directed towards the cone apex. The final form of the velocity profile in the vicinity of the interface is given by

$$v_r = \frac{-Q_o}{w_{or}h} \left(\frac{r_c^2}{r^2} \right) \frac{(3 \cos^2 \theta - 1)}{(3 \cos^2 \theta_c - 1)}. \quad (4.10)$$

Once the interfacial velocity is known, the viscous stress acting on the interface can be determined. Eq. (4.4) can now be specialized using the functional form of the interfacial velocity. Since the velocity profiles are assumed to be identical near the interface on either side, the strain tensors in each liquid are also the same. The relevant tangential component of the interfacial stress balance can be obtained by taking the inner product of Eq. (4.4) and the radial unit vector to obtain

$$\frac{\partial \gamma}{\partial r} = -(\mu_o - \mu_i) \left[\mathbf{e}_r \cdot \left(\nabla \mathbf{v} + (\nabla \mathbf{v})^T \right) \cdot \mathbf{e}_\theta \right]. \quad (4.11)$$

Eq. (4.11) specifically equates the Marangoni stresses due to an interfacial gradient of surface tension to the viscous stress acting on the interface. The relevant velocity

gradients can be obtained by differentiating Eq. (9). Integrating Eq. (4.11) with respect to r yields an interfacial tension profile which must be satisfied to maintain the conical shape. To determine the integration constant, a value of the interfacial tension must be known at a point on the interface. We set the interfacial tension at $r = S$, the location where the liquid-liquid interface is pinned upstream, equal to the clean interfacial tension value, γ_0 . The resulting equation for the interfacial tension profile is given by

$$\gamma - \gamma_0 = -\frac{3(\mu_o - \mu_i)Q_o \sin \theta_c \cos \theta_c}{w_{or}h(3\cos^2 \theta_c - 1)} \left(\frac{r_c^2}{r^2}\right) \left(1 - \frac{r^2}{S^2}\right). \quad (4.12)$$

The interfacial tension profile is generated by the presence of surfactant. Using Eqs. (4.5) and (12), an implicit equation for the interfacial surfactant concentration distribution $\Gamma(r)$ along the interface can be obtained. Interfacial tension and surfactant concentration are plotted in Figure 4.3 as functions of dimensionless distance along the cone interface for typical conditions at which tipstreaming occurs experimentally. The solid line represents interfacial tension; the dashed line represents the surfactant concentration. These two profiles are related by the interfacial equation of state given in Eq. (4.5). Note that as the cone tip is approached, i.e. as $r \rightarrow 0$, the interfacial tension rapidly decreases commensurate with an increase in the concentration of surfactant. The inset schematically illustrates the convective effect of the outer elongational flow field on the interfacial surfactant concentration profile. These results are consistent with the phenomenological mechanism for tipstreaming first described by de Bruijn[31].

The interfacial concentration profile can be integrated over the surface of the cone, to obtain the moles of surfactant needed to satisfy the interfacial stress balance. For the conical geometry the surface integral is given by

$$N_{Cone} = 2\pi \int_{r_c}^S \Gamma(r) r \sin \theta_c dr . \quad (4.13)$$

For tipstreaming to occur, there must be sufficient time for an appropriate number of moles of surfactant to adsorb to the interface to generate a conical shape. To estimate the time available for adsorption, we use the characteristic time scale for thread formation, which is comparable to the time between formation of primary droplets. Lee *et al.* previously determined the characteristic time scale for droplet formation[8]. Based on scaling analyses of the characteristic lubrication[32] and Laplace pressures developed during droplet breakup along with mass conservation, the time of formation is proportional to the cube of the orifice hydraulic diameter and inversely proportional to inner phase volumetric flow rate and the capillary number, defined by

$$Ca = \frac{\mu_o a Q_o}{RT \Gamma_\infty h L} \left[\frac{1}{w_{or}} - \frac{1}{2w_{up}} \right] . \quad (4.14)$$

The resulting characteristic time between formation of primary droplets is given by

$$\tau_d \approx \frac{0.15 D_H^3}{Q_i Ca} , \quad (4.15)$$

where the numerical coefficient 0.15 has been determined empirically[8]. The numerical coefficient is independent of flow rates, droplet breakup mode and device geometry. It has been shown that much more complex behavior occurs for oil-in-water systems[33]. However, these systems, in general, do not tipstreaming

due to relatively large viscosity ratios. The sensitivity of the model to this value is limited.

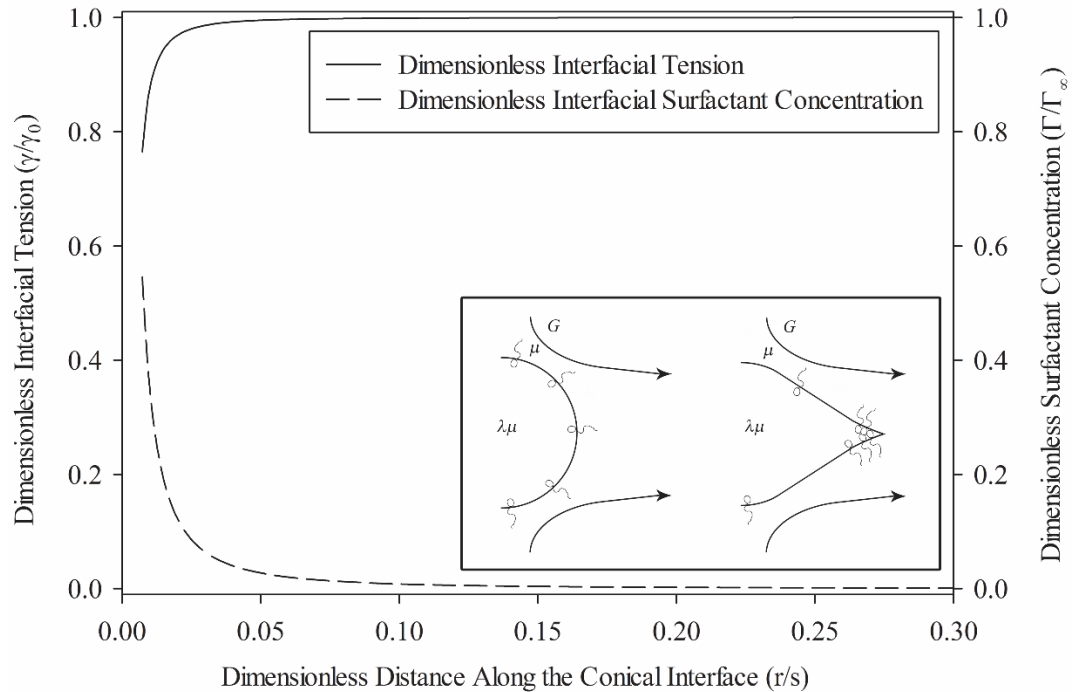


Figure 4.3. Simulated profiles for the interfacial tension and interfacial surfactant concentration along the conical interface with volumetric flow rate equal to $100 \mu\text{l}/\text{min}$ and bulk surfactant concentration equal to $7 \times 10^{-5} \text{ mol}/\text{l}$. All other parameters needed are reported in Table 3.1. The inset schematically illustrates the effect of external flow on the surfactant concentration profile. (Inset adapted from [22])

Based on the dimensional analysis previously presented, surfactant transport to the interface is kinetically limited and desorption kinetics are negligibly small compared with adsorption kinetics. We assume that at short times after formation of a primary droplet, the interface is virtually clean of surfactant and the surfactant concentration on the interface is essentially zero. In the adsorption controlled limit at short times, the generalized Frumkin rate equation yields a constant interfacial flux of surfactant to the interface of $\beta C_{\infty} \Gamma_{\infty}$. Integrating this flux with respect to time yields a linear relationship between the interfacial

surfactant concentration and time t , given by $\Gamma \approx \beta C_\infty \Gamma_\infty t$. Combined with Eq. (4.15), the number of moles of surfactant adsorbed to the interface during the time between formation of primary droplets, N_{ads} , equals the interfacial concentration evaluated at $t = \tau_d$ multiplied by an estimate of the interfacial area to yield

$$N_{ads} \approx \beta C_\infty \Gamma_\infty \tau_d (2\pi a^2) . \quad (4.16)$$

The interfacial area is estimated as half the surface area of a sphere with radius a . In reality, the interfacial shape is significantly more complicated since the protruding drop of inner phase liquid is confined by the top and bottom walls of the microchannel upstream from the cone apex. This confinement decreases the available interfacial area for adsorption. Visualization of the interface during experiments allows for an estimation of the interfacial area of the confined cone. For simplicity, the interfacial area is approximated as hemispherical which provides a reasonable estimate of the interfacial area available for adsorption compared with estimations from experiments.

The arguments presented so far suggest that tipstreaming is feasible when conditions permit sufficient adsorption of surfactant to establish a surface tension profile corresponding to a conical interface. In other words, tipstreaming is viable when $N_{Cone} = N_{ads}$ or

$$\beta C_\infty \Gamma_\infty \tau_d (2\pi a^2) = 2\pi \int_{r_c}^s \Gamma(r) r \sin \theta_c dr . \quad (4.17)$$

For given bulk surfactant concentration and liquid flow rates, Eq. (4.17) contains a single unknown quantity, the cone apex angle θ_c . The implicit, nonlinear form of

Eq. (4.17) requires θ_c to be found numerically. To reduce the number of input parameters, we express the concentration and flow rate variables in dimensionless form. A dimensionless concentration, \bar{C} , is formed by taking the ratio of the surface relaxation time scale to the kinetic time scale,

$$\bar{C} = \frac{\mu_o a \beta C_\infty}{RT\Gamma_\infty} . \quad (4.18)$$

Aside from the bulk concentration, \bar{C} is only a function of geometry, surfactant, and fluid properties. A dimensionless flow rate, \bar{Q} , is formed by taking the ratio of the primary droplet formation time to the convection time scale, yielding

$$\bar{Q} = \frac{w_{or} ha}{\tau_D Q_o} = \frac{20}{3} \left[1 - \frac{w_{or}}{2w_{up}} \right] \frac{\mu_o a^2 \varphi Q_o}{D_H^3 LRT\Gamma_\infty} . \quad (4.19)$$

Upon substitution of Eqs. (4.14) and (4.15) into Eq. (4.19) it is apparent that \bar{Q} is proportional to the inner phase volumetric flow rate, but that it is independent of the outer phase flow rate and the bulk surfactant concentration. However, in experiments we fix the value of φ and so we recast the dimensionless flow rate so that it is proportional to φQ_o . It has also been previously shown in experiments that tipstreaming is only observed when $\varphi \ll 1$ [7]. \bar{Q} also depends on geometry, surfactant, and fluid properties.

4.4 PHYSICAL LIMITS APPLIED TO THE MODEL

4.4.1 GENERALIZED FRUMKIN EQUATION OF STATE

To obtain a solution from the model equations, Matlab (The MathWorks Inc., Natick, MA) is used to numerically solve for variable values that cannot be

determined analytically. A copy of the Matlab code used is available in Appendix A of this thesis. The numerical method uses a single real variable root finding algorithm built into Matlab. Parameters in the model equations include surfactant concentration and volumetric flow rate. Thus, solutions to the model equations will vary based on the prescribed conditions. To develop solution values within a concentration/flow rate operating space, the model equations are solved at specified points within a discretized operating space. Conditions at which the solutions to the model equations are physically reasonable are considered plausible conditions for tipstreaming, allowing for the boundaries of the feasible operating diagram for tipstreaming to be determined.

For specific $\{\bar{C}, \bar{Q}\}$ pairs, Matlab is used to determine θ_c from Eq. (4.17) using numerical integration and a built in root finding algorithm (fzero, revision: 5.33.4.23)[34]. This numerical solver is applied over a discretized operating space of dimensionless flow rate and dimensionless concentration values corresponding to typical experimental conditions. Solutions to Eq. (4.17) are available for a large range of operating conditions. However, many of these solutions violate additional physical constraints. We assume that solutions that violate physical constraints represent conditions at which a conical interface cannot be maintained and a form of droplet breakup other than tipstreaming must occur, while physically viable solutions represent conditions at which tipstreaming can occur. Below, we describe four additional physical constraints that bound the tipstreaming operating space.

The first physical limit that we consider is determined by the device geometry. Figure 4.2 shows that the diameter of the section of cone residing within

the orifice increases as the cone apex angle θ_c decreases. For cone angles less than the limit

$$\theta_c < \tan^{-1} \left(\frac{a - w_{or}/2}{L} \right), \quad (4.20)$$

the cone cannot fit within the orifice region without intersecting the device walls, resulting in a lower limit for the cone angle. Solutions to Eq. (4.17) that result in a θ_c value below this limit are therefore considered to be unphysical. We note that smaller cone apex angles also correspond to larger cut off and thread radii, which would produce larger droplets than we would expect to be consistent with tipstreaming. The upper bound on θ_c is determined by the angle that produces a cut off radius of zero. However, as we will show, solutions are limited by other physical constraints before the upper bound is reached. Figure 4.4 depicts the boundary line within the dimensionless concentration vs. flow rate operating space that represents the lower limiting value of the cone angle. Boundary lines are shown for three different orifice hydraulic diameters, keeping all other geometric dimensions and material properties fixed. The region above and to the left of each boundary line corresponds to conditions that violate Eq. (4.20). The discretization resolution within the parameter space is high enough for a line to be easily determined. Decreasing the hydraulic diameter of the orifice results in a smaller physical region since only larger cone angles (smaller thread radii) are permitted. In the remainder of this paper, we use a hydraulic diameter of 60 μm to allow for comparison with experimental results.

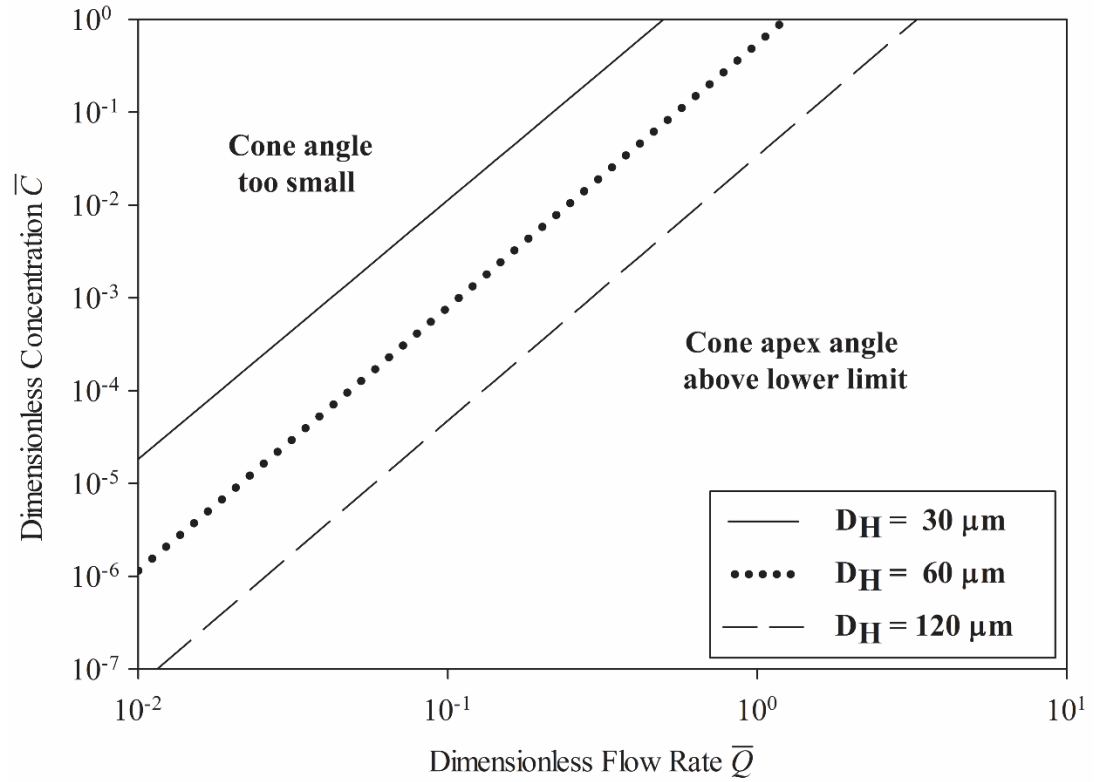


Figure 4.4. Boundary lines separating operating conditions that result in tipstreaming cone angles smaller than the lower limit, for three different hydraulic diameters of the flow focusing orifice. The region above and to the left of each line corresponds to cone apex angles below the lower limit. The remaining physicochemical properties correspond to the values listed in Table 3.1 .

Additional physical constraints can be applied to further limit the viable operating range to the right of and below the boundary lines shown in Figure 4.4. In addition to the interfacial surfactant mass balance described by Eq. (4.17), a global mass balance of surfactant must be satisfied. The rate of surfactant leaving the cone interface to populate the thread can be estimated from the model results at a given set of conditions. The molar flux of surfactant onto the thread must be less than the total molar flux of surfactant into the microchannel, or

$$Q_i C_\infty \geq 2\pi r_t (\Gamma|_{r=r_c}) (v_t|_{r=r_c}) . \quad (4.21)$$

Solutions where Eq. (4.21) is violated are considered to be unphysical. The relevant region of operating space is labeled in the lower middle region of Figure 4.5, which depicts the viable operating space for tipstreaming for the case of $D_H = 60 \mu\text{m}$ shown in Figure 4.4.

The solutions are also limited by the possible values of interfacial tension. The equation of state given by Eq. (4.5) allows the interfacial tension to attain negative values at high concentrations. However, experimentally, the minimum observed interfacial tension value is that corresponding to the critical micelle concentration (CMC) [35]. The minimum interfacial tension is well approximated by the product $RT\Gamma_\infty$ yielding the criterion

$$\gamma \geq RT\Gamma_\infty \quad (4.22)$$

as another constraint on tipstreaming. Combining Eqs. (4.12) and (4.22) and expressing the result in dimensionless form reveals that the boundary is independent of bulk and interfacial surfactant concentrations. There is an upper limit to the dimensionless flow rate, above which the interfacial tension is lower than the minimum physically reasonable value. The limiting \bar{Q} value, denoted as \bar{Q}_c^γ , depends weakly on the cone apex angle, and we take it to be approximately constant over the range of physical θ_c values. Solutions that are above \bar{Q}_c^γ , and thus violate Eq. (4.22) to satisfy the interfacial surfactant balance are considered to be unphysical; these solutions are labeled on the right side of Figure 4.5.

In addition to these physical limits, a limit can be set on which physics governs breakup. The limit of interest is the transition from tipstreaming to jetting. Experimentally, as the flow rates of a tipstreaming system are increased, the mode

of droplet breakup becomes jetting. This transition would not be captured by the limiting physical constraints applied above because during jetting, a conical interface can also be maintained. Utada *et al.* have characterized the onset of jetting in coflowing capillary devices, giving two different criteria[36]. Upon examining these criteria for jetting to occur, the relevant boundary is set as a result of the inner phase inertial forces overcoming the capillary forces. The ratio of the inertial to capillary forces can be characterized in terms of a Weber number defined by

$$\text{We} = \frac{\rho_i D_H}{\gamma|_{r=r_c}} \left(\frac{Q_o}{w_{or} h} \right)^2 \quad (4.23)$$

where ρ_i is the inner phase density. When $\text{We} \geq O(1)$ the inertial forces become large enough to overcome the surface tension and jetting occurs. The Weber number can be set to unity and rewritten in terms of the dimensionless flow rate as done with the interfacial tension limit above. This yields a critical dimensionless flow rate value, \bar{Q}_c^{We} , above which jetting is expected to occur. The critical flow rate will also weakly depend on the cone apex angle, and we again take it to be approximately constant over the range of physical θ_c values. Under the conditions given in Table 3.1, \bar{Q}_c^{We} is the smallest critical dimensionless flow rate value and thus sets the right limit on the tipstreaming region. However, it is unclear if the Weber number will always set this upper governing boundary. Solutions above this critical flow rate are determined to be jetting and are labeled on the right side of Figure 4.5.

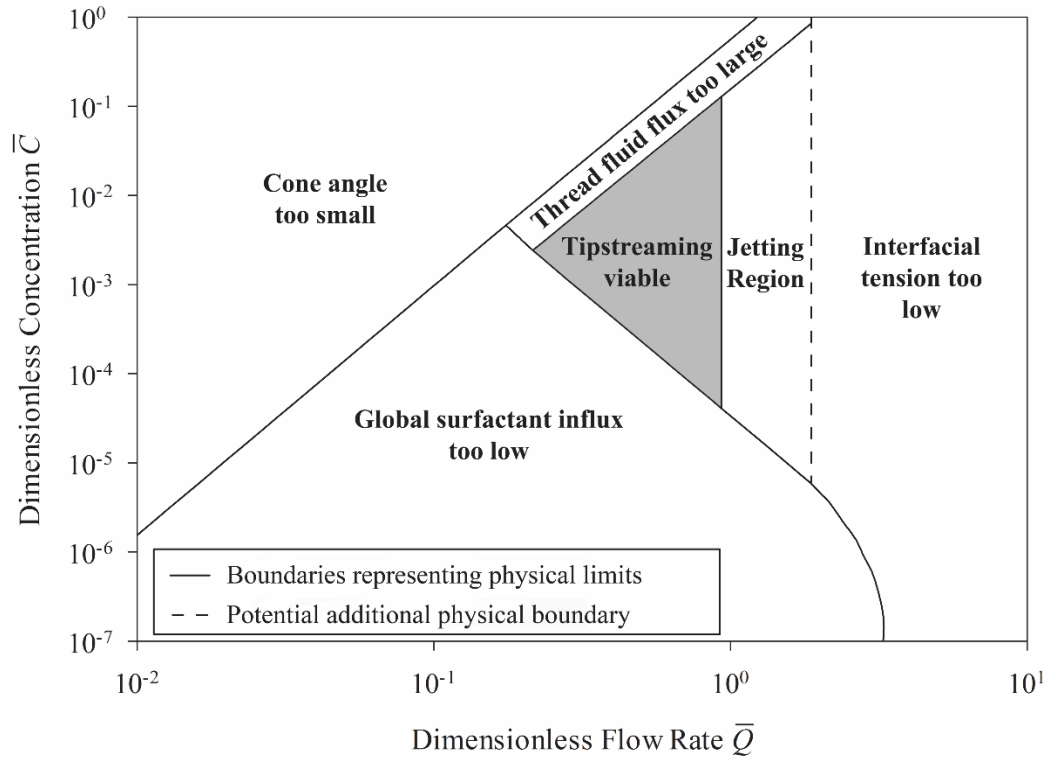


Figure 4.5. Operating diagram depicting viable conditions for tipstreaming predicted by performing an interfacial mass balance and constrained by physical limits including device geometry considerations, a global surfactant mass balance, a global fluid mass balance, transition to jetting, and a minimum interfacial tension. Physicochemical parameters used correspond to those in Table 3.1, and the $D_H = 60 \mu\text{m}$ case shown in Figure 4.4.

Lastly, the mass of the inner phase fluid must be conserved. Volumetric flow rates of the fluid in the thread can be estimated from the interfacial velocity at the cone-to-thread transition, given by Eq. (4.10). Estimating the thread velocity profile as plug flow yields Q_i values greater than the prescribed volumetric flow rate of the inner phase liquid. This result implies that pressure gradients in the cone-thread region must act to reduce the volumetric flow rate in the thread. Recirculating flow during tipstreaming has been observed experimentally, supporting the hypothesis that large adverse pressure gradients are present [7]. The

pressure change over the cone-to-thread transition can be estimated from model results, and is due to a change in interfacial curvature. It is difficult to estimate the pressure change directly but an estimate can be made using both the pressure jump across the conical interface and the thread interfaces along with an estimate of the pressure drop in the contraction flow of the outer phase flow. The pressure jump across the conical interface at the cone to thread transition is calculated from the normal component of the stress balance using parameters set by the interfacial balance. Similarly, the pressure jump across the thread interface can be estimated. The stress tensor difference for the normal component of the stress balance simplifies to the pressure difference in the two phases for a thread with constant radius. The pressure difference equals the Laplace pressure given by $\gamma|_{r_c} / r_t$ for a cylindrical thread. Lastly, the pressure drop in the outer phase flow as a result of entering the orifice can be approximated as the pressure drop due to flow through an orifice with a finite thickness[37, 38]. By combining these pressure values, the pressure gradient in the inner fluid across the cone-to-thread transition can be approximated as

$$\left(\frac{p_i^{Cone} - p_i^{Thread}}{t_{or}} \right) = \frac{\mu_o Q_o}{D_H^3} \left[\frac{128}{\pi D_H} + \frac{24}{t_{or}} + \frac{2(1-\lambda) D_H^3}{w_{or} h t_{or} r_c} \right] - \frac{\gamma|_{r_c}}{t_{or} r_c} \tan\left(\frac{\theta_c}{2}\right). \quad (4.24)$$

For small values of the cut off radius r_c , the right side of Eq. (4.24) is negative resulting in an adverse pressure gradient that drives a back flow into the cone allowing the inner phase fluid mass to be conserved. Eq. (4.24) allows calculation of the volumetric flow rate within the thread from thread boundary motion and Hagen-Poiseuille flow. The volumetric flow rate in the thread must be greater than

zero and less than the prescribed flow rate of the inner phase liquid. Solutions that lead to thread flow rates outside the physical volumetric flow rate range occupy a narrow region of phase space in the upper middle part of Figure 4.5. This boundary is much more complicated to determine and requires several more assumptions than the others.

Once all of the physical constraints described above have been considered, the remaining regions of operating space are considered feasible conditions for tipstreaming. Figure 4.5 depicts the specific range of dimensionless flow rate and dimensionless concentration values where tipstreaming is physically possible. Within this region, interfacial and bulk surfactant mass balances can be satisfied while maintaining physically reasonable interfacial tension values. The viable region is triangular in shape and spans one decade in dimensionless flow rate and five decades in dimensionless concentration.

A comparison is now be made between the experimentally observed operating range for tipstreaming and the feasible region predicted by the preceding interfacial transport arguments. The bulk concentration and flow rate values at which tipstreaming is observed are normalized to obtain corresponding \bar{C} and \bar{Q} values, and these are compared with the predicted feasibility boundaries for the same physicochemical parameters in Figure 4.6. The comparison shows that the conditions at which tipstreaming is observed in experiments lie within the physical boundaries established by the model given in Eqs. (4.17), (4.20), (4.21), (4.22), and (4.24).

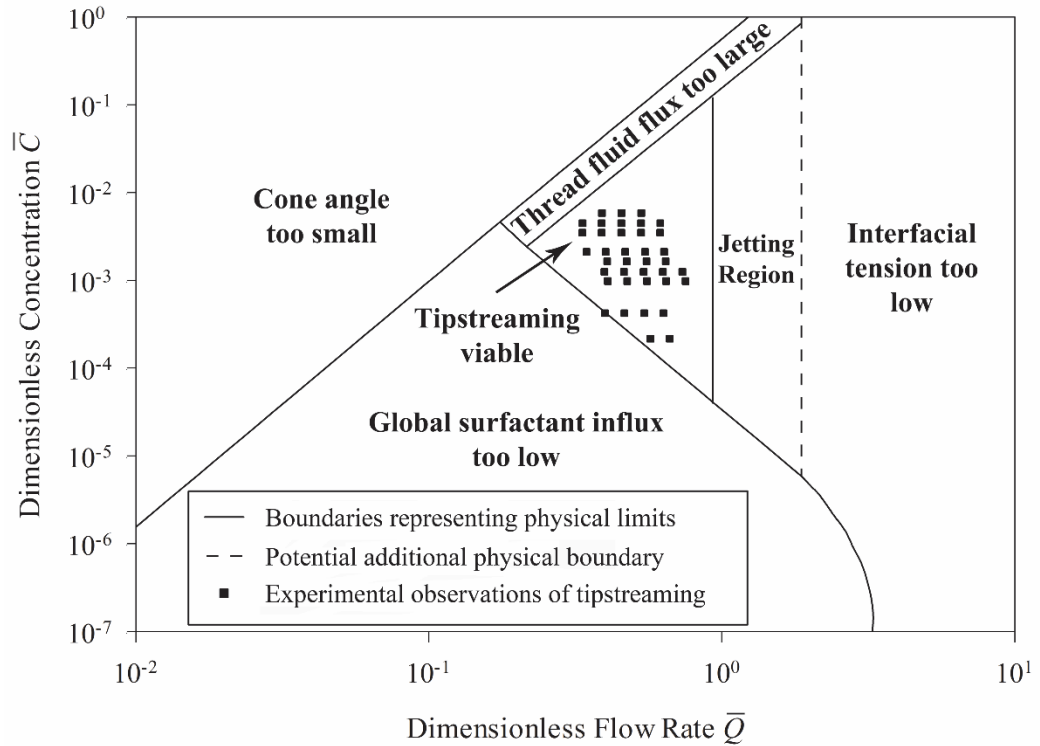


Figure 4.6. Comparison of predicted operating diagram for tipstreaming with conditions at which the tipstreaming mode of breakup is observed in experiments, shown in dimensional parameter space in Figure 4.1. Bulk concentration and flow rates are made dimensionless and defined in the text, and the predicted feasibility boundaries are estimated using the physicochemical parameters corresponding to the experiments and listed in Table 3.1 .

The results depicted in Figure 4.6 show that the simplifying assumptions used to develop the interfacial surfactant mass balance of Eq. (4.17) and the other physical constraints described in Eqs. (4.20), (4.21), (4.22), and (4.24) have led to a successful description of the conditions at which tipstreaming can occur. Although these estimates describe well the observed boundaries for one surfactant-oil-water system, there is still a need to generalize these results and validate them for other systems. The equations given here can be integrated and solved numerically using physicochemical parameters corresponding to any system of

interest. However, the nonlinear nature of these equations still does not lend insight into which parameters most strongly influence the tipstreaming process.

4.4.2 HENRY'S LAW FORMULATION

To simplify the descriptions of the feasible boundaries, we note that the upper limit of interfacial concentration estimated above lies within the linear region of the generalized Frumkin equation of state. Therefore, we can approximate the equation of state as linear, using the Henry's Law form, $\gamma \approx \gamma_0 - RT\Gamma$, allowing Eqs. (4.17), (4.20), (4.21), (4.22), and (4.24) to be evaluated analytically. Using the linear equation of state, Eq. (4.17) is integrated and the result is expressed in terms of the dimensionless flow rate, \bar{Q} and the dimensionless concentration, \bar{C} . For a fixed device geometry, surfactant type, and cone apex angle, the bulk concentration at which the interfacial mass balance is satisfied is proportional to the cube of the flow rate, $\bar{C} \propto (\bar{Q})^3$. Evaluating the proportionality coefficient at the minimum cone apex angle, given by Eq. (4.20), yields a simplified version of the upper geometric bound, given by

$$\bar{C} = \left(\frac{0.3D_H^3 L w_{up} r_c}{\varphi w_{or} h a^3 S [2w_{up} - w_{or}]} \right)^2 \left(\frac{3 \sin^2 \theta_c \cos \theta_c}{2 [3 \cos^2 \theta_c - 1]} \right) \left(S^2 \left[\ln \left(\frac{S^2}{r_c^2} \right) - 1 \right] + r_c^2 \right) \bar{Q}^3 \quad (4.25)$$

where

$$\theta_c = \tan^{-1} \left(\frac{2a - w_{or}}{2L} \right) \quad \text{and} \quad (4.26)$$

$$r_c = \frac{(2w_{or}L - 2t_{or}a + t_{or}w_{or}) \left([2a - w_{or}]^2 + 4L^2 \right)^{\frac{1}{2}}}{4L(2a - w_{or})} .$$

Figure 4.7 shows this approximate boundary as a solid line which agrees well with the numerically calculated boundary using the nonlinear equation of state (dashed line). The boundary given by Eq. (4.21) describing the global surfactant mass balance can be linearized in a similar way, and expressed in terms of the dimensionless concentration and flow rate. This approximation reveals that the minimum bulk concentration needed to produce tipstreaming is inversely proportional to the cube of the flow rate, $\bar{C} \propto (\bar{Q})^{-3}$. The proportionality coefficient depends on the cone apex angle, the device geometry, and the surfactant properties. For consistency, the proportionality coefficient is evaluated at the minimum cone apex angle, given by Eq. (4.20) and yields an analytic solution for the global surfactant limit, given by

$$\bar{C} = \left[\frac{2\pi a^2 \beta (\mu_o - \mu_i)}{w_{or} h R T \varphi} \left(\frac{3 \sin^2 \theta_c \cos \theta_c}{2 [3 \cos^2 \theta_c - 1]} \right)^{\frac{1}{2}} \right]^3 \bar{Q}^{-3}, \quad (4.27)$$

where θ_c is given by Eq. (4.26). This relationship is plotted in Figure 4.7 as a solid line, compared with the numerically calculated boundary using the nonlinear equation of state (dashed line). The arrows indicate that the linearization shifts the lower boundary to higher concentrations. The difference is attributed to the linearization of the equation of state, which leads to an overestimate of the mass of surfactant needed to satisfy the total interfacial stress balance and a corresponding increase in the bulk concentration.

Lastly, we consider the jetting onset boundary. Setting the Weber number equal to one and expressing the result in dimensionless form reveals that the boundary is independent of bulk and interfacial surfactant concentrations. Thus, a

specific equation of state does not need to be assumed. There is an upper limit to the dimensionless flow rate, above which the Weber number is greater than one. The limiting \bar{Q} value depends weakly on the cone apex angle, and we take it to be approximately constant over the range of physical θ_c values. The resulting approximate value of critical dimensionless flow rate, \bar{Q}_c^{We} , is shown in Figure 4.7 with a solid line and given by

$$\bar{Q}_c^{We} = \chi \left[\left(\left(\frac{(1-\lambda) \sin \theta_c \cos \theta_c}{(3 \cos^2 \theta_c - 1)} \right)^2 + \frac{4}{9} \text{La} \right)^{\frac{1}{2}} - \frac{(1-\lambda) \sin \theta_c \cos \theta_c}{(3 \cos^2 \theta_c - 1)} \right], \quad (4.28)$$

$$\text{where} \quad \chi = \left(\frac{10 \mu_o^2 a^2 \phi w_{or} h}{\rho_i D_H^4 L R T \Gamma_\infty} \right) \left(1 - \frac{w_{or}}{2 w_{up}} \right)$$

where θ_c is given by Eq. (4.26) and La is the Laplace number defined by $\text{La} \equiv (\rho_i D_H \gamma_0) / \mu_o^2$. The approximate boundary agrees well with the numerically computed value, given by the vertical dotted line, since an approximation for the equation of state was not needed. The three approximate boundaries lead to an approximate feasible region for tipstreaming denoted by horizontal shading in Figure 4.7. The numerically calculated feasible region using the nonlinear equation of state is denoted by diagonal shading. The cross hatch pattern indicates the overlap between the two estimates of the feasible regions; there is significant agreement between the two. The approximate boundaries given by Eqs. (4.25), (4.27), and (4.28) provide useful criteria and better insight into which parameters influence the operating range for tipstreaming most significantly.

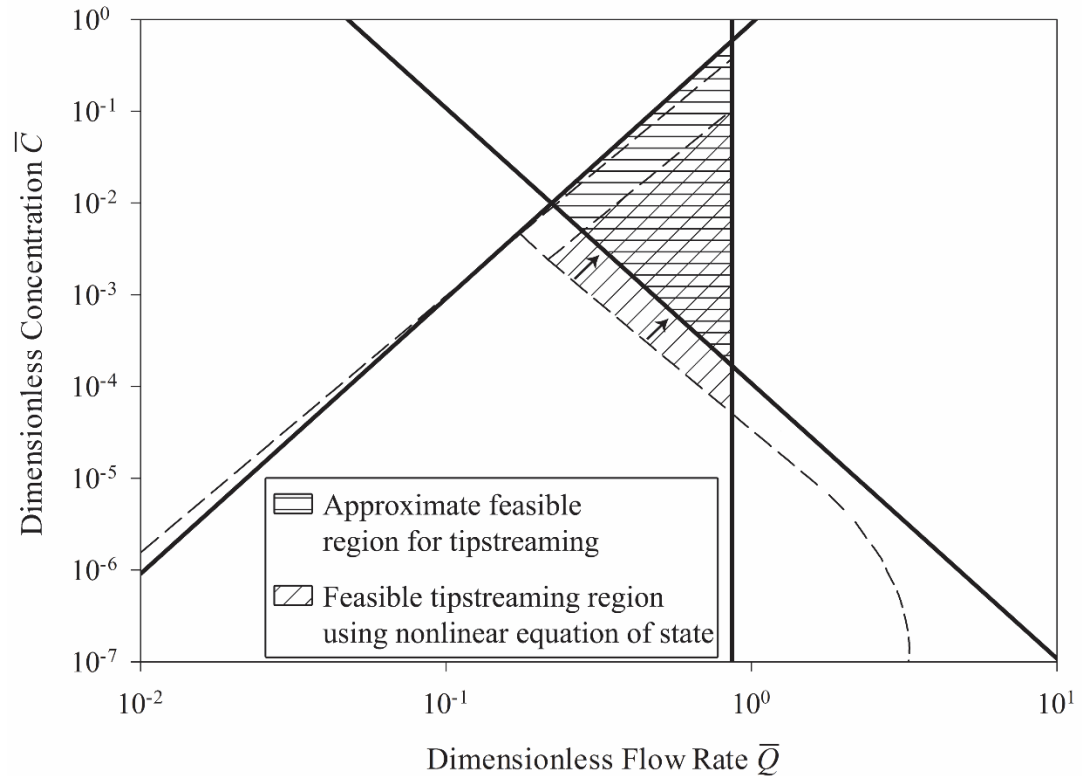


Figure 4.7. Approximate physical boundaries for the tipstreaming region obtained by linearizing the equation of state. The solid lines indicate the geometry boundary, the global surfactant mass balance boundary, and the jetting transition boundary. The dotted lines indicate the corresponding numerical model solutions using the nonlinear equation of state. The arrows indicate the directions the boundaries shift as a result of the linearization of the equation of state. The horizontal shading indicates the physical tipstreaming region predicted by the approximate boundaries. The diagonal shading indicates the feasible region predicted from the numerically calculated boundaries. The cross hatched pattern indicates overlap between these two regions.

4.5 RESULTS AND DISCUSSION

The agreement between model results and tipstreaming experiments is significant because the model does not require any arbitrary scaling of the feasibility boundaries, nor does it require any fitted parameters. All of the relevant

isotherm and equation of state parameters can be obtained via independent methods. The result is a semi-analytical model that can predict the concentrations and flow rates needed to obtain tipstreaming for a given surfactant-oil-water system and a given device geometry. The model is developed with the help of several key assumptions, meaning that there are limitations to the applicability of the results. The assumption of a conical interface is the most significant assumption made, since it allows the form of the interfacial velocity to be determined and the interfacial stress balance to be evaluated.

Tipstreaming images show that the conical assumption is appropriate for the region near the tip from which the thread is drawn. However, upstream of the cone tip, the interface is confined by the top and bottom walls of the microchannel leading to a “pancake” like interface shape in that region. Although we estimated the total surface area of the flattened cone to be similar to that of a spherical cap, we did not account for the variations in the fluid and interfacial velocities that must occur in this region. Since the most dramatic changes in interfacial velocity and interfacial tension occur very close to the tip, we assume that changes at the rear of the cone will not significantly alter the results. A second important assumption is that kinetically limited surfactant transport determines the mass of surfactant that adsorbs to the interface during thread formation. This suggests that tipstreaming is best accomplished with a surfactant that exhibits relatively slow adsorption kinetics. The model examines this specific limiting case but does not rule out the possibility for tipstreaming in other transport limits. Measuring kinetic rate constants for surfactants is difficult since many measurement methods that can

access transport timescales, including pendant drop experiments, are predominantly diffusion-limited[39] meaning kinetic and diffusion transport mechanisms cannot be decoupled[27, 40]. As a result, there is a lack of reliable surfactant kinetic rate constants available, preventing estimation of the relevant tipstreaming conditions for most surfactants, especially at oil-water interfaces. Additionally, the criteria implemented in this model specifies the conditions needed for tipstreaming and is not able to determine whether periodic or continuous thread formation occurs. Lastly, the model fails to capture any viscoelastic effects exhibited by the bulk fluids. Thread formation can occur with viscoelastic fluids [41], however the mechanism for thread formation in the presence of viscoelasticity is different from the surfactant mediated process described here. The model presented is not appropriate to analyze thread formation in non-Newtonian fluids.

A goal of developing the model presented here is to better understand how to control the tipstreaming process, for example by increasing the operating range in which it occurs. The approximate boundaries given by Eqs. (4.25), (4.27), and (4.28) facilitate rapidly estimating the effect of each parameter on the tipstreaming boundaries. Firstly, the tipstreaming boundaries are complicated functions of the device geometry. The orifice width and microchannel depth are incorporated in both the hydraulic diameter and the convective time scales. Doubling the orifice width shifts the feasible tipstreaming region to lower dimensionless flow rates and lower dimensionless concentration values. More specifically, the geometry limit shifts to lower dimensionless flow rates by a quarter of a decade, the global surfactant mass balance boundary shifts to lower dimensionless flow rates by three

quarters of a decade, and the jetting transition limit shifts to lower dimensionless flow rates by a third of a decade. The boundary movement caused by doubling the orifice width slightly decreases the size of the tipstreaming region. Increasing the microchannel depth has an opposite, but smaller, effect on the geometry and jetting transition boundaries. However, the global surfactant mass balance boundary is shifted to lower flow rates by half a decade, increasing the tipstreaming region and shifting it to lower concentration values. The geometry boundary shifts to higher dimensionless flow rates by a twentieth of a decade and the jetting transition limit shifts to higher flow rates by a fifth of a decade. These shifts still result in a larger predicted region for tipstreaming.

Doubling the orifice width and microchannel depth (such that the hydraulic diameter is doubled) results in a similar shift to that caused by doubling the orifice width alone. In this case, the global surfactant mass balance boundary shifts to lower dimensionless flow rates by three quarters of a decade, increasing the size of the tipstreaming region. The upstream capillary radius a , see Table 3.1, is also important due to its role in determining the apex angle of the interface. Doubling a alters the jetting transition boundary to a moderate extent but significantly impacts the geometry and global surfactant mass balance boundaries, which both shift to higher flow rates by a decades, eliminating the feasible region of tipstreaming entirely. Halving a has the opposite effect, doubling the size of the feasible tipstreaming region. Doubling the distance from the upstream capillary to the orifice, L , has a similar, but smaller, effect on the global surfactant mass balance boundary as halving a and vice versa, shifting them by half a decade in

both cases. Altering other geometric parameters influences the tipstreaming region to a lesser extent.

Surfactant properties play a significant role in establishing tipstreaming. The model suggests that the adsorption rate constant β and the maximum packing surface concentration Γ_∞ are the most important of these properties. Altering β has no effect on the geometry or jetting transition boundaries. Doubling β shifts the global surfactant mass balance boundary to higher dimensionless concentrations by a decade, decreasing the tipstreaming region, while halving β has the opposite effect. Therefore, slower rates of adsorption appear to facilitate tipstreaming over a wider range of conditions.

Doubling Γ_∞ does not alter the geometry or the global surfactant mass balance boundaries but does moves the jetting transition boundary to lower dimensionless flow rates by a quarter of a decade. These shifts decrease the feasible tipstreaming region by approximately 75%. Halving Γ_∞ has the opposite effect on the boundaries, effectively doubling the tipstreaming region. In reality, β and Γ_∞ are linked by the surfactant structure, so the changes described here would not occur independently. The product $\beta \Gamma_\infty$ has been shown to fall within a specific range of values for several different types of surfactants [27, 40]. In addition, Γ_∞ values are within an order of magnitude of the same value for a wide range of surfactants. We note that altering properties involved in the dimensionless operating space will shift dimensional values of flow rates and concentrations, which may lead to other practical considerations of fabrication and equipment limitations.

The analysis described above suggests that the most effective way to increase the feasible range of tipstreaming is to use a slowly adsorbing surfactant with a small β value, a large value for the maximum packing at the interface Γ_∞ , a small upstream capillary radius, a and a larger orifice hydraulic diameter. However, the upstream capillary radius a must remain larger than the hydraulic diameter to generate an extensional flow. In addition, increasing the hydraulic diameter will require larger dimensional flow rates to achieve similar convection timescales. The generalized Frumkin equation of state model was used to initially develop the model. However, Figure 4.7 shows that linearizing the equation of state allows for a reasonably accurate approximation to the tipstreaming boundaries, suggesting that the feasible region for tipstreaming does not rely heavily on the functional form of the equation of state.

Finally, to further validate the model, additional surfactant-oil-water systems (in which the properties β and Γ_∞ vary) should be tested to determine whether the boundaries for tipstreaming shift in the manner suggested by the model. However, as described above, obtaining kinetic rate constants for surfactants is difficult. Currently the only other reliable surfactant kinetic parameters at the oil-water interface that are available in the literature are for octaethylene glycol monodecyl ether ($C_{10}E_8$) and octaethylene glycol monotetradecyl ether ($C_{14}E_8$) surfactants[11]. These two surfactants have been used previously to obtain tipstreaming[14]. Scaled experimental tipstreaming conditions for $C_{10}E_8$ and $C_{14}E_8$ are nearly identical to those for $C_{12}E_8$. Additionally, the values of β and Γ_∞ for both surfactants are similar to those of $C_{12}E_8$. Thus, the model predicts a

similar tipstreaming region. Although the model and experiments agree well in these two cases, they do not provide a robust test of the model for significantly different surfactant properties.

4.6 CONCLUSIONS

We have developed a model capable of predicting concentration and flow rate values that will result in the microscale tipstreaming mode of droplet breakup in flow focusing geometries. The model is based on an assumption of a conical interfacial geometry, which is a unique feature of tipstreaming in experiments. By conducting an interfacial mass balance of surfactant, the mass of surfactant needed to maintain the interfacial shape is equated to the mass of surfactant that has time to adsorb to the interface in the presence of the strong convective flow. Physical constraints are also considered that limit the feasible region for tipstreaming, including the requirement of a global surfactant mass balance, the requirement that interfacial tension is greater than a minimum value, and the requirement of a dispersed phase fluid mass balance. Experimental observations of microscale tipstreaming lie within the predicted physical boundaries for tipstreaming. This agreement indicates that an interfacial surfactant mass balance is adequate to determine conditions needed to maintain a conical interface during tipstreaming. Further approximating the predicted boundaries by linearizing the equation of state allows for rapid estimation of the tipstreaming boundaries. The approximate boundaries also yield better insight into the role of device geometry and surfactant properties in the tipstreaming process. The results allow for more efficient design

of the device geometry and surfactant selection to maximize the range of conditions that result in microscale tipstreaming.

1. Stone, H.A., A.D. Stroock, and A. Ajdari, *Engineering flows in small devices: Microfluidics toward a lab-on-a-chip*. Annual Review of Fluid Mechanics, 2004. **36**: p. 381-411.
2. Duffy, D.C., et al., *Rapid prototyping of microfluidic systems in poly(dimethylsiloxane)*. Analytical Chemistry, 1998. **70**(23): p. 4974-4984.
3. McDonald, J.C., et al., *Fabrication of microfluidic systems in poly(dimethylsiloxane)*. Electrophoresis, 2000. **21**(1): p. 27-40.
4. Link, D.R., et al., *Geometrically mediated breakup of drops in microfluidic devices*. Physical Review Letters, 2004. **92**(5): p. 054503.
5. Squires, T.M. and S.R. Quake, *Microfluidics: Fluid physics at the nanoliter scale*. Reviews of Modern Physics, 2005. **77**(3): p. 977-1026.
6. Dollet, B., van Hoeve, W., Raven, J. P., Marmottant, P., and Versluis, M., *Role of the channel geometry on the bubble pinch-off in flow-focusing devices*. Physical Review Letters, 2008. **100**(3): p. 034504.
7. Anna, S.L. and H.C. Mayer, *Microscale tipstreaming in a microfluidic flow focusing device*. Physics of Fluids, 2006. **18**(12): p. 121512.
8. Lee, W., L.M. Walker, and S.L. Anna, *Role of geometry and fluid properties in droplet and thread formation processes in planar flow focusing*. Physics of Fluids, 2009. **21**(3).
9. Ward, T., M. Faivre, and H.A. Stone, *Drop Production and Tip-Streaming Phenomenon in a Microfluidic Flow-Focusing Device via an Interfacial Chemical Reaction*. Langmuir, 2010. **26**(12): p. 9233-9239.
10. Jeong, W.C., et al., *Controlled generation of submicron emulsion droplets via highly stable tip-streaming mode in microfluidic devices*. Lab on a Chip, 2012. **12**(8): p. 1446-1453.
11. Alvarez, N.J., Lee, W., Walker, L. M., and Anna, S. L., *The effect of alkane tail length of C(i)E(8) surfactants on transport to the silicone oil-water interface*. Journal of Colloid and Interface Science, 2011. **355**(1): p. 231-236.
12. Lin, S.Y., Lee, Y. C., Yang, M. W., Liu, H. S., *Surface equation of state of nonionic CmEn surfactants*. Langmuir, 2003. **19**(8): p. 3164-3171.
13. Frumkin, A., *The capillary curve of higher fatty acids and the constitutive equation of the surface layer*. Zeitschrift Fur Physikalische Chemie--Stoichiometrie Und Verwandtschaftslehre, 1925. **116**(5/6): p. 466-484.

14. Lee, W., *Microscale thread formation as a mechanism to generate submicron droplets*, 2010, Ph.D. thesis, Department of Chemical Engineering, Carnegie Mellon University: Pittsburgh, PA. p. 186.
15. Anna, S.L., N. Bontoux, and H.A. Stone, *Formation of dispersions using "flow focusing" in microchannels*. Applied Physics Letters, 2003. **82**(3): p. 364-366.
16. Christopher, G.F. and S.L. Anna, *Microfluidic methods for generating continuous droplet streams*. Journal of Physics D-Applied Physics, 2007. **40**(19): p. R319-R336.
17. Milliken, W.J., H.A. Stone, and L.G. Leal, *The effect of surfactant on the transient motion of newtonian drops*. Physics of Fluids A-Fluid Dynamics, 1993. **5**(1): p. 69-79.
18. Milliken, W.J. and L.G. Leal, *The Influence of Surfactant on the Deformation and Breakup of a Viscous Drop - the Effect of Surfactant Solubility*. Journal of Colloid and Interface Science, 1994. **166**(2): p. 275-285.
19. Eggleton, C.D. and K.J. Stebe, *An adsorption-desorption-controlled surfactant on a deforming droplet*. Journal of Colloid and Interface Science, 1998. **208**(1): p. 68-80.
20. Cohen, I., Brenner, M. P., Eggers, J., and Nagel, S. R., *Two fluid drop snap-off problem: Experiments and theory*. Physical Review Letters, 1999. **83**(6): p. 1147-1150.
21. Eggleton, C.D., Y.P. Pawar, and K.J. Stebe, *Insoluble surfactants on a drop in an extensional flow: a generalization of the stagnated surface limit to deforming interfaces*. Journal of Fluid Mechanics, 1999. **385**: p. 79-99.
22. Eggleton, C.D., T.M. Tsai, and K.J. Stebe, *Tip streaming from a drop in the presence of surfactants*. Physical Review Letters, 2001. **87**(4): p. 048302.
23. Rongy, L. and A. De Wit, *Steady Marangoni flow traveling with chemical fronts*. Journal of Chemical Physics, 2006. **124**(16): p. 164705.
24. Agrawal, M.L. and R.D. Neuman, *Surface-diffusion in monomolecular films. II Experiment and theory*. Journal of Colloid and Interface Science, 1988. **121**(2): p. 366-380.
25. Jin, F., N.R. Gupta, and K.J. Stebe, *The detachment of a viscous drop in a viscous solution in the presence of a soluble surfactant*. Physics of Fluids, 2006. **18**(2): p. 022103.

26. Edwards, D.A., H. Brenner, and D.T. Wasan, *Interfacial transport processes and rheology*. Butterworth-Heinemann series in chemical engineering 1991, Boston: Butterworth-Heinemann. 558 p.
27. Pan, R.N., J. Green, and C. Maldarelli, *Theory and experiment on the measurement of kinetic rate constants for surfactant exchange at an air/water interface*. Journal of Colloid and Interface Science, 1998. **205**(2): p. 213-230.
28. Happel, J. and H. Brenner, *Low Reynolds number hydrodynamics, with special applications to particulate media*. Prentice-Hall international series in the physical and chemical engineering sciences 1965, Englewood Cliffs, N.J.,: Prentice-Hall. 553 p.
29. Leal, L.G., *Laminar flow and convective transport processes : scaling principles and asymptotic analysis*. Butterworth-Heinemann series in chemical engineering 1992, Boston: Butterworth-Heinemann. 740 p.
30. Dupin, M.M., I. Halliday, and C.M. Care, *Simulation of a microfluidic flow-focusing device*. Physical Review E, 2006. **73**(5): p. 055701.
31. De Bruijn, R.A., *Tipstreaming of drops in simple shear flows*. Chemical Engineering Science, 1993. **48**(2): p. 277-284.
32. Garstecki, P., Gitlin, I., DiLuzio, W., Whitesides, G. M., Kumacheva, E., and Stone, H. A., *Formation of monodisperse bubbles in a microfluidic flow-focusing device*. Applied Physics Letters, 2004. **85**(13): p. 2649-2651.
33. Nie, Z.H., Seo, M. S., Xu, S. Q., Lewis, P. C., Mok, M., Kumacheva, E., Whitesides, G. M., Garstecki, P., Stone, H. A., *Emulsification in a microfluidic flow-focusing device: effect of the viscosities of the liquids*. Microfluidics and Nanofluidics, 2008. **5**(5): p. 585-594.
34. Beers, K.J., *Numerical methods for chemical engineering : applications in MATLAB* 2007, Cambridge, UK ; New York: Cambridge University Press. 474.
35. Berg, J.C., *An introduction to interfaces & colloids: the bridge to nanoscience* World Scientific, 2009.
36. Utada, A.S., Fernandez-Nieves, A., Stone, H. A., and Weitz, D. A., *Dripping to jetting transitions in coflowing liquid streams*. Physical Review Letters, 2007. **99**(9): p. 094502.
37. Sampson, R.A., *On Stokes's Current Flow*. Philosophical Transactions of the Royal Society, 1891(182): p. 449-518.

38. Dagan, Z., S. Weinbaum, and R. Pfeffer, *An infinite-series solution for the creeping motion through an orifice of finite length*. Journal of Fluid Mechanics, 1982. **115**(FEB): p. 505-523.
39. Alvarez, N.J., Walker, L. M., and Anna, S. L., *A Microtensiometer To Probe the Effect of Radius of Curvature on Surfactant Transport to a Spherical Interface*. Langmuir, 2010. **26**(16): p. 13310-13319.
40. Jin, F., R. Balasubramaniam, and K.J. Stebe, *Surfactant adsorption to spherical particles: The intrinsic length scale governing the shift from diffusion to kinetic-controlled mass transfer*. Journal of Adhesion, 2004. **80**(9): p. 773-796.
41. Lee, W., L.M. Walker, and S.L. Anna, *Competition Between Viscoelasticity and Surfactant Dynamics in Flow Focusing Microfluidics*. Macromolecular Materials and Engineering, 2011. **296**(3-4): p. 203-213.

CHAPTER 5**CONTROLLING THREAD FORMATION DURING TIPSTREAMING
USING AN ACTIVE FEEDBACK CONTROL LOOP****5.1 INTRODUCTION**

Tipstreaming has been experimentally studied in both isolated droplets[1-4] and within microfluidics[5-10]. The process has also been modeled numerically and analytically[10-18]. However, one issue in particular is that the formation of thin threads during steady flow tipstreaming is periodically interrupted by the formation of significantly larger primary droplets[5, 6]. Figure 5.1 a shows an image captured during steady state tipstreaming that shows the production of the larger primary droplets between thread formation. The larger primary droplets hinder the use of tipstreaming through either loss of feedstock chemicals or the need to add a downstream droplet separation process.

The goal of this Chapter is to develop a feedback control loop capable of maintaining the position of the highly curved interface tip and eliminating the production of the larger primary droplets. The control system results in the production of a continuous thread of droplets pulled from the interface as shown in Figure 5.1 b, which contains an image of tipstreaming captured during controlled thread formation. Several control systems previously implemented in microfluidics are discussed in Chapter 3. The control system presented in this study is unique in that the focus is to control the position of an interface from which droplets are forming. This concept arises from the experimental observation that during the portion of the process in which a thread is being drawn, the interface remains approximately stationary[10]. The physics that leads to a stable interface shape

during thread formation is inherent in the idea of controlling the interface. Thus, an understanding of the mechanism of tipstreaming is necessary.

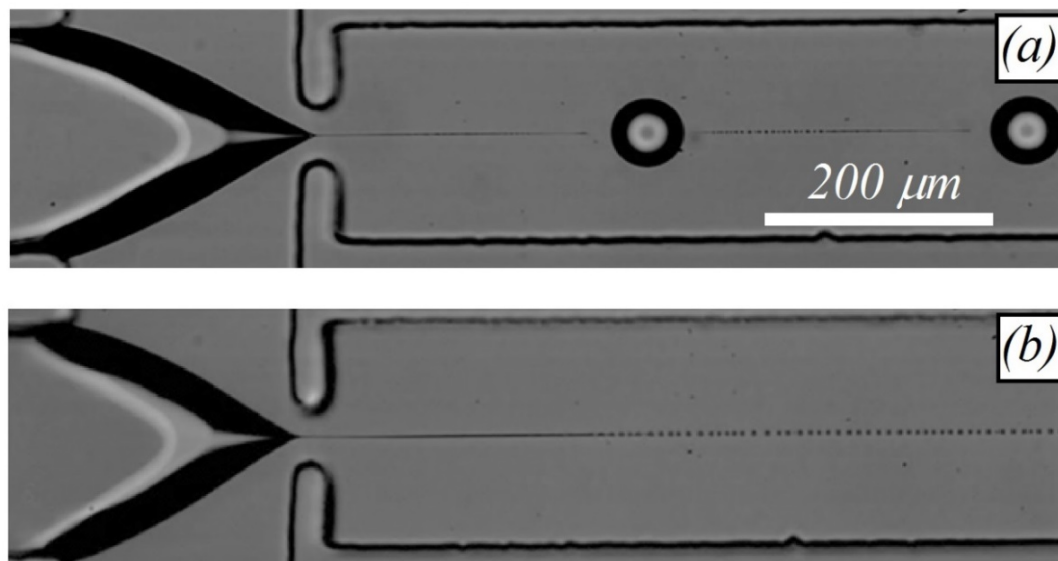


Figure 5.1 (a) Image of steady state tipstreaming using constant volumetric flow rates for both the continuous and dispersed phase fluids. (b) Image of thread formation using the active feedback controller. The set point is located 220 microns downstream of the exit of the dispersed phase channel, the proportional constant is $K_p = 9.52 \times 10^{-7}$ V/ μm , and the derivative constant is $K_d = 0$.

For isolated droplets in an unbounded elongational flow field, surfactant accumulates at the droplet poles. This results in a local decrease in interfacial tension, and a subsequent increase in curvature, leading to the distinctive tip shape. Viscous forces then draw a thread of fluid from the highly curved interface. Tipstreaming in microfluidics is performed using a flow focusing geometry shown in Figure 3.1 a. This device generates an elongational flow field as liquid is forced to flow through the contraction orifice. Within a specific range of flow rates and surfactant concentrations, tipstreaming of the dispersed phase liquid is observed. In microchannels with a uniform device height, thread formation is periodically interrupted by the production of a larger primary drop. This is likely due to both a

depletion of surfactant on the interface and an excess of dispersed phase liquid supplied to the device. Decreasing the flow rate of the dispersed phase liquid has been shown to increase the length of the thread formed[5]. However, if the flow rate is reduced too much, the interface becomes unstable and the dispersed phase liquid is forced upstream into the inlet channel. To date, a continuous thread has not been produced using an arbitrary oil-water-surfactant system. Jeong *et al.* have produced a continuous thread through a tipstreaming mechanism in a 3D channel geometry using a specific, high molecular weight surfactant[9]. However, limiting the surfactant type limits the possible applications and device fabrication for channels with varying depth requires a more complicated soft lithography fabrication technique as well as precise alignment during bonding.

Finally, the semi-analytical model for microscale tipstreaming described in Chapter 5 suggests that the position of the cone-to-thread transition within the flow focusing geometry will alter the drop size produced[10]. Thus, a control scheme based on fixing the interface tip at a specific location has the potential to allow for fine control of droplet size. Eliminating primary droplet production and enhancing the ability to control the droplet size would facilitate the use of tipstreaming in applications such as those previously listed.

5.2 CONTROLLER DEVELOPMENT AND DESIGN

Tipstreaming experiments in the present study use the planar flow focusing device geometry shown in Figure 3.1. Materials and equipment developed for the controlled thread formation experiments is described in Chapter 3 of this work.

LabVIEW is used to implement a control scheme to maintain a fixed tip location. Typically, a controller compares a measured value to a set point and alters an input variable to change the measured value. In the present experiments, the measured value is the location of the tip of the interface. The interface is imaged using an inverted microscope with an attached camera. Images captured are 304 by 304 pixels in size. To ensure consistency in measurements, the device is positioned such that the left edge of the image is flush with the exit of the dispersed phase channel. The image is then analyzed to determine the location of the tip of the interface. It is important to note that even though a high speed camera is used to obtain the images, high speed capture is not necessary. The Phantom v9.1 is used due to its availability in the current setup and the availability of manufacturer software for importing images into LabVIEW. Images are imported from the camera at a maximum frequency of 16 Hz. Once an image is captured and imported by LabVIEW, that image is analyzed using built-in image analysis tools in MATLAB (The MathWorks Inc., Natick, MA). Built-in thresholding (`im2bw`), pixel connectivity (`bwconncomp`), and edge finding (`edge`) functions are used to remove the thread and device walls from the image. Figure 5.2 illustrates the effect of these functions which allows for a rapid and robust determination of the location of the interface tip. Figure 5.2 a shows the image imported into LabVIEW from the camera using typical lighting and magnification. Figure 5.2 b is the same image after thresholding and removing all objects smaller than 7000 interconnected pixels. Figure 5.2 c shows the image after the edge finding function is applied. Once the image in Figure 5.2 c is obtained, the position of the tip can be easily

determined relative to the left edge of the image, which is flush with the exit of the dispersed phase channel.

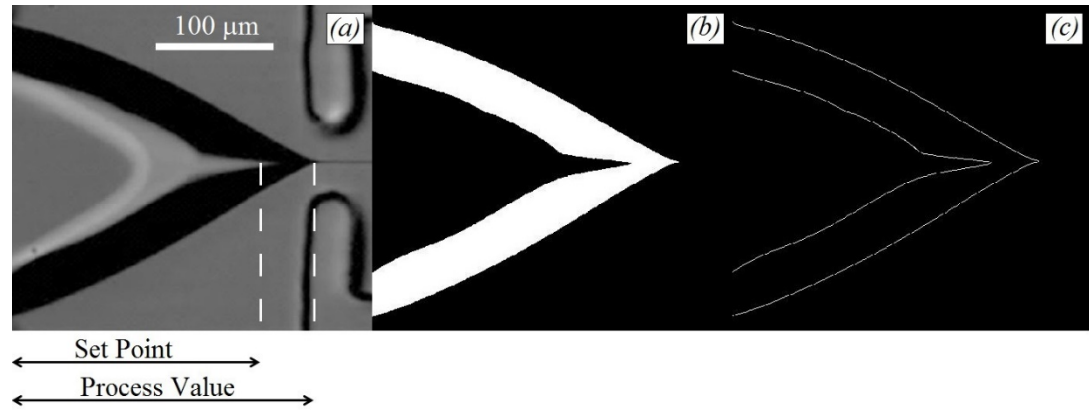


Figure 5.2 (a) Image of the interface captured during controlled tipstreaming. Both the set point and process values are measured from the left edge of the image in pixels. (b) The image shown in (a) post analysis, using built-in MATLAB commands to threshold and morphologically remove features smaller than 7000 connected pixels. (c) Image of the resulting interface after applying the built-in “edge find” command to (b) to determine the location of the tip of the interface.

The set point is defined as a fixed distance downstream of the dispersed phase channel exit. To alter the position of the interface, the voltage to the electric-to-pneumatic transducer is changed in order to adjust the pressure applied to the dispersed phase liquid, and thus the dispersed phase flow rate and the tip position. Once the initial voltage, set point, and process value are established, a simple proportional controller can be defined as

$$V_i = V_{i-1} + K_p (SP - PV) , \quad (5.1)$$

where V_i is the new voltage to be applied, V_{i-1} is the voltage applied in the previous iteration, K_p is the proportional gain constant, SP is the set point value and PV is the process value, or the measured position of the tip of the interface. In addition

to a simple proportional controller, a derivative component can also be included such that the proportional-derivative controller is defined as

$$V_i = V_{i-1} + K_p (SP - PV_i) + K_d \frac{(PV_i - PV_{i-1})}{\Delta t}, \quad (5.2)$$

where PV_i is the current process value measured, PV_{i-1} is the process value from the previous iteration of the controller, K_d is the derivative gain constant, and Δt is the time it takes to complete one iteration of the control loop. The frequency of the controller is limited by the speed at which the computer can process the images needed to complete the calculations for a loop. The processing rate varies between 12 and 16 Hz. Figure 5.3 shows a schematic representation of the feedback control loop.

In addition to the control parameters, startup conditions have the potential to affect the initial controlled behavior. To minimize startup effects, a consistent protocol is followed for all experiments considered in this study. Initially, the mineral oil containing surfactant solution is pumped through the device for 30 minutes to ensure that any swelling of the device is complete prior to droplet generation. The dispersed phase liquid tubing is then connected and an initial voltage is manually input such that a jetting or dripping mode of droplet formation is observed. Jetting and dripping modes occur at higher flow rates than tipstreaming[6, 19, 20]. For the particular setup considered here, a voltage of 2 V is supplied to the electric-to-pneumatic transducer, resulting in a reservoir vessel pressure of approximately 8 psi. The pressure is continuously applied for an additional 30 minutes to ensure that both the dispersed and continuous phase flow

rates are constant. Once the system has been allowed to reach steady state flow, the voltage applied is slowly ramped down while the process value is measured. The rate of the decrease is 1.5×10^{-4} V/s. Simultaneously, the process values for the previous 100 iterations are averaged. Once this average is within $10 \mu\text{m}$ of the set point, the ramp down is stopped and the controller is started. The time to ramp down to the point where the controller takes over varies depending on the value of the set point and initial voltage applied. For the experiments considered in this study, ramp times range from 30 minutes to one hour. Doubling the rate of decrease shows little change in the final control data suggesting the rate is small enough to prevent startup effects from influencing the controller performance.

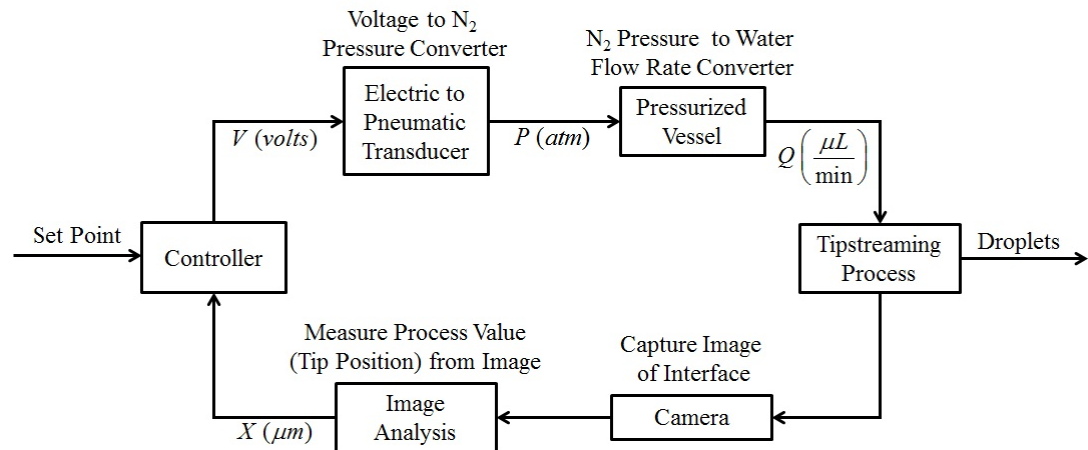


Figure 5.3 Block diagram of the tipstreaming controller. A set point and control parameter(s) are selected using a LabVIEW user interface, and the interfacial tip position from the previous iteration is recorded. The controller adjusts the voltage supplied to an electric-to-pneumatic transducer through a PCI data acquisition card. The transducer adjusts the pressure supplied to a pressurized reservoir vessel containing the dispersed phase liquid. The liquid flows into the microfluidic device, forming an interface within the flow focusing junction. The resulting interface is imaged to determine the position of the interface tip. The tip position is reported to the controller, completing an iteration of the control loop.

5.3 EXPERIMENTAL CONTROLLER OPTIMIZATION

The goal of the controller analysis is to determine the stability of the interface position during thread generation. The system is considered stable if both the production of large primary droplets is suppressed and the interface remains in the flow focusing geometry and is not forced upstream in the dispersed phase inlet channel. Stability is a function of both the controller gain constants (K_p and K_d) as well as the set point value (SP). Conditions at which tipstreaming appears most stable are used as a base case with which to analyze the effect of systematically varying each control parameter. The base case values for each parameter are $K_p = 9.52 \times 10^{-7}$ V/ μm , $K_d = 0$ (V s)/ μm , and $SP = 220$ μm , which is located 30 μm upstream of the orifice. Figure 5.4 shows the tip position as a function of time during control of the interface position. Oscillation around the set point value occurs naturally in a proportional controller. In our system, the period of the oscillations is influenced by the speed at which the microfluidic device can respond to changes in flow rate. Stone *et al.* have argued that this response is the result of the compressibility of the fluid[21]. Using their scaling analysis, the time lag for the present system is of the order of several minutes, similar to the period of oscillations observed. The ability of the controller to maintain the set point is quantified by generating a histogram of the tip positions from the transient values plotted in Figure 5.4 and calculating the standard deviation of the distribution.

Figure 5.5 shows the controlled tip position data plotted as a histogram for the base case, compared with a normal distribution having the same mean and standard deviation. The measured standard deviation of the tip position for the base

case is $\pm 5.8 \mu\text{m}$. Each standard deviation value is calculated from two hours of measured values of the tip location during controlled tipstreaming at each value of the proportional gain constant, K_p . To determine the variability of the control scheme from experiment to experiment, the base case experiment is repeated twice with identical control parameters.

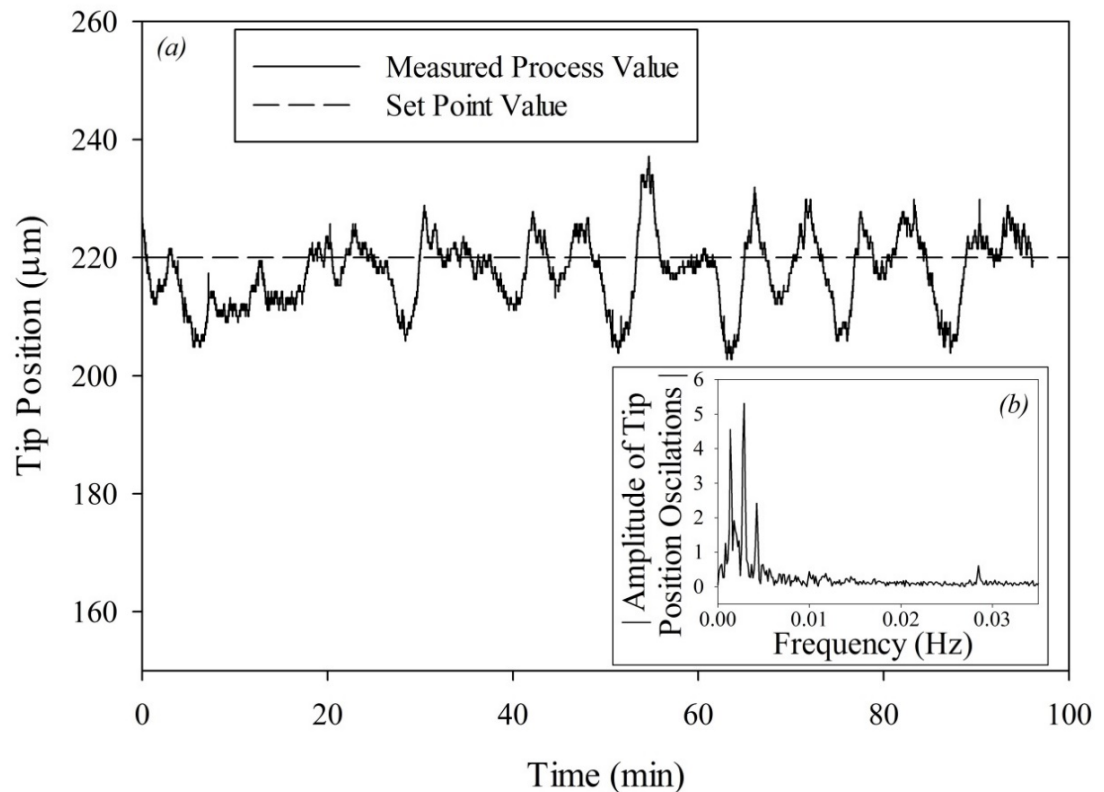


Figure 5.4 (a) Tip position as a function of time during control of the interface position for a typical experiment. The set point is located 220 microns downstream of the exit of the dispersed phase channel, the proportional constant is $K_p = 9.52 \times 10^{-7} \text{ V}/\mu\text{m}$, and the derivative constant is $K_d = 0$. (b) Sample fast Fourier Transform of the oscillation data presented in (a). The maximum peak is observed at a frequency of 0.0029 Hz corresponding to a period of 345 seconds.

The standard deviations of the two repeated runs are $\pm 5.45 \mu\text{m}$ and $\pm 5.92 \mu\text{m}$. The differences are attributed to several factors including the time at

which data collection is started and stopped, and small variations in device size. Experiments are performed to determine the optimal control parameters that result in the smallest standard deviation of the measured tip values. For these experiments, the proportional gain constant is systematically varied and the standard deviation of the process value is measured.

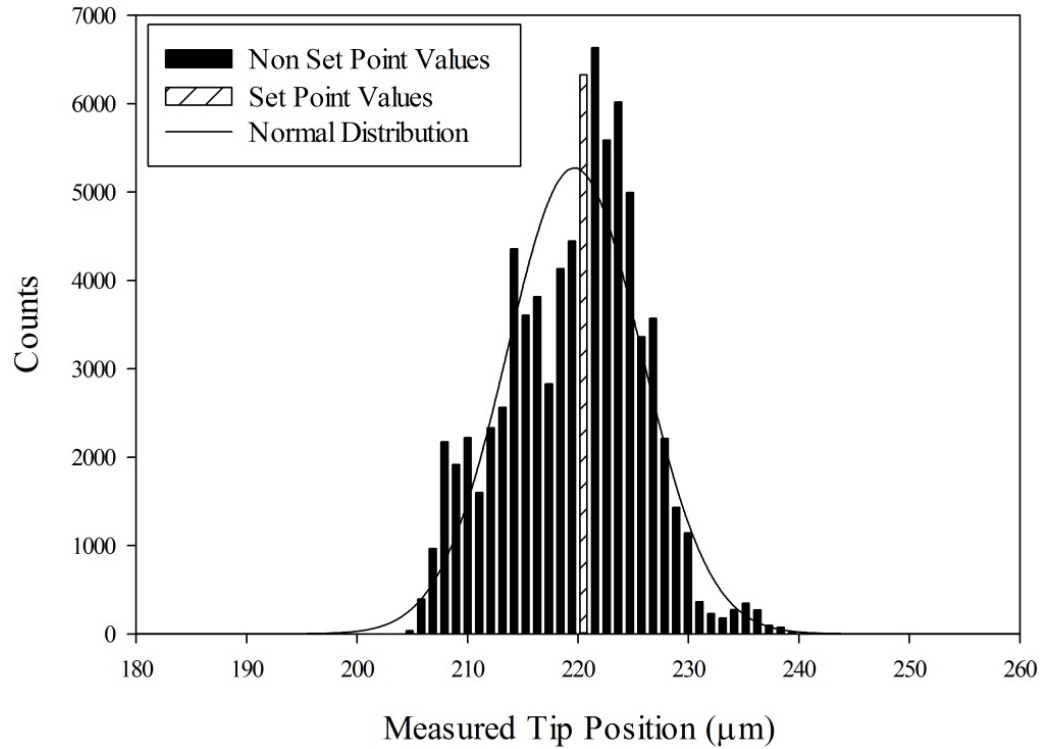


Figure 5.5 Histogram of interfacial tip location measurements obtained during control scheme operation. The set point is located 220 microns downstream from the exit of the dispersed phase channel, the proportional constant is $K_p = 9.52 \times 10^{-7} \text{ V}/\mu\text{m}$, and the derivative constant is $K_d = 0$. The normal distribution corresponds to the mean and standard deviation of the data shown.

Standard deviation of the tip position as a function of proportional gain constant is shown in Figure 5.6. Shaded regions indicate conditions where the system is unstable, exhibiting either production of larger primary droplets or flow of the dispersed phase liquid upstream into the inlet channel. By this definition, a

value of zero for the proportional gain constant also results in unstable behavior, since this effectively deactivates the controller and results in uncontrolled tipstreaming with intermittent production of large droplets. As the value of K_p is increased from zero, intermittent tipstreaming occurs until a minimum value of $K_p = 9.52 \times 10^{-9} \text{ V}/\mu\text{m}$ is reached. For gain values greater than the minimum, the system continuously produces a thread with no intermittent large droplets. At the minimum gain value, the system exhibits large oscillations in the measured tip location and thus a larger standard deviation in the position of the tip.

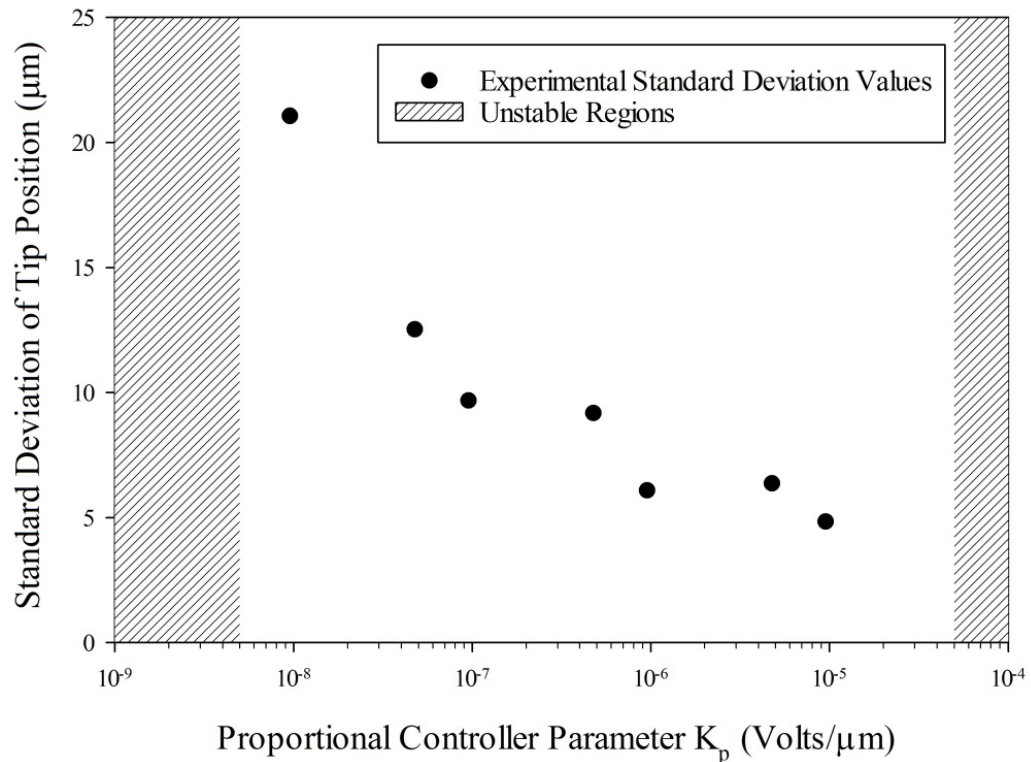


Figure 5.6 Standard deviation of the measured tip position as a function of the controller proportionality constant. Experiments using K_p values within the shaded regions result in unstable control of the interface. Unstable control of the interface results in the interface being forced upstream into the inlet channel, or the production of larger primary droplets. The set point for each experiment is located 220 microns downstream from the exit of the dispersed phase channel.

As K_p increases, the oscillations diminish until the system becomes unstable again. Increasing K_p values corresponds to a faster response by the controller, which has a stabilizing effect. However, when the proportional gain constant becomes too large, the controller responds much faster than the microfluidic device responds to changes in flow rate[21, 22]. This leads to over compensation for variations in the tip position, resulting in unstable behavior. For subsequent studies in which we examine the effects of altering the set point value and adding derivative control, the proportional gain constant is held fixed at a base case value of $K_p = 9.52 \times 10^{-7}$ V/ μm . This value is used because it exhibits comparatively small oscillations and is in the middle of the stability range observed for K_p values as shown in Figure 5.6.

In an attempt to further reduce the oscillations of the process value, a derivative component is added to the controller to test for increased stability. Using a fixed value of $K_p = 9.52 \times 10^{-7}$ V/ μm for the proportional gain constant, a derivative component is implemented using K_d values that range from $K_d = 9.52 \times 10^{-9}$ to 9.52×10^{-5} (V s)/ μm . Figure 5.7 shows the standard deviation of the tip position as a function of the derivative gain constant. The shaded region indicates values at which the system exhibits uncontrolled oscillation, resulting in the fluid interface being forced upstream into the dispersed phase inlet channel. The broken axis at small values of K_d is meant to indicate the similar effect of small K_d values to the $K_d = 0$ case. As K_d increases from zero, the system

initially shows an increase in oscillation amplitude, reflected in larger standard deviation values. For larger values of the derivative gain constant, the standard deviation decreases again until the system becomes unstable above a value of $K_d = 4.76 \times 10^{-4}$ (V s)/ μm . For all values of K_d , the standard deviation of the tip position is comparable to or larger than the base case, with no derivative control or $K_d = 0$. An integral controller component is not needed since this type of control typically addresses set point offsets, which are not observed during the tipstreaming experiments considered here.

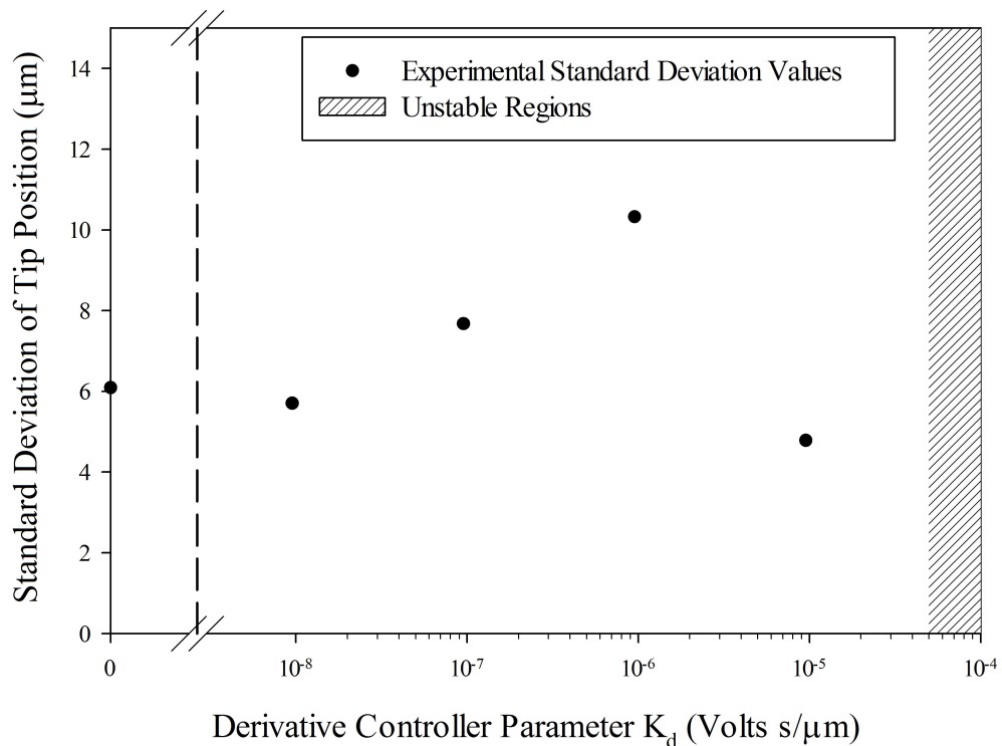


Figure 5.7 Standard deviation of the measured tip position as a function of the controller derivative constant. Experiments using K_d values within the shaded region results in unstable control of the interface. Unstable control of the interface results in the interface being forced upstream into the inlet channel, or the production of larger primary droplets. The set point for each experiment is located 220 microns downstream from the exit of the dispersed phase channel. The proportional constant is $K_p = 9.52 \times 10^{-7}$ V/ μm .

Lastly, we examine the role of the set point value on changes in oscillation amplitude and system stability. Experiments are performed using the base case value for the proportional gain constant $K_p = 9.52 \times 10^{-7}$ V/ μm with no derivative control, $K_d = 0$. The set point values are measured in microns from the exit of the dispersed phase liquid channel, located upstream of the orifice. Figure 5.8 shows the standard deviation of the measured process value as a function of the set point. Set point values between 178 and 242 μm exhibit controlled, stable tipstreaming.

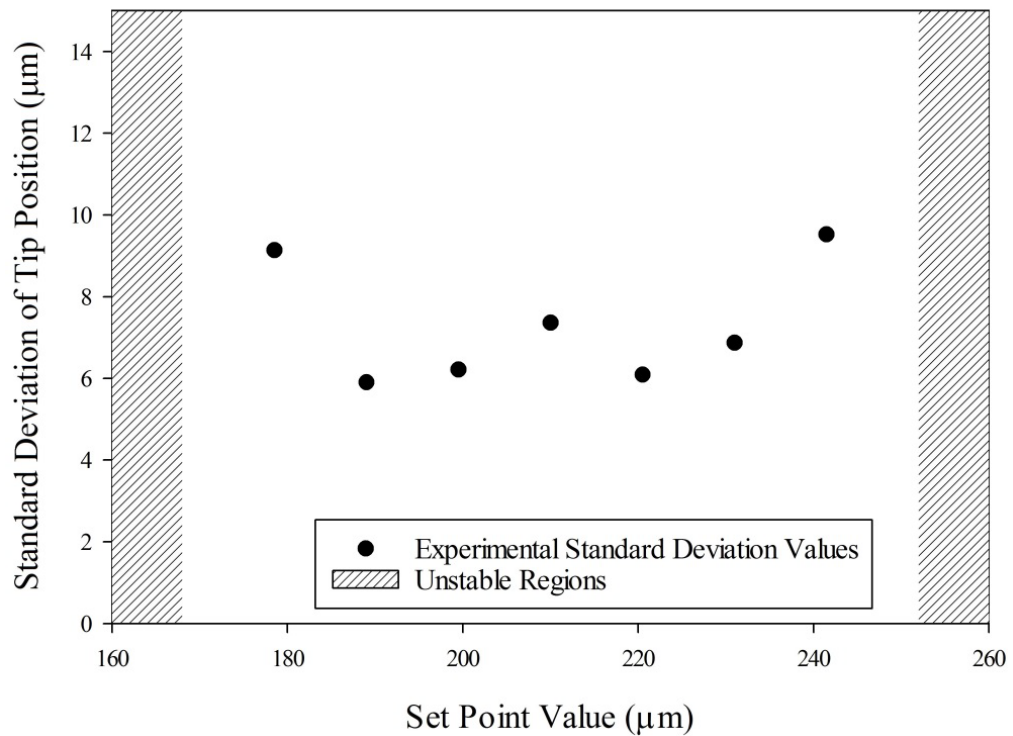


Figure 5.8 Standard deviation of the measured tip position as a function of the set point (SP). Experiments using SP values within the shaded regions result in unstable control of the interface. Unstable control of the interface results in the interface being forced upstream into the inlet channel, or the production of larger primary droplets. The proportional constant is $K_p = 9.52 \times 10^{-7}$ V/ μm . Derivative control is not used, $K_d = 0$.

At values of the set point greater than 242 μm , large primary droplets are generated, while at set point values smaller than 178 μm , the interface is forced upstream into the dispersed phase channel. Over the range of set point values that exhibit continuous tipstreaming, the oscillation amplitude, reflected in the standard deviation of the tip position, is relatively constant. There is an increase in the observed oscillation amplitude when the set point is close to the edges of the stable region. Additionally, there is an increase in the oscillation amplitude near the center of the stable set point region.

5.4 RESULTS AND DISCUSSION

The results demonstrate that a simple proportional control scheme is sufficient to maintain the position of the highly curved tip of an immiscible fluid interface while a thread is continuously drawn from it. The production of primary droplets can be eliminated, facilitating the use of tipstreaming in applications by removing the need for downstream droplet separation. Additionally, this method of continuous thread formation does not require more complicated surfactant systems or device fabrication techniques[9]. The practical limit on the length of time that controlled thread formation can be achieved is approximately 15 hours and is set by the total volume of the continuous liquid in the syringe pumps. There is a range of three control parameters, a proportional gain constant, a derivative gain constant, and a set point value, in which stable control of the thread is possible. The most critical control parameter is the proportional gain constant. The value of K_p has a significant effect on both the overall stability of the thread formation, as

well as the amplitude of the oscillations of the tip position around the set point value. In addition to analyzing the standard deviation of the measured values, a Fourier transform of the transient set point data is also performed to determine the dominant frequency of oscillation in each experiment. The Fourier transform analysis shows that there is little dependence of the dominant oscillation frequency on the values of K_p , K_d , or SP . The average value of the dominant frequency is $f = 0.0025 \pm 0.0002$ Hz over the stable region of the proportional controller. The inset of Figure 5.4 shows a sample fast Fourier transform of the data plotted in Figure 5.4.

The lowest amplitude oscillations of the tip position are obtained for values of K_p between 10^{-6} and 10^{-5} V/ μm . Oscillations in the tip position will affect the size of the resulting thread, and therefore the size of the droplets being produced. Thus, small oscillations are desirable since they are expected to translate to lower polydispersity in the resulting droplet size distribution. However, it is difficult to measure changes in the droplet size accurately due to optical resolution limits of both the microscope and camera. For this reason, determining the influence of controller gain on droplet size requires techniques other than visualization and is outside the scope of the present paper. In traditional control schemes, derivative components are added to further decrease oscillations. However, adding a derivative component to the tipstreaming controller did not show a significant decrease in oscillation amplitude, and in some situations increased the amplitude of oscillations. The derivative component implemented is a simple first order derivative controller, meaning that it only utilizes values saved

from the previous iteration. It is possible that better control could be achieved by using a higher order controller. This is indicated by the long period oscillations of the interface position compared with the high frequency of the controller[23]. Using additional iteration points may result in a more accurate representation of the slope of the measured data and a decrease in the influence of noise. Finally, the set point location will influence the average size of the droplets produced. This dependence can be deduced from a semi-analytical model[10] for tipstreaming as well as from thread size observations. Thread diameters are typically between 0.5 and 2 μm in size. An exact size cannot be determined due to optical limitations; however, altering the set point does change the visibility of the threads being produced. Larger set point values that maintain the tip farther downstream of the dispersed phase channel exit result in more clearly defined, darker threads, while smaller set point values that maintain the tip closer to the dispersed phase channel exit result in lighter threads that are more difficult to optically image. This observation suggests that the droplet size can be altered and possibly controlled by varying the set point of the controller. Further analysis of droplet size dependence on set point values is needed.

5.5 CONCLUSIONS

Results presented in this study demonstrate the ability to control the tipstreaming process and produce a continuous thread, which results in the continuous production of droplets in the 500 nm to 2 μm size range. By eliminating the production of large primary droplets inherent to steady flow tipstreaming, the

control scheme facilitates the implementation of tipstreaming in several applications that would benefit from a source of relatively monodisperse micron sized droplets. Our results show that tipstreaming can be adequately controlled using a simple proportional controller. Analysis of the influence of the control parameters on the stability of the interface location is performed to determine the optimal conditions for thread production. The addition of a derivative component to the controller does not show an increase in the stability of the interface position, and can in fact destabilize the system. Observations while using this control method also suggest that the size of the droplets generated can be controlled by altering the interface position set point. Further analysis of droplet sizes post-production are still needed to confirm this observation.

1. Taylor, G.I., *The formation of emulsions in definable fields of flow*. Proceedings of the Royal Society of London Series a-Mathematical and Physical Sciences, 1934. **146**(A858): p. 0501-0523.
2. De Bruijn, R.A., *Tipstreaming of drops in simple shear flows*. Chemical Engineering Science, 1993. **48**(2): p. 277-284.
3. Krechetnikov, R. and G.M. Homsy, *On physical mechanisms in chemical reaction-driven tip-streaming*. Physics of Fluids, 2004. **16**(7): p. 2556-2566.
4. Fernandez, J.M. and G.M. Homsy, *Chemical reaction-driven tip-streaming phenomena in a pendant drop*. Physics of Fluids, 2004. **16**(7): p. 2548-2555.
5. Anna, S.L. and H.C. Mayer, *Microscale tipstreaming in a microfluidic flow focusing device*. Physics of Fluids, 2006. **18**(12): p. 121512.
6. Lee, W., L.M. Walker, and S.L. Anna, *Role of geometry and fluid properties in droplet and thread formation processes in planar flow focusing*. Physics of Fluids, 2009. **21**(3).
7. Lee, W., L.M. Walker, and S.L. Anna, *Competition Between Viscoelasticity and Surfactant Dynamics in Flow Focusing Microfluidics*. Macromolecular Materials and Engineering, 2011. **296**(3-4): p. 203-213.
8. Ward, T., M. Faivre, and H.A. Stone, *Drop Production and Tip-Streaming Phenomenon in a Microfluidic Flow-Focusing Device via an Interfacial Chemical Reaction*. Langmuir, 2010. **26**(12): p. 9233-9239.
9. Jeong, W.C., et al., *Controlled generation of submicron emulsion droplets via highly stable tip-streaming mode in microfluidic devices*. Lab on a Chip, 2012. **12**(8): p. 1446-1453.
10. Moyle, T.M., L.M. Walker, and S.L. Anna, *Predicting conditions for microscale surfactant mediated tipstreaming*. Physics of Fluids, 2012. **24**(8): p. 082110-21.
11. Milliken, W.J., H.A. Stone, and L.G. Leal, *The effect of surfactant on the transient motion of newtonian drops*. Physics of Fluids A-Fluid Dynamics, 1993. **5**(1): p. 69-79.
12. Milliken, W.J. and L.G. Leal, *The Influence of Surfactant on the Deformation and Breakup of a Viscous Drop - the Effect of Surfactant Solubility*. Journal of Colloid and Interface Science, 1994. **166**(2): p. 275-285.

13. Eggleton, C.D., Y.P. Pawar, and K.J. Stebe, *Insoluble surfactants on a drop in an extensional flow: a generalization of the stagnated surface limit to deforming interfaces*. Journal of Fluid Mechanics, 1999. **385**: p. 79-99.
14. Eggleton, C.D. and K.J. Stebe, *An adsorption-desorption-controlled surfactant on a deforming droplet*. Journal of Colloid and Interface Science, 1998. **208**(1): p. 68-80.
15. Eggleton, C.D., T.M. Tsai, and K.J. Stebe, *Tip streaming from a drop in the presence of surfactants*. Physical Review Letters, 2001. **87**(4): p. 048302.
16. Bazhekov, I.B., P.D. Anderson, and H.E.H. Meijer, *Numerical investigation of the effect of insoluble surfactants on drop deformation and breakup in simple shear flow*. Journal of Colloid and Interface Science, 2006. **298**(1): p. 369-394.
17. Suryo, R. and O.A. Basaran, *Tip streaming from a liquid drop forming from a tube in a co-flowing outer fluid*. Physics of Fluids, 2006. **18**(8): p. 13.
18. Krechetnikov, R., *Structure of Marangoni-driven singularities*. Physics of Fluids, 2012. **24**(2): p. 022111.
19. Anna, S.L., N. Bontoux, and H.A. Stone, *Formation of dispersions using "flow focusing" in microchannels*. Applied Physics Letters, 2003. **82**(3): p. 364-366.
20. Ward, T., et al., *Microfluidic flow focusing: Drop size and scaling in pressure versus flow-rate-driven pumping*. Electrophoresis, 2005. **26**(19): p. 3716-3724.
21. Stone, H.A., A.D. Stroock, and A. Ajdari, *Engineering flows in small devices: Microfluidics toward a lab-on-a-chip*. Annual Review of Fluid Mechanics, 2004. **36**: p. 381-411.
22. Sollier, E., et al., *Rapid prototyping polymers for microfluidic devices and high pressure injections*. Lab on a Chip, 2011. **11**(22): p. 3752-3765.
23. Ang, K.H., G. Chong, and Y. Li, *PID control system analysis, design, and technology*. Ieee Transactions on Control Systems Technology, 2005. **13**(4): p. 559-576.

CHAPTER 6**REMOVAL OF PRIMARY DROPLETS GENERATED DURING TIPSTREAMING USING AN ON-CHIP SEPARATOR****6.1 INTRODUCTION**

The utility of tipstreaming is to generate monodisperse micron sized droplets. However, steady state tipstreaming generates a bimodal distribution of droplets, as shown in Figure 5.1 a. The controller developed in Chapter 5 details a method to eliminate the production of primary droplets resulting in only micron sized droplet formation. However, production rates are low for an individual microfluidic device. Generating a usable quantity of droplets from a single device requires several days. Scale up procedures for microfluidics have been suggested which use multiple device geometries in parallel[1]. It is impractical to develop and build a controller for multiple devices, requiring multiple imaging tools and flow control regulators. An alternative method of eliminating the primary droplets would be advantageous for use in parallel systems.

One method to obtain only the micron sized drops is to separate and remove the primary drops from the smaller droplets of interest. This separation can be performed on the microfluidic device or off chip after collection of the droplets. Off chip separation requires robust stabilization of droplets against coalescence. During collection of a droplet stream, there is a large decrease in fluid velocity as the fluid and drops exit the microfluidic device. The decreasing fluid velocity results in slow moving droplets within the device exit. Droplet spacing decreases such that drainage times for the oil between two consecutive droplets becomes shorter than the time needed for the droplets to move apart[2]. The bimodal

distribution in drops sizes increases this effect, causing shorter distances between subsequent droplets and increased coalescence[3].

Additionally, surfactant concentrations necessary for tipstreaming are not large enough to prevent droplet coalescence[4, 5]. Model results described in Chapter 4 show the micron sized droplets have a higher interfacial surfactant coverage. However, the high coverage of the micron sizes drops is not enough to prevent coalescence with the primary droplets which have lower coverage [6]. Off chip separation techniques, such as centrifugation or filtration, also apply a high shear stress on the droplets which results in additional coalescence and droplet breakup. Due to these issues, off chip separation is unattractive since a mechanism is needed to prevent broadening of the drop size distribution. Motivated by these complications, the work in this Chapter investigates an on chip separation technique to generate a source of only micron sized droplets from steady state tipstreaming.

If the primary droplets are removed on chip, collection of micron sized drops requires minimal additional droplet stabilization. This is due to the high interfacial surfactant coverage of the micron sized droplets. Droplet spacing also remains more uniform upon collection, decreasing coalescence. Additionally, inline separation allows for visualization of the separation process. Visualization allows for in ensuring minimal drop coalescence during separation and quantifying separation efficiency. Lastly, on chip separation limits the need for additional processing of collected droplets. Thus, designing a robust on chip droplet separation technique is useful in developing tipstreaming as more attractive droplet generation tool.

6.2 BACKGROUND

Several droplet and particle separation techniques have been utilized in microfluidic devices. Active techniques based on magnetism[7] or electrophoresis[8-10] as well as passive techniques based on trapping[11], obstructions[12], and fluid flow[6, 13, 14] have been successful. However, many of these techniques have specific physical limitations which prevent their use with tipstreaming. Active separation techniques employ an external force on the droplets to be separated. The force applied typically depends on droplet size, creating lateral displacement which allows for different sizes to be directed to different exit streams. However, tipstreaming systems require very high linear velocities. This results in short residence times of the droplets in a given section of the channel. Because of this, it is difficult to achieve a high degree of separation within a short time. Additionally, slowing the exit stream velocities by increasing the channel cross sectional area typically increases drop coalescence.

Passive techniques provide a more promising method of separation. Many of these techniques, including filtration and obstacle based separation, rely on hydrodynamic interactions. Generally, these techniques use the size of openings or channels to prevent larger droplets from entering. These systems work well for droplets with low Weber and capillary numbers[11, 15]. In these cases, surface tension is dominant and droplets maintain a spherical shape. However, conditions within the tipstreaming exit channel are such that inertia and viscous forces readily deform a droplet.

The difficulty in separating droplets generated via tipstreaming is that all drops are moving on the same streamline. One technique using a pinched flow device geometry to alter the droplet streamline has been studied[6, 16]. A constriction in the exit channel along with an additional fluid inlet forces the droplets against a microfluidic channel wall. The wall is used as an obstacle but does not significantly deform the drops. Droplet streamlines are altered based on the distance the center of mass of a drop is away from the wall. Larger droplets travel on streamlines slightly further from the wall surface since their center of mass remains further from the wall than that of the smaller droplets. A subsequent expansion in the channel amplifies the difference in streamlines resulting in lateral separation of the droplets based on size.

The implementation of this type of separator in conjunction with tipstreaming has had some success at specific operating conditions. However, there are several complications that arise as a result of its use. First, the addition of the geometry onto the exit channel has a negative impact on the tipstreaming process. This is likely due to an effect of the pressure drop across the device. The restriction in the channel requires a higher input pressure which may affect upstream geometries or pump flow rates. Secondly, breakup of primary droplets within the constriction geometry largely limits the effectiveness of the separation at relevant tipstreaming conditions.

6.3 MATERIALS AND SEPARATOR DESIGN

We examine an alternative separation geometry which takes advantage of principles used in both the obstacle and pinched flow techniques. The new microfluidic separation geometry is shown in Figure 6.1 a. Separation experiments are performed using conditions similar to those described in Chapter 3 for steady state tipstreaming. A flow focusing geometry identical to that shown in Figure 3.1 is used to generate tipstreaming droplet breakup. The separation geometry is located 6 mm downstream of the flow focusing orifice. Deionized water is the dispersed phase liquid for all separation experiments. The continuous phase liquid is light mineral oil (Fisher Scientific O1211). The $C_{12}E_8$ surfactant concentration in the dispersed phase and the flow rate ratio of the two phases are kept constant at $100 \mu\text{mol/l}$ and $\varphi = 1/40$ respectively. Three different values of the continuous phase volumetric flow rate are tested to characterize separator performance.

The design concept is based on a separation technique used for macro scale droplets[15]. The pillars are in place to deflect the center of mass of the larger droplets while the smaller droplets can pass between pillar gaps. However, without the proper resistance tuning the droplets simply deform and pass through the small gaps between pillars. Resistance tuning is used to focus the streamline the drops are traveling on. First, the length of the two exit channel are carefully selected when making the microfluidic device. The secondary exit channel is designed to be approximately three millimeters shorter than the main exit channels. This initially causes the stream of both droplets to flow entirely down the secondary exit channel.

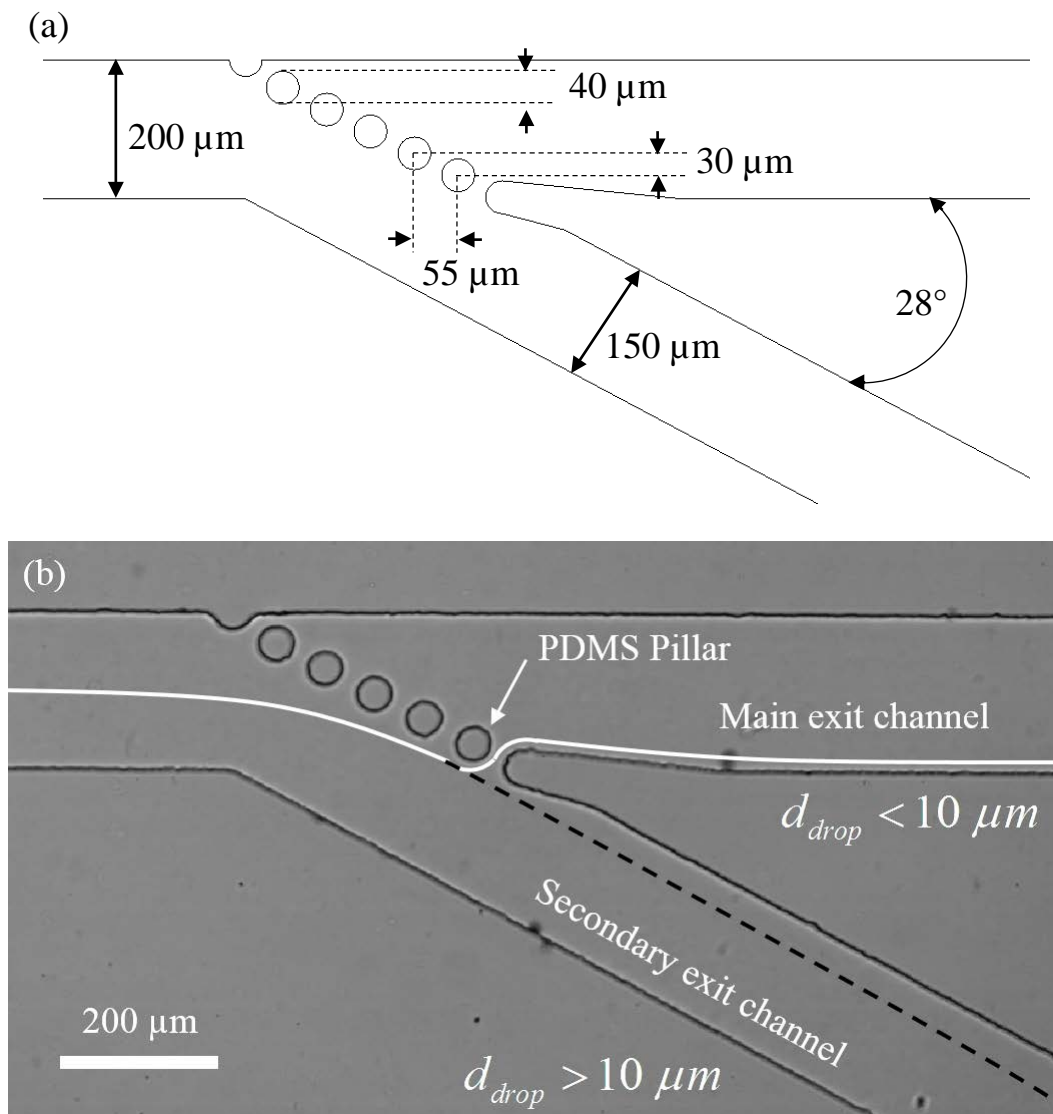


Figure 6.1 (a) A schematic representation of the separator design including device dimensions. (b) Image of microfluidic separator geometry with illustrations representing the stream lines of the droplets. Fluid flows is from left to right. Both micron sized and primary droplets enter the geometry on the white streamline on the left. Deflection of the larger droplets onto the black dashed streamline results in droplet separation as the micron sized droplets remain on the white stream line.

At both exits of the chip, polyethylene tubes are connected to the device which the liquid and droplets flow into. The polyethylene tubing (Scientific Commodities Inc.) has an inner diameter of $0.76\ \text{mm}$. The resistance to flow in the

secondary channel is increased by tightening a flow restrictor clamp placed on the polyethylene tube connected to the secondary exit channel. The restrictor clamp uses a screw drive with a screw size of 0.15 inches in diameter and 35 threads per inch. Systematic adjustments of the restrictor clamp are performed to obtain separation. Manual tightening is done in increments of a quarter turn of the screw drive. Tightening the restrictor screw produces immediate changes to the flow field based on visual observations. However, an additional 30 minutes is given after the final adjustment to ensure the flow is stabilized. The increase in resistance redirects additional fluid flow through the main exit channel, adjusting the fluid streamlines.

The goal is to manipulate the streamline on which the droplets are traveling to move close to the bottom most PDMS pillar. The larger primary droplets are deflected from the original streamline because the spacing between the original streamline and pillar is smaller than the primary drop radius. The original streamline continues into the main exit channel while the new streamline for the larger droplets travels down the secondary exit channel. The smaller sized droplets are not deflected from the original streamline resulting in separation. The original streamline is illustrated in white in Figure 6.1 b. Interactions between the pillar and the primary droplets cause the larger drops to move to a lower streamline, illustrated by the black dashed line, which flows into the secondary exit channel.

The Stokes number is used to characterize how easily particles or droplets are deflected from streamlines[17]. The Stokes number is a ratio of the momentum response time of the droplet and the characteristic time of flow around an object and is defined as

$$Stk = \frac{t_p U}{D_o} \quad (6.1)$$

where t_p is the momentum response time of the drop, U is the fluid velocity, and D_o is the diameter of the obstacle[18]. At small Reynolds numbers, as is the current case, the momentum response time of the drop is defined as

$$t_p = \frac{\rho_d D_d^2}{18\mu_o} \quad (6.2)$$

where ρ_d is the droplet density, D_d is the drop diameter and μ_o is the continuous phase viscosity[17]. Assuming the velocity of the smaller droplets is identical to the fluid velocity results in the large droplets still having a small Stokes number of $Stk = O(10^{-2})$. However, the Stokes number of the micron sized droplets is smaller by 4 orders of magnitude, $Stk = O(10^{-6})$. The difference is significant enough to result in droplet separation.

6.4 SEPARATOR RESULTS AND ANALYSIS

PDMS pillar obstacles are used to deflect the primary droplets onto slightly different streamlines. The separator geometry amplifies the distance between those streamlines similar to pinched flow separation. This technique requires focusing the streamlines such that after deflection, the two different streamlines flow into the two different exit channels. With resistance tuning, droplets traveling on the original streamline focused near the exit channel split, resulting in size based separation. An image of the separation of droplets is shown in Figure 6.2. Once

satisfactory separation is achieved, additional resistance adjustments are unnecessary and good separation is maintained for several hours.

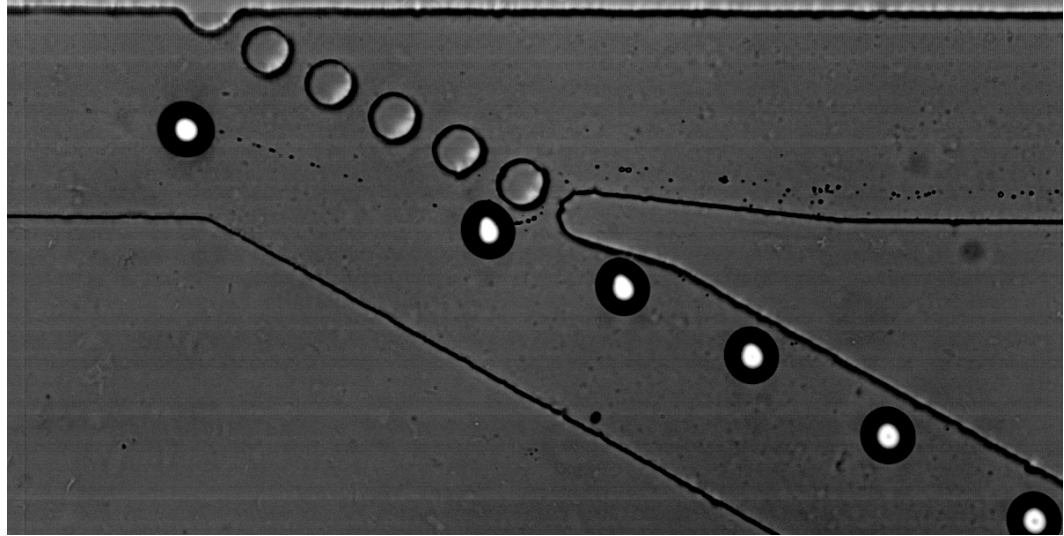


Figure 6.2 Image of successful droplets separation. Larger primary droplets are deflected by the pillar obstacles into the secondary exit channel. The movement of the smaller droplets remain unaffected, traveling into the main exit channel.

The large droplets interact with the PDMS pillar which pushes the drop to a new streamline in a similar way the channel wall does in the pinched flow separation design. However, the flow field the droplets experience in this geometry imposes less shear on the drops which eliminates primary droplet breakup. Additionally, the pressure drop across the separator is small compared with that of the flow pinching design. Any change in the total pressure drop across the device negligibly effect the thread formation process. The additional pillars above the deflecting pillar aid in balancing the flow resistance of the two channels.

Separation experiments have been performed at several different flow rate values to determine the effectiveness and robustness of the separation technique. The continuous phase flow rate values for which tipstreaming is observed range

from 60 to 120 $\mu\text{l}/\text{min}$, see Figure 4.1. Separation experiments are tested at three flow rate magnitudes, 60 $\mu\text{l}/\text{min}$, 90 $\mu\text{l}/\text{min}$, and 120 $\mu\text{l}/\text{min}$ to determine the impact on droplet separation. Here we report an efficiency percentage representing the percent of micron sized droplets captured by the main exit channel. High speed videos of the separation process are taken using methods described in Chapter 3.

For each flow rate, the separation of 100 threads from their corresponding primary droplets is analyzed. With proper resistance tuning, the larger droplets are completely eliminated from the main stream for all three flow rates tested. The number of micron sized droplets exiting within each channel is manually counted. Separation efficiencies are reported in Table 6.1 for each of the three flow rate conditions. An important note is resistance tuning requires more precise manipulation at the larger flow rate value. More precise methods of adjusting the resistance to flow in each channel including computer controlled resistance tuning would likely increase the separation efficiency.

Table 6.1 Separation efficiencies for each of the three flow rates tested. Percentages represent the percent of micron sized droplets which exited through the main exit channel.

Continuous Phase Flow Rate	Separation Efficiency
$Q_c = 60 \mu\text{l}/\text{min}$	94.8%
$Q_c = 90 \mu\text{l}/\text{min}$	92.3%
$Q_c = 120 \mu\text{l}/\text{min}$	80.6%

From visual analysis, droplets formed from the end of the threads are more difficult to separate from the primary droplet stream. This is a result of droplet-droplets interactions between thread ends and the subsequent primary droplet. At

higher flow rate values, threads generated via tipstreaming are shorter. The increased frequency of thread end drops interacting with primary droplets causes a decrease in separation efficiency. These observations indicate the generation of longer threads results in an increase in separation efficiency. Thus, the results reported by Lee *et al.* which investigate tipstreaming thread length give insight into how relatively effective this separation technique would be under different tipstreaming conditions[19].

6.5 CONCLUSIONS

This Chapter describes the development and implementation of a novel inline microfluidic separator. The result is a technique able to remove the larger primary droplets generated during steady state tipstreaming from the micron sized droplets of interest. With proper manual tuning, the separator completely removes the larger primary droplets from the stream of micron sized droplets. Analysis of separation efficiency shows the ability to separate over 90% of the micron sized droplets from the primary droplets at lower flow rates.

Increasing the flow rate magnitude has a negative impact on the separation efficiency. This is due to shorter thread lengths produced at high flow rate values. The shorter thread lengths increase interactions between the micron sized drops and primary droplets leading to decreased separation efficiency. Better control over the resistance to flow in the exit channels has the potential to increase the separation efficiency. The proposed droplet separation technique facilitates parallelization of

devices to increase micron size droplet production rates and reduces the need for off chip processing.

1. Li, W., et al., *Simultaneous generation of droplets with different dimensions in parallel integrated microfluidic droplet generators*. *Soft Matter*, 2008. **4**(2): p. 258-262.
2. Tan, Y.-C., Y. Ho, and A. Lee, *Droplet coalescence by geometrically mediated flow in microfluidic channels*. *Microfluidics and Nanofluidics*, 2007. **3**(4): p. 495-499.
3. Hung, L.-H., et al., *Alternating droplet generation and controlled dynamic droplet fusion in microfluidic device for CdS nanoparticle synthesis*. *Lab on a Chip*, 2006. **6**(2): p. 174-178.
4. Baret, J.-C., *Surfactants in droplet-based microfluidics*. *Lab on a Chip*, 2012. **12**(3): p. 422-433.
5. Anna, S.L. and H.C. Mayer, *Microscale tipstreaming in a microfluidic flow focusing device*. *Physics of Fluids*, 2006. **18**(12): p. 121512.
6. Lee, W., *Microscale thread formation as a mechanism to generate submicron droplets*, 2010, Ph.D. thesis, Department of Chemical Engineering, Carnegie Mellon University: Pittsburgh, PA. p. 186.
7. Yizhong, W., Z. Yuejun, and C. Sung Kwon, *Efficient in-droplet separation of magnetic particles for digital microfluidics*. *Journal of Micromechanics and Microengineering*, 2007. **17**(10): p. 2148.
8. Fair, R.B., *Digital microfluidics: is a true lab-on-a-chip possible?* *Microfluidics and Nanofluidics*, 2007. **3**(3): p. 245-281.
9. Gascoyne, P.R.C. and J. Vykoukal, *Particle separation by dielectrophoresis*. *Electrophoresis*, 2002. **23**(13): p. 1973-1983.
10. Pamme, N., *Continuous flow separations in microfluidic devices*. *Lab on a Chip*, 2007. **7**(12): p. 1644-1659.
11. Tan, Y.-C. and A.P. Lee, *Microfluidic separation of satellite droplets as the basis of a monodispersed micron and submicron emulsification system*. *Lab on a Chip*, 2005. **5**(10): p. 1178-1183.
12. Joensson, H.N., M. Uhlen, and H.A. Svahn, *Droplet size based separation by deterministic lateral displacement-separating droplets by cell-induced shrinking*. *Lab on a Chip*, 2011. **11**(7): p. 1305-1310.
13. Gossett, D.R. and D.D. Carlo, *Particle Focusing Mechanisms in Curving Confined Flows*. *Analytical Chemistry*, 2009. **81**(20): p. 8459-8465.

14. Choi, S., et al., *Hydrophoretic Sorting of Micrometer and Submicrometer Particles Using Anisotropic Microfluidic Obstacles*. Analytical Chemistry, 2008. **81**(1): p. 50-55.
15. Bowman, T., J. Frechette, and G. Drazer, *Force driven separation of drops by deterministic lateral displacement*. Lab on a Chip, 2012. **12**(16): p. 2903-2908.
16. Maenaka, H., et al., *Continuous and Size-Dependent Sorting of Emulsion Droplets Using Hydrodynamics in Pinched Microchannels*. Langmuir, 2008. **24**(8): p. 4405-4410.
17. Crowe, C.T., *Multiphase flows with droplets and particles*. 2nd ed2012, Boca Raton: CRC Press. xv, 494 p.
18. Fuchs, N.A., et al., *The mechanics of aerosols*. Rev. ed. ed1964, Oxford: Pergamon.
19. Lee, W., L.M. Walker, and S.L. Anna, *Role of geometry and fluid properties in droplet and thread formation processes in planar flow focusing*. Physics of Fluids, 2009. **21**(3).

CHAPTER 7**TIPSTREAMING FROM THE REAR OF A DROPLET TRAVELING THROUGH A MICROCHANNEL****7.1 INTRODUCTION**

Tipstreaming occurs due to a balance between viscous forces and surfactant effects at a liquid-liquid interface. The forces needed to observe tipstreaming can be generated in many different systems and flow fields depending on the properties of the fluids and surfactants. As a result, multiple tipstreaming systems have been studied using different geometries[1-4], fluids[5, 6], and surfactants[7-9]. Chapter 2 of this work describes several of these studies in much greater detail.

In this Chapter, we report an additional tipstreaming system not previously reported in the literature. Tipstreaming is observed at the rear of a drop traveling through a microchannel. Bubbles and droplets in microchannels travel at different speeds depending on size and the liquid viscosities[10-12]. Tipstreaming is observed at the rear of droplets traveling faster than the average fluid velocity in a microchannel. From the reference frame of the droplet, fluid is flowing past the front of the droplet towards the rear. Droplets traveling faster than the average fluid velocity generate viscous stresses on the drop interface. Chapter 4 describes similar viscous stresses at an interface as a result of fluid flow. When surfactant is present on the interface, the flow sweeps surfactant to the droplet rear, generating Marangoni stresses. Large viscous stresses are able to develop the necessary interfacial tension gradients to form a pointed tip from which a thread is pulled. The result is tipstreaming at the rear of a droplet traveling in a microchannel.

Viscous forces due to fluid flow effect droplet shape and the presence of a drop alters the fluid flow. The coupled hydrodynamics has been studied both experimentally and numerically[13-15]. In many cases, effects of confinement play a large role in the viscous stresses acting on a droplet[16]. The effects of flow on the breakup of droplets in confined channels has also been previously characterized. Olbricht and Kung found at high viscosity ratios droplet breakup occurred above a critical capillary number[17]. In their work, breakup modes did not resemble tipstreaming since surfactant was not present.

Additionally, Mulligan and Rothstein observed the formation of tails at the rear of droplets traveling in a microfluidic hyperbolic constriction[18]. As a droplet entered the constriction, several tails were observed to form and break off from the rear of the primary droplet. Significant confinement, wall effects, and a low viscosity ratio make it difficult to characterize the breakup observed as tipstreaming. However, differing degrees of drop confinement was shown to effect conditions of droplet breakup. In this work and others, the existence of a critical capillary number is used to characterize droplet breakup [19-22]. The presence of surfactant in these systems also contributes to changes in the droplet shape and fluid flow. Janssen and Anderson have numerically investigated the effect flow has on the shape and interfacial surfactant distribution of a confined droplet[23]. Their findings show increased interfacial surfactant concentrations at the rear of a droplet traveling in a confined geometry under pressure driven flow. Simulations depicting the formation of interfacial surfactant concentration gradients due to viscous stresses suggest conditions exist where tipstreaming could occur.

This Chapter specifically examines the effect of accelerating a surfactant covered drop traveling in a microchannel. During and after formation, surfactant adsorbs to the droplet interface. The droplet speed is increased downstream using additional microchannels to supply extra continuous phase liquid. The increased volumetric flowrate increases the average fluid velocity in the exit channel. In these experiments, tuning the viscous stresses on the interface can be achieved by changing the total volumetric flow rate. A balance between viscous and Marangoni stresses can be found which allows for thread formation at the rear of a droplet. Investigating tipstreaming at the rear of the droplet provides insight into the different flow fields and conditions needed to generate fluid threads from an interface. Additionally, tipstreaming from the rear of a droplet can increase micron sized drop production rates by generating multiple threads from multiple droplets in a single device.

7.2 EXPERIMENTAL METHODS AND DEVICE DESIGN

Tipstreaming is observed to occur at the rear of a large droplet traveling within a microchannel. A flow focusing geometry identical to that of Figure 3.1 is used to generate large droplets of water in mineral oil. Droplets are generated using a continuous phase flow rate of $Q_c = 20 \mu\text{L}/\text{min}$ and a dispersed phase flow rate of $Q_d = 5 \mu\text{L}/\text{min}$. These flow rates remain fixed for all experiments described within this Chapter. Experiments are performed using a range of C_{12}E_8 surfactant concentrations similar to those needed to observe tipstreaming in a flow focusing geometry. The operating conditions do not result in tipstreaming within the flow

focusing geometry. These conditions instead produce large geometry controlled droplets shown in Figure 7.1. The droplets have a diameter of approximately $150\ \mu\text{m}$ and travel in a channel with dimensions $200\ \mu\text{m}$ by $120\ \mu\text{m}$. The dimensions are such that droplets are confined by the channel in only the height direction.

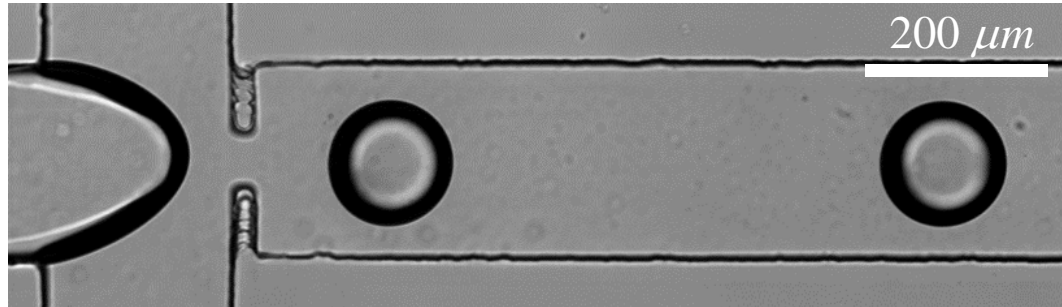


Figure 7.1 Image of geometry controlled droplet production in a flow focusing geometry. Droplet diameters are $150\ \mu\text{m}$ and channel width is $200\ \mu\text{m}$.

There are two sections of the exit channel. A diagram of the geometry is shown in Figure 7.2. The first channel section which immediately follows the flow focusing geometry is referred to as the upstream section. At the end of the upstream section, two additional channels merge with the exit channel. This is the acceleration point. Additional continuous phase liquid is supplied through these channels at varying flow rates, reported as the additional continuous phase flow rate, Q_a . The cross sectional area of the exit channel before and after the acceleration point is designed to be identical. The addition of continuous phase fluid causes the average velocity within the channel to increase at this point. The second section of the exit channel following the acceleration point is referred to as the downstream section.

The droplets traveling in the upstream section have a linear speed of approximately 20 mm/s . The capillary number characterizes the ratio of viscous stresses acting on the interface to capillary pressure and is defined as

$$Ca = \frac{\mu_o V}{\gamma} \quad (7.1)$$

where V is the droplet velocity and μ_o is the viscosity of the continuous phase. In the upstream channel section, $Ca = O(0.01)$ indicating capillary forces are dominant at the interface, resulting in spherical drops. The capillary number is useful in determining conditions where droplet breakup is expected to occur. Several different forms of the capillary number have been used to characterize tipstreaming[24, 25]. In this Chapter, we use the standard definition given in Eq. (7.1) due to the simplified geometry.

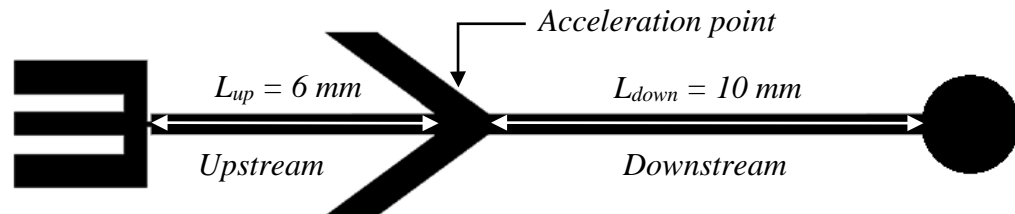


Figure 7.2 Diagram of flow focusing geometry, additional microchannels, and merge point downstream of droplet production geometry.

The increase in liquid supplied by the additional channels results in an increase in velocity of the fluid and drops. Depending on the amount of additional liquid supplied, drop velocities can reach 200 to 400 mm/s in the downstream channel section. The increase in velocity results in an increase in the viscous stresses acting on the droplet interface. Due to the increased viscous stresses,

tipstreaming is observed to occur at the rear of the droplets downstream of the acceleration point. Images of thread formation are taken using the microscope and high speed camera setup describe in Chapter 3.

7.3 RESULTS AND DISCUSSION

7.3.1 ANALYSIS OF TIPSTREAMING FROM THE REAR OF A DROP

Tipstreaming from the rear of droplets is observed to occur for a range of specific Q_a values at a given surfactant concentration. Once a drop reaches the acceleration point, viscous forces increase and alter the droplet shape. An elongational flow field develops as fluid flows around the moving droplet. The fluid flow sweeps surfactant to the rear of the droplet, generating surfactant concentration gradients along the surface of the drop. The combination of viscous stresses and Marangoni stresses result in conditions similar to tipstreaming in a flow focusing geometry. The balance of these forces forms a sharp tip from which a thread is pulled. The thread then breaks up into smaller droplets which flow behind the parent droplet through the microchannel. Figure 7.3 shows the drop shape and the thread produced from the rear of the droplet.

A unique feature of rear drop tipstreaming is that thread formation does not occur immediately after acceleration. Depending on operating conditions, thread formation occurs between 0.1 mm and 10 mm downstream of the acceleration point. The distance at which the onset of tipstreaming is observed downstream of the acceleration point is defined as P_{down} . Figure 7.4 plots this distance from the acceleration point where tipstreaming is observed as a function of the additional

continuous phase flow rate for three different surfactant concentrations. At large values of Q_a , plotted on the x-axis, tipstreaming is observed at distances close to the acceleration point. As the additional continuous phase flow rate is decreased, tipstreaming is observed at distances further from the acceleration point. At Q_a values below the lowest point plotted for each surfactant concentration, a thread does not form prior to the droplet reaching the end of the exit channel. Large values of Q_a result in instantaneous breakup of the drop upon entering the acceleration point.

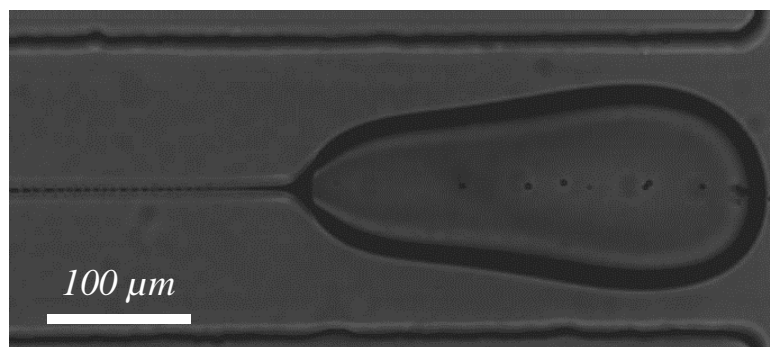


Figure 7.3 Image of droplet traveling through a microchannel after acceleration. Thread formation occurs at the rear of the droplet as continuous phase flows past the drop.

In these devices, the Reynold's number is small meaning that once the droplet has passed the acceleration point the velocity should remain constant. However, this assumes a constant cross section of the device. In fact, droplet speed increase as the droplet moves down the channel. The data points in Figure 7.5 show the measured speed of a droplet as a function of distance from the acceleration point for $Q_a = 150 \mu\text{l}/\text{min}$. This implies the cross sectional area of the channels is decreasing at increasing distances from the acceleration point. The microchannel

is made of PDMS which has a relatively low Young's modulus, $E \approx 1$ MPa [26]. At high flow rates, it has been shown that the pressure driven flow within a microchannel deforms the channel height[27].

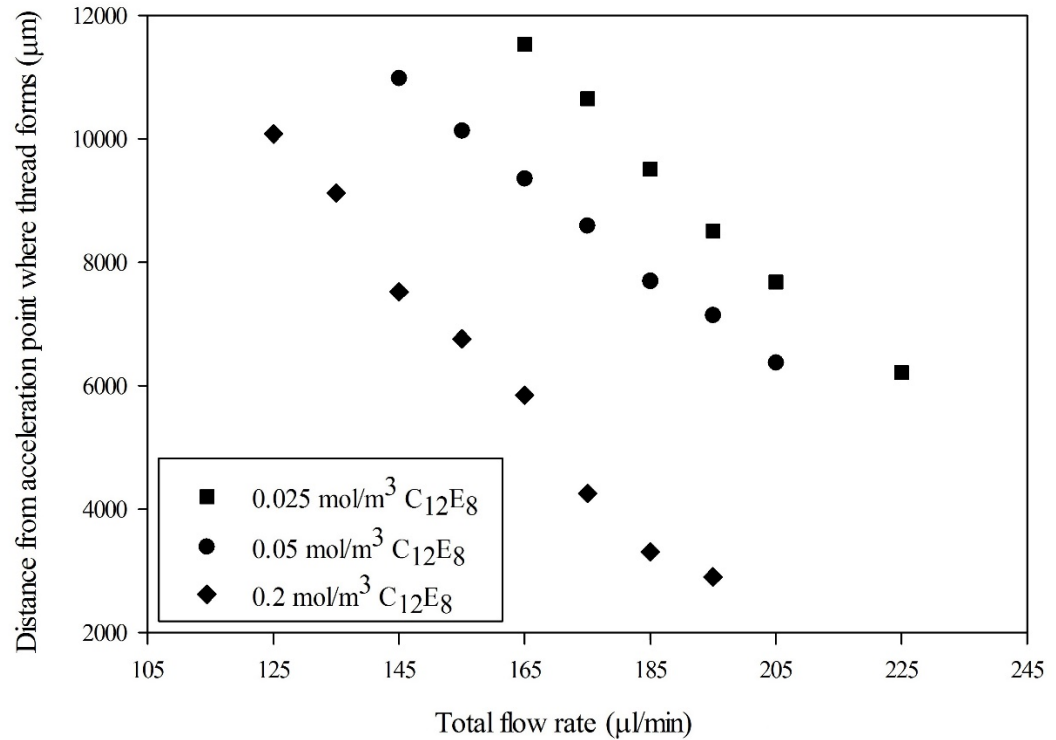


Figure 7.4 Distance downstream of the acceleration point at which thread formation is observed as a function of the total liquid volumetric flow rate. The \blacklozenge represent a surfactant concentration of $0.2 \text{ mol}/\text{m}^3$ C_{12}E_8 , \bullet represent a surfactant concentration of $0.05 \text{ mol}/\text{m}^3$ C_{12}E_8 , and \blacksquare represent a surfactant concentration of $0.025 \text{ mol}/\text{m}^3$ C_{12}E_8 .

Dendukuri *et al.* have characterized this effect in microfluidic channels and give an estimate of the channel height change as[28]

$$\Delta h(x) \approx \frac{w_{out} P(x)}{E_{PDMS}}. \quad (7.2)$$

Here, P is the pressure within the channel as a function of x , the distance from the channel exit. The pressure within the channel is estimated using the Hagen-Poiseuille equation,

$$P_{channel}(x) = \frac{128\mu_o x(Q_d + Q_c + Q_a)}{\pi D_H^4} + P_{atm}, \quad (7.3)$$

which yields a pressure drop of approximately 1 atmosphere across the total downstream channel length. This results in a maximum deviation of 40 microns in channel height for $Q_a = 150 \mu\text{l}/\text{min}$. To characterize the impact of this height change, the maximum fluid velocity, given by

$$V_{max} = \frac{2(Q_d + Q_c + Q_a)}{w_{out}(h_o + \Delta h(x))}, \quad (7.4)$$

is estimated as a function of distance from the channel exit. Combining Eqs. (7.2), (7.3), and (7.4) yields the predicted maximum fluid velocity, described by

$$V_{max} = \frac{2(Q_d + Q_c + Q_a)}{w_{out} \left(h_o + \frac{128\mu_o w_{out}(Q_d + Q_c + Q_a)x}{\pi D_H^4 E_{PDMS}} + P_{atm} \right)}, \quad (7.5)$$

which increases at increasing distance from the acceleration point.

The solid line in Figure 7.5 shows the change in the predicted maximum fluid velocity due to the deformation of the PDMS for $Q_a = 150 \mu\text{l}/\text{min}$. The predicted fluid velocity and droplet velocity change by a similar amount over the length of the downstream channel. This indicates the change in droplet speed is a result of the PDMS deformation. An important note is the predicted maximum fluid velocity is lower than the measured droplet velocity. This difference in flow

is what generates the viscous stresses on the interface sweeping surfactant to the rear of the droplet.

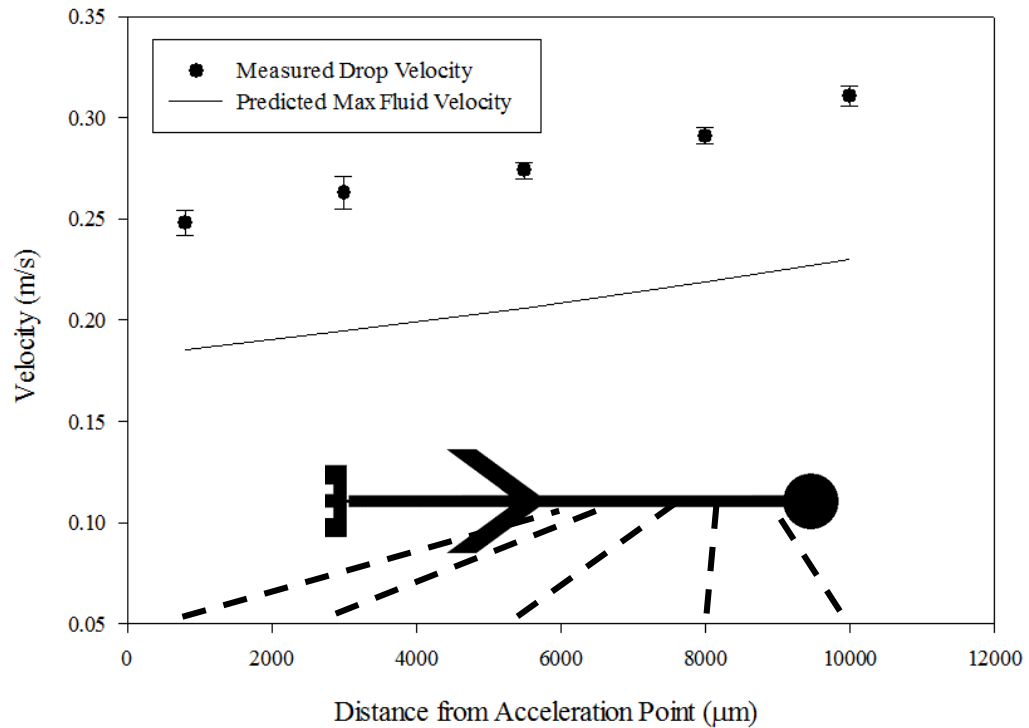


Figure 7.5 Values for measured droplet velocity and predicted maximum fluid velocity as a function of distance from the acceleration point for $Q_a = 150 \mu\text{l}/\text{min}$. The \bullet represent the measured droplet velocities and the solid line is the predicted maximum fluid velocity given by Eq. (7.5). The channel image illustrates the approximate location within the exit channel.

As the drop velocity increases, the viscous stresses acting on the droplet interface increase. When the drop velocity is high enough, the necessary balance between viscous and Marangoni stresses is reached and tipstreaming occurs. As described previously, the capillary number is used to characterize droplet breakup. In order to determine the capillary number, the interfacial tension of the droplets must be estimated for each of the different surfactant concentrations. The interfacial tension, γ , depends on the lifetime of the interface and transport of

surfactant. Using the kinetically controlled adsorption argument from Chapter 4, the value of $Bi(Pe\delta)$ is very small for these experiments, $10^{-5} < Bi(Pe\delta) < 10^{-4}$ [29]. This indicates that kinetic rates of adsorption are significantly slower than those of diffusion. An estimate of surfactant concentration on the interface can be made from this assumption. The flux of surfactant to a clean interface in the kinetic limit is $j_{ads} = \beta C_{\infty} \Gamma_{\infty}$.

The time available for adsorption in the upstream section can be determined from the upstream drop velocity, V_{up} , and the upstream channel length, L_{up} . Surfactant also continues to adsorb to the droplet interface in the downstream section. The additional time available for adsorption is estimated from the droplet velocity when tipstreaming occurs, V_{down} , and the distance from the acceleration point, P_{down} . Thus, the interfacial concentration of surfactant on the drop can be estimated as

$$\Gamma = \beta C_{\infty} \Gamma_{\infty} \left(\frac{L_{up}}{V_{up}} + \frac{P_{down}}{V_{down}} \right). \quad (7.6)$$

Interfacial tension values for the drop are determined from the surfactant coverage estimate using the generalized Frumkin interfacial equation of state, Eq. 4.5.

A small error in the interfacial tension is introduced by this approximation since drop velocity changes as a function of position within the channel. However, the increase in droplet speed results in a very short residence time for the exit channel. This means only a small deviation in the amount of time available for surfactant adsorption is introduced. Estimating this error in interfacial tension shows a difference of less than 0.5 mN/m. Additionally, interfacial coverages are

estimated to be relatively low for the cases studied here, $0.15 \leq \frac{\Gamma}{\Gamma_{\infty}} \leq 0.3$. The relatively low surface coverage and small interfacial tension change indicates the assumption results in only a small error in the estimated interfacial tension values. An important note is for all cases where tipstreaming is observed the coverage is above the minimum surface coverage criteria proposed by de Bruijn for tipstreaming[4].

Once droplet velocities and interfacial tension values are determined, capillary numbers of the drops can be estimated at the point tipstreaming begins. Determining the capillary numbers for the experimental results presented in Figure 7.4 shows tipstreaming occurs at similar capillary numbers for identical values of the additional continuous phase flow rate, Q_a . Plotting the capillary number where tipstreaming is observed collapses the results for different surfactant concentrations onto a single capillary curve, see Figure 7.6. The result is interesting since droplets from the three different surfactant concentration experiments have different velocities and different surfactant coverages for the same value of Q_a . This implies there is a critical capillary number needed to observe tipstreaming for a given additional phase flow rate.

Another important point is the critical capillary number increase with increasing additional phase flow rate values. This suggest tipstreaming requires increased viscous stresses to form a thread at high values of Q_a . Our hypothesis for this result is based on the confinement of the droplets. Higher volumetric flow rate values result in larger PDMS channel height deformations. This results in less

droplet confinement requiring additional viscous stress to generate droplet breakup. The amount of confinement is similar for the different surfactant concentration experiments at a given value Q_a .

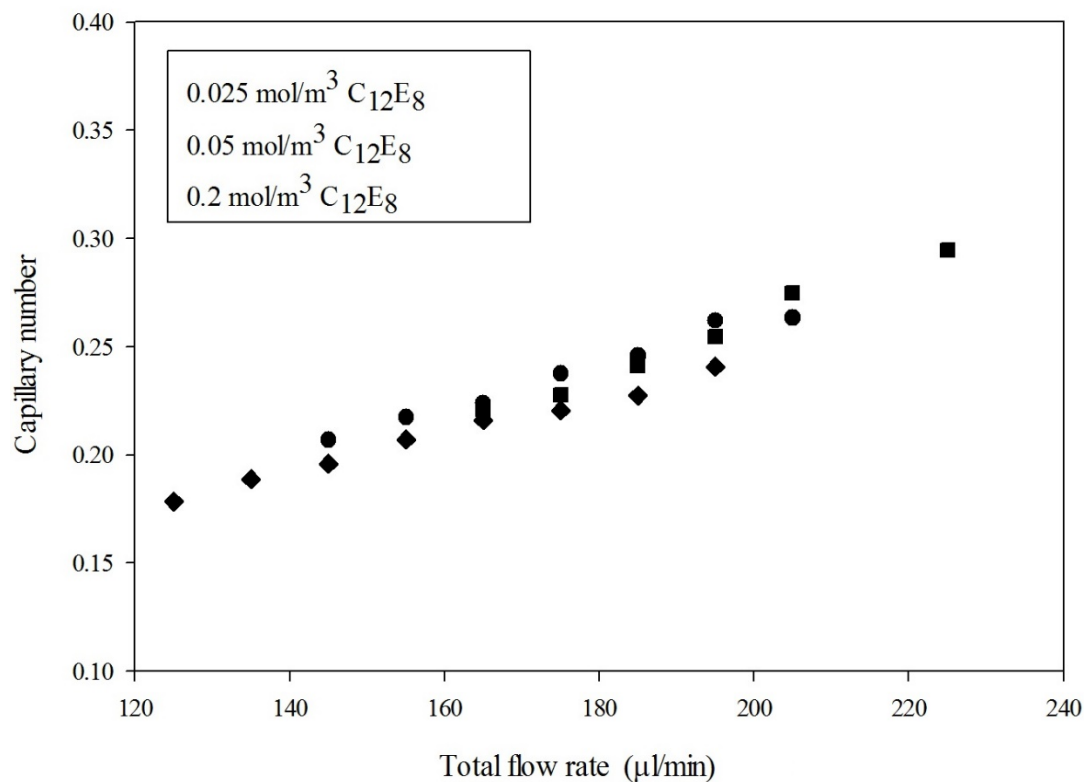


Figure 7.6 Estimated values of the capillary number at which tipstreaming occurs as a function of the total liquid volumetric flow rate. The \blacklozenge represent a surfactant concentration of $0.2 \text{ mol/m}^3 \text{ C}_{12}\text{E}_8$, \bullet represent a surfactant concentration of $0.05 \text{ mol/m}^3 \text{ C}_{12}\text{E}_8$, and \blacksquare represent a surfactant concentration of $0.025 \text{ mol/m}^3 \text{ C}_{12}\text{E}_8$.

Mulligan and Rothstein found very similar results during their drop confinement experiments[18]. As in our case, a critical capillary number was required for them to observe tail formation. Values of their critical capillary number range from 0.05 to 0.15. In cases where a tail forms, they observe a decrease in the required critical capillary number at increasing confinement. The confinement effect is comparable to our results. At lower additional continuous

phase liquid flow rate values, the channel deformation is smaller resulting in increased confinement and lower critical capillary numbers. Understanding the role of confinement in tipstreaming could potentially impact flow focusing geometry designs to improve the usefulness of tipstreaming. Confinement effects may also explain the sustained thread formation recently observed in a less confined flow focusing geometry[7]. This result is important in understanding the tipstreaming phenomenon and requires additional study.

7.3.2 DEVELOPMENT OF OPERATING DIAGRAMS

Characterizing the conditions needed to observe tipstreaming from the rear of a droplet allows for better understanding of the phenomena. An operating diagram is useful to determine the physical bounds of the tipstreaming system. Understanding the physical limits also allows for determining the controlling physics important to rear drop tipstreaming. As in the case of flow focusing based tipstreaming, an operating diagram can be constructed using the relevant physical timescales important in the process.

There are four relevant time scales for tipstreaming at the rear of a drop. These time scales are used to develop an operating diagram similar to those generated for tipstreaming in a flow focusing geometry. The result is an estimate of the expected conditions required to observe tipstreaming from the rear of a droplet. The first important time scale to consider is the lifetime of the drop interface prior to the onset of tipstreaming. This can be determined from the

upstream channel length, the point where thread formation occurs, and the droplet velocity. The resulting lifetime of the interface is

$$\tau_{interface\ lifetime} = \left(\frac{L_{up}}{V_{up}} + \frac{P_{down}}{V_{down}} \right), \quad (7.7)$$

which is the same estimate used in determining the capillary number of the droplets described above. The life time of the interface is used to determine the time available for surfactant adsorption onto the droplet surface. The time scale for convection along the interface is

$$\tau_{convection} = \frac{a}{V_{down}}, \quad (7.8)$$

which is important in characterizing the rate at which surfactant is convected to the rear of the drop. Here, a is the droplet diameter. Higher rates of convection lead to sharper gradients in interfacial surfactant concentration and thus larger Marangoni stresses.

Surfactant adsorption is also important in determining the interfacial tension of the droplet. The time scale for kinetically limited surfactant adsorption is

$$\tau_{ads} = \frac{1}{\beta C_{\infty}}. \quad (7.9)$$

This time scale is also important to the development of operating diagrams described in Chapter 4. A characteristic time scale for surfactant desorption can also be determined. However, this desorption time scale is much longer than a drops resident time suggesting conditions are in the irreversible adsorption limit. Lastly, the time required for interfacial tension gradient relaxation characterizes

how quickly an interfacial tension gradient will relax to equilibrium and is given by

$$\tau_{relaxation} = \frac{\mu_o a}{RT\Gamma_\infty}. \quad (7.10)$$

Using the ratio of time scales relevant for surfactant adsorption and surface relaxation results in a dimensionless concentration, \bar{C} . The dimensionless concentration characterizes the surfactant effects on the interface and is identical to the dimensionless concentration of Eq. 4.18 in Chapter 4. Similarly, the ratio of time scales for the life time of the interface and convection yield a dimensionless drop velocity given by

$$\bar{V} = \left(\frac{V_{down}}{V_{up}} \right) \left(\frac{L_{up}}{a} \right) + \frac{P_{down}}{a}. \quad (7.11)$$

The dimensionless droplet velocity characterizes the viscous stress acting on the droplet. Using these dimensionless parameters, an operating diagram for tipstreaming from the rear of a drop is constructed. The operating diagram uses experimental data, including the data shown in Figure 7.4, plotted in terms of dimensionless droplet velocity and dimensionless concentration.

When constructed in terms of \bar{V} and \bar{C} , the operating diagram for a series of experiments altering Q_a and C_∞ is shown in Figure 7.7. Several experimental series for different surfactant concentrations and flow rates are shown. The black circles represent conditions where tipstreaming is observed from the rear of a droplet. As in the case with microscale tipstreaming, there is a specific region

within the operating diagram where tipstreaming from the rear of the droplet is observed.

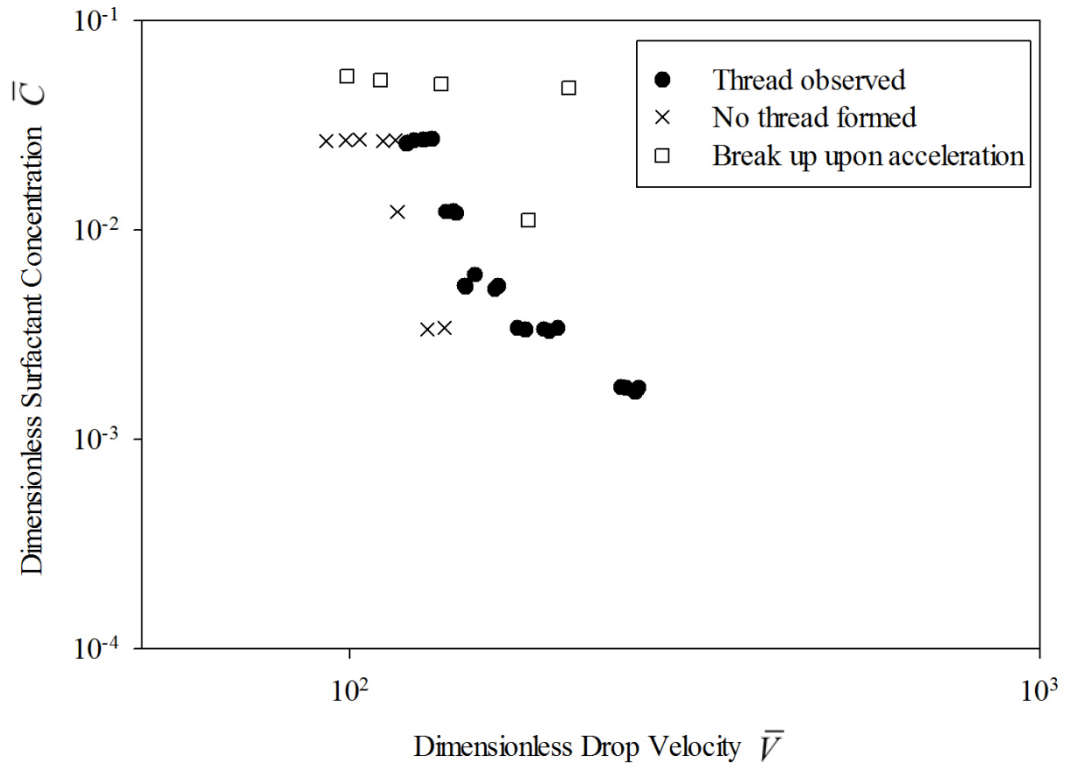


Figure 7.7 Experimental operating diagram for tipstreaming from the rear of a droplet. The ● symbols represent conditions where tipstreaming from the rear of a droplet is observed, × represent conditions where no thread is observed at the exit channel of the device, and □ represent conditions where non-tipstreaming droplet breakup occurs immediately upon entering the acceleration point.

This region is bounded by conditions which result in two non-tipstreaming cases. The first is droplets enter the downstream section of the exit channel and never develop a thread at the rear of the drop, represented by × symbols. Threads are generally absent for small surfactant concentrations and low droplet velocities. Lack of surfactant at the interface or small viscous stresses prevent Marangoni stresses from developing. This results in the droplets remaining intact until exiting the microchannel. The second case results in the breakup of the droplet upon

entering the acceleration point, represented by white squares. This is due to high viscous stresses and low interfacial tension values. Droplets undergo non-tipstreaming drop breakup as the front of the droplet moves faster and pulls away from the rear of the droplet. Droplet breakup within the acceleration point occurs at capillary numbers similar to those observed by Stone *et al.* in elongational flow field breakup experiments[19].

Boundaries encompassing this tipstreaming region can also be determined. First, tipstreaming criteria developed by de Bruijn found a minimum surfactant coverage needed to observe tipstreaming[4]. Based on his results, below interfacial concentrations of $\frac{\Gamma}{\Gamma_{\infty}} \leq 0.1$, thread formation does not occur. This limit is used to determine a minimum surfactant concentration needed to observe tipstreaming. Figure 7.8 reproduces the experimental data from Figure 7.7 with a boundary line showing the minimum surfactant concentration. Below this minimum concentration, thread formation is not expected.

In addition to the lower surfactant coverage limit, two additional bounds of constant capillary number are empirically fit to the tipstreaming region. These bounds generate a range of capillary numbers over which thread formation is observed at the rear of a drop. Capillary numbers higher than the upper bound, $Ca = 0.35$, result in droplet breakup within the acceleration point. Capillary numbers lower than the lower bound, $Ca = 0.15$, do not display any droplet breakup or thread formation. Note that the range of capillarity numbers reported here is very similar to the range observed for tipstreaming in flow focusing geometries[24]. These capillary numbers provide basic criteria needed to observe thread formation. The

operating diagram allows for estimating conditions needed to observe tipstreaming from the rear of a droplet. The additional role of drop confinement will also influence the conditions needed to observe thread formation. Additional work is needed to more rigorously characterize the effect of confinement on the conditions where tipstreaming from the rear of a droplet is observed. This may include altering the size of the parent droplets or changing the Young's modulus of the device material.

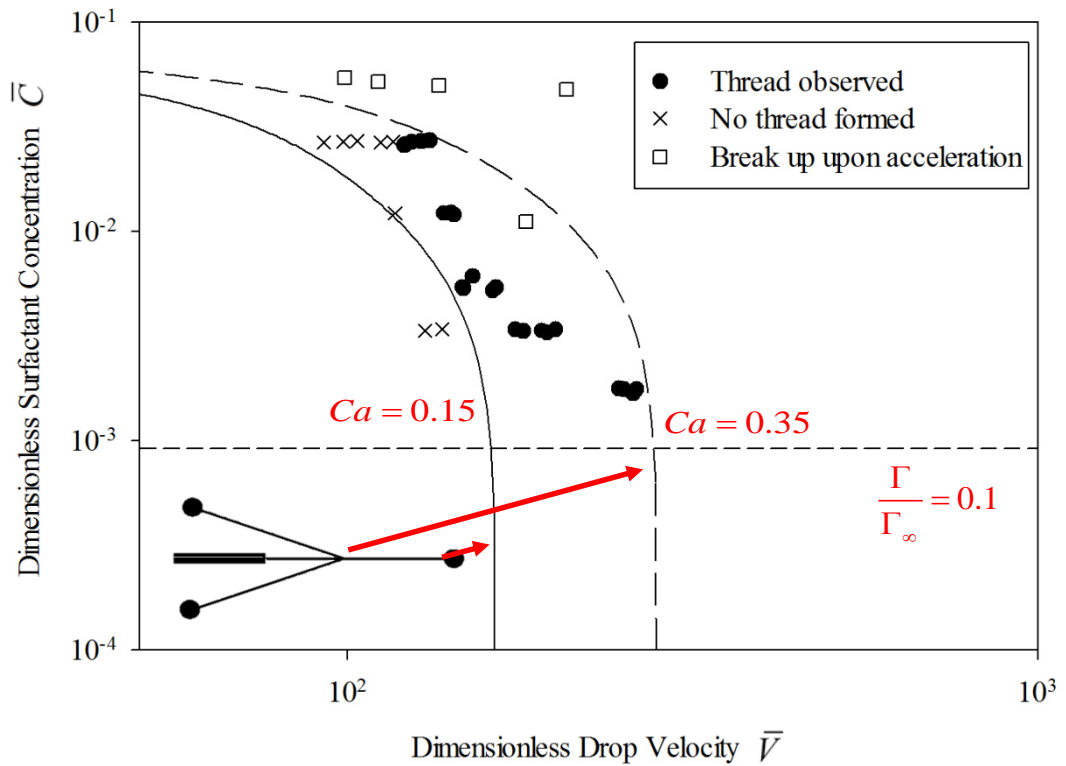


Figure 7.8 Experimental operating conditions reproduced from Figure 7.7 with three additional boundaries. The --- line is a boundary below which interfacial surfactant concentrations are too low to expect thread formation. The solid line is a line of constant capillary number of $Ca = 0.15$, below which thread formation is not observed. Lastly, the -- line is another line of constant capillary number, $Ca = 0.35$, above which droplet breakup within the acceleration point is observed.

7.4 CONCLUSIONS

Tipstreaming is a unique phenomenon able to generate droplets much smaller than the characteristic length scales of the system. The results of this Chapter demonstrate that tipstreaming is a universal phenomenon. Tipstreaming occurs in many different geometries and flow fields. The work presented here examines tipstreaming at the rear of a larger parent drop traveling in a microchannel. Thread formation occurs at the rear of droplets traveling in a confined exit channel after acceleration. The onset of tipstreaming occurs at varying distances from the acceleration point. Experiments measuring droplet velocity show the drops continue to accelerate while traveling through the exit channel. Deformation of the microchannel is the suspected cause for the continued droplet acceleration. As drop velocity increases, viscous stresses acting on the interface increase. If viscous stresses are large enough to generate the required Marangoni stress for tipstreaming, thread formation occurs.

The capillary number is used to scale the effects of different drop velocities and interfacial tension values. Tipstreaming occurs at similar capillary numbers for a given additional continuous phase flow rate, Q_a . The dependence on Q_a suggests droplet confinement is important in determining the capillary number where thread formation occurs. Additionally, an operating diagram is developed for tipstreaming from the rear of a droplet. The operating diagram shows a specific region of tipstreaming similar to that observed for flow focusing operating diagrams. We have developed basic criteria which bound the observed tipstreaming region. Boundaries including a minimum surfactant coverage and critical capillary

numbers can be placed around the tipstreaming region. These bounds act as a guide to determine the conditions where thread formation is expected to occur. This analysis demonstrates rear drop tipstreaming as a potential method of parallelizing thread formation as well as a new geometry in which to study the tipstreaming phenomenon.

1. Fernandez, J.M. and G.M. Homsy, *Chemical reaction-driven tip-streaming phenomena in a pendant drop*. *Physics of Fluids*, 2004. **16**(7): p. 2548-2555.
2. Lee, W., L.M. Walker, and S.L. Anna, *Role of geometry and fluid properties in droplet and thread formation processes in planar flow focusing*. *Physics of Fluids*, 2009. **21**(3).
3. Suryo, R. and O.A. Basaran, *Tip streaming from a liquid drop forming from a tube in a co-flowing outer fluid*. *Physics of Fluids*, 2006. **18**(8): p. 13.
4. De Bruijn, R.A., *Tipstreaming of drops in simple shear flows*. *Chemical Engineering Science*, 1993. **48**(2): p. 277-284.
5. Lee, W., Walker, L. M., and Anna, S. L., *Competition Between Viscoelasticity and Surfactant Dynamics in Flow Focusing Microfluidics*. *Macromolecular Materials and Engineering*, 2011. **296**(3-4): p. 203-213.
6. Ward, T., M. Faivre, and H.A. Stone, *Drop Production and Tip-Streaming Phenomenon in a Microfluidic Flow-Focusing Device via an Interfacial Chemical Reaction*. *Langmuir*, 2010. **26**(12): p. 9233-9239.
7. Jeong, W.C., et al., *Controlled generation of submicron emulsion droplets via highly stable tip-streaming mode in microfluidic devices*. *Lab on a Chip*, 2012. **12**(8): p. 1446-1453.
8. Lee, W., *Microscale thread formation as a mechanism to generate submicron droplets*, 2010, Ph.D. thesis, Department of Chemical Engineering, Carnegie Mellon University: Pittsburgh, PA. p. 186.
9. Martz, T.D., et al., *Microfluidic Generation of Acoustically Active Nanodroplets*. *Small*, 2012. **8**(12): p. 1876-1879.
10. Bretherton, F.P., *The Motion of Long Bubbles in Tubes*. *Journal of Fluid Mechanics*, 1961. **10**(2): p. 166-188.
11. Fuerstman, M.J., et al., *The pressure drop along rectangular microchannels containing bubbles*. *Lab on a Chip*, 2007. **7**(11): p. 1479-1489.
12. Tung, K.Y., C.C. Li, and J.T. Yang, *Mixing and hydrodynamic analysis of a droplet in a planar serpentine micromixer*. *Microfluidics and Nanofluidics*, 2009. **7**(4): p. 545-557.
13. Sarrazin, F., et al., *Experimental and numerical study of droplets hydrodynamics in microchannels*. *Aiche Journal*, 2006. **52**(12): p. 4061-4070.

14. Wang, Y.C. and P. Dimitrakopoulos, *Low-Reynolds-number droplet motion in a square microfluidic channel*. Theoretical and Computational Fluid Dynamics, 2012. **26**(1-4): p. 361-379.
15. Kinoshita, H., et al., *Three-dimensional measurement and visualization of internal flow of a moving droplet using confocal micro-PIV*. Lab on a Chip, 2007. **7**(3): p. 338-346.
16. Vananroye, A., P. Van Puyvelde, and P. Moldenaers, *Effect of Confinement on Droplet Breakup in Sheared Emulsions*. Langmuir, 2006. **22**(9): p. 3972-3974.
17. Olbricht, W.L. and D.M. Kung, *The Deformation and Breakup of Liquid-Drops in Low Reynolds-Number Flow through a Capillary*. Physics of Fluids a-Fluid Dynamics, 1992. **4**(7): p. 1347-1354.
18. Mulligan, M.K. and J.P. Rothstein, *The effect of confinement-induced shear on drop deformation and breakup in microfluidic extensional flows*. Physics of Fluids, 2011. **23**(2).
19. Stone, H.A., B.J. Bentley, and L.G. Leal, *An Experimental-Study of Transient Effects in the Breakup of Viscous Drops*. Journal of Fluid Mechanics, 1986. **173**: p. 131-158.
20. Janssen, J.M.H. and H.E.H. Meijer, *Droplet breakup mechanisms: Stepwise equilibrium versus transient dispersion*. Journal of Rheology (1978-present), 1993. **37**(4): p. 597-608.
21. Ha, J.-W. and L.G. Leal, *An experimental study of drop deformation and breakup in extensional flow at high capillary number*. Physics of Fluids (1994-present), 2001. **13**(6): p. 1568-1576.
22. Bentley, B.J. and L.G. Leal, *AN EXPERIMENTAL INVESTIGATION OF DROP DEFORMATION AND BREAKUP IN STEADY, TWO-DIMENSIONAL LINEAR FLOWS*. Journal of Fluid Mechanics, 1986. **167**: p. 241-283.
23. Janssen, P.J.A. and P.D. Anderson, *Surfactant-covered drops between parallel plates*. Chemical Engineering Research & Design, 2008. **86**(12A): p. 1388-1396.
24. Anna, S.L. and H.C. Mayer, *Microscale tipstreaming in a microfluidic flow focusing device*. Physics of Fluids, 2006. **18**(12): p. 121512.
25. Moyle, T.M., L.M. Walker, and S.L. Anna, *Predicting conditions for microscale surfactant mediated tipstreaming*. Physics of Fluids, 2012. **24**(8): p. 082110-21.

26. Gervais, T., et al., *Flow-induced deformation of shallow microfluidic channels*. Lab on a Chip, 2006. **6**(4): p. 500-507.
27. Hardy, B.S., et al., *The deformation of flexible PDMS microchannels under a pressure driven flow*. Lab on a Chip, 2009. **9**(7): p. 935-938.
28. Dendukuri, D., et al., *Stop-flow lithography in a microfluidic device*. Lab on a Chip, 2007. **7**(7): p. 818-828.
29. Eggleton, C.D. and K.J. Stebe, *An adsorption-desorption-controlled surfactant on a deforming droplet*. Journal of Colloid and Interface Science, 1998. **208**(1): p. 68-80.

CHAPTER 8**THE EFFECT OF OPERATING CONDITIONS ON THE SIZE OF DROPLETS GENERATED VIA TIPSTREAMING****8.1 INTRODUCTION**

The size of droplets formed within microfluidics typically depends upon a characteristic length scale of the geometry used to form the drops [1-4]. As previously mentioned, soft lithography based devices are limited in resolution to 10 μm [5, 6]. Tipstreaming is a technique which relies on hydrodynamics to determine the limiting length scale, allowing for the production of droplets approximately a micron in size [7-11]. However, until this point, the specific size of the droplets has not been discussed within this work. Despite previous experimental and modeling based studies of tipstreaming, droplet sizes are typically approximated. Additionally, little is reported about how operating conditions effect the size of the thread or droplets.

Previous studies have suggested different conditions within the tipstreaming regime produce droplets of different sizes [7, 8, 10]. Experimental observations made by Anna and Mayer claim that decreasing the flow rate ratio, defined as $\phi = Q_d / Q_c$, appears to decrease thread diameter and the diameter of the drops resulting from breakup [7]. Lee *et al.* also suggest the exit channel geometry and viscosity ratio have an impact on thread and droplet size [8]. Initial experiments have also given indication that droplet size does change with operating conditions. Figure 8.1 is a series of images from tipstreaming experiments using different surfactant concentrations. Visual inspection clearly shows thread and droplet size is greatly affected by changing the concentration of the surfactant. Determining the

effect of these operating conditions will aid in using tipstreaming as a tool to generate a desired size of drops.

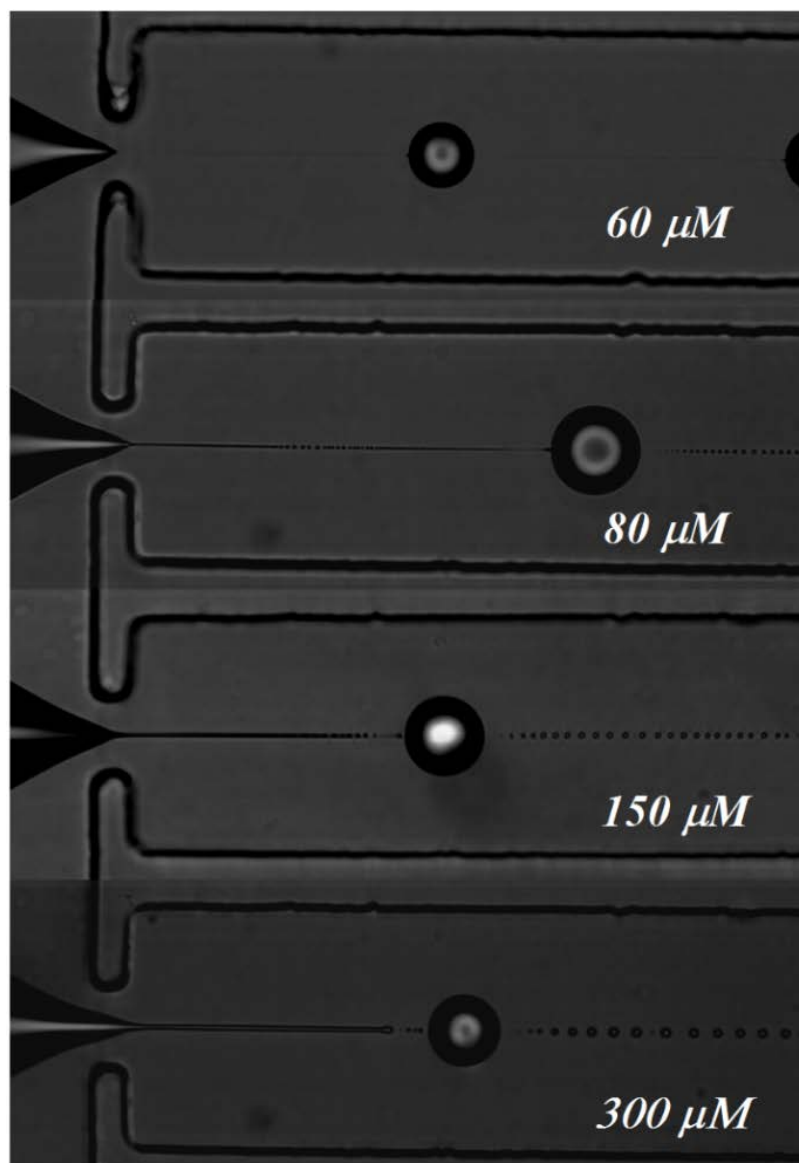


Figure 8.1. Four images of tipstreaming thread formation and droplets resulting from breakup. Flow rate values for all four cases are $Q_c = 80 \mu\text{l}/\text{min}$ and $Q_d = 2 \mu\text{l}/\text{min}$. The surfactant concentration of C₁₂E₈ given in micromolar values is reported for each of the four cases.

In addition to experimental evidence of altering thread and droplet size, recent modeling work also suggests the operating parameters have an impact on

thread size [11]. Detailed in Chapter 4, we have developed a model able to predict conditions for microscale tipstreaming based on an interfacial surfactant mass balance. The model not only estimates tipstreaming conditions but is also able to predict a thread diameter from the cone shape. Experimentally, the cone to thread transition is observed to occur at the center of the orifice. Because the model predicts cone geometry, a cutoff radius is set at the center of the orifice to eliminate the singularity at the cone tip. A predicted thread radius is then determined from the cutoff radius. The model estimates the thread diameter based only on upstream interfacial geometry required to observe tipstreaming. As a result, thread size effects from the changes in tipstreaming conditions may be captured. However, the effect of the downstream flow field and additional thread elongation will not be captured in the predicted thread size.

Lee *et al.* note that it is expected that the downstream flow field has a significant impact on thread formation, thread length, and thread diameter [8]. They also note the importance of the exit stream geometry and its effect on thread thinning. Additional modeling of thread size has been studied using asymptotic matching to analyze the cone to thread transition [12]. However, the system analyzed is significantly different from a flow focusing geometry and relies on gravity as the driving force for flow at the interface. In this Chapter, we compare predicted thread radius values from our tipstreaming model to experimentally measured thread and droplet sizes.

A difference in thread diameter and drop diameter resulting from thread breakup is also expected. The thread formed during tipstreaming undergoes

breakup into droplets due to a capillary instability. Drop size resulting from thread breakup primarily depends on the initial thread diameter [13]. Analysis of surfactant free system shows droplet diameter is approximately twice the initial thread diameter [14, 15]. Additionally, some work has examined surfactant effects on capillary instabilities [16-18]. One study uses slender body theory and a stability analysis of a thread with insoluble surfactant on the interface [19]. The results show there is an effect in the instability growth rate. Marangoni effects from surfactants dampen the capillary instability that causes thread breakup. However, the dominant wave number responsible for determining drop size was not significantly affected. The size relationship for the present system is difficult to determine due to the presence of an unknown amount of soluble surfactant on the thread interface. As a result, the size difference between the thread and droplets is likely similar to the results for a clean interface.

Lastly, Jeong *et al.* have reported the size of particles produced from tipstreaming droplets at different operating conditions [10]. However, this work examines the effect of altering the flow rate ratio at only two different values. A systematic study of operating conditions is needed to fully determine the role multiple parameters have on thread and droplet size. This work maps the relationship between droplet size and three experimental conditions, the ratio of the dispersed and continuous phase flow rates, $\varphi = Q_d / Q_c$, the surfactant concentration, and the magnitude of the liquid flow rates. The result is an outline detailing the necessary parameters to adjust in order to alter droplet size for use in various applications. We also test the effect two of these parameters have on the

size of hydrogel particles polymerized from tipstreaming droplets as a proof of concept for particle design.

8.2 MATERIALS AND METHODS

Tipstreaming experiments are performed in a rectilinear flow focusing geometry illustrated in Figure 3.1. The devices are fabricated using techniques similar to those described in Chapter 3 of this work. Device dimensions are the same as those reported in Table 3.1. For all experiments presented in this section, the continuous phase liquid used is light mineral oil (Fisher Scientific O1211, used as received). The optical measurement study uses deionized water as the dispersed phase with dissolved octaethylene glycol monododecyl ether ($C_{12}E_8$) (Sigma Aldrich P8925, used as received), in amounts between 80 $\mu\text{mol/l}$ to 300 $\mu\text{mol/l}$.

Droplet breakup and optical size measurements are visualized and recorded using an inverted microscope (Nikon Ti-U) with an attached high-speed camera (Phantom v9.1). Image analysis is used to determine the thread and droplet diameter with a minimum of 100 threads or droplets being measured for each set of conditions. Thread and droplet diameters are determined by analyzing the light intensity profiles for the vertical pixel rows of an image. A more detailed explanation of this measurement method is described in Chapter 3.4 of this work.

The fabrication technique for devices used in the droplet polymerization experiments requires an additional step to limit upstream polymerization of the dispersed phase. Once the initial PDMS layer is cured on the silicon wafer mold, a section of the device containing the upstream geometry and flow focusing junction is cut out and removed. Next, 0.5 wt% carbon black (Cabot Monarch 900, used as

received) is added to new uncured PDMS and re-poured into the section of the mold that was removed. The device is then cured and bonded to a flat slab of PDMS prepared using a similar technique to generate a similarly sized section of opaque PDMS. During bonding, the two blackened areas are aligned such that light cannot reach the upstream channels; only the exit channel of the device is visible. The length of the visible exit channel is approximately 2 cm. The carbon black prevents ultraviolet light from penetrating the PDMS and polymerizing the dispersed phase liquid before droplet formation occurs. This also restricts the visibility in these devices however, droplets can be observed once they flow into the clear exit channel.

The dispersed phase used in the droplet polymerization experiments is deionized water sparged with pure nitrogen gas at 80 °C for 1 hour to remove any dissolved oxygen. Poly(ethylene glycol) diacrylate (PEG-DA) (Sigma Aldrich 455008, Avg. $M_n = 700$) is filtered through a β -alumina column to remove stabilizers. Once filtered, the PEG-DA is added to the sparged water at a concentration of 4 wt% for all polymerization experiments. Additionally, 0.5 wt% of the photoinitiator 2-hydroxy-4'-(2-hydroxyethoxy)-2-methylpropiophenone (Aldrich 410896, used as received) is added to the disperse phase to increase the rate of the polymerization.

Rheological measurements of the hydrogel precursor are made using a TA Instruments DHR-2 rheometer with cup and bob geometry. These results indicate Newtonian behavior of the fluid over a wide range of shear rates and a viscosity of 1 ± 0.1 cP at 22°. After preparation of the polymer solution, C₁₂E₈ surfactant is

added to generate the desired surfactant concentration. An Omnicure series 2000 UV light source is used to polymerize the droplets in the microfluidic exit channel after they are formed. A fiber optic cable is connected to the Omnicure light guide with the end place approximately 1 cm above the microfluidic device, aligned with the exit channel. Once polymerized, the particles are collected and centrifuged under an acceleration of 100g for 5 minutes to ensure the larger primary droplets have been removed from the supernatant. The size of the hydrogel particles in the supernatant is measured by dynamic light scattering (DLS) using a Malvern Zetasizer Nano-ZS with a cuvette path length of 4.5 mm at a 173° backscattering angle. DLS measurements fit an autocorrelation function to sequential scattering patterns to determine the diffusion coefficient of the light scattering species. The Stokes-Einstein relationship correlates the diffusion coefficient to a hydrodynamic radius. We use the mobile interface correlation given by

$$d_{drop} = \frac{kT}{2\pi\mu D} \quad (8.1)$$

where k is the Boltzmann constant, T is the temperature, μ is the viscosity of the continuous phase liquid, and D is the measured diffusion coefficient resulting from fitting the autocorrelation function. Larger hydrogel particle sizes are measured off chip, after centrifugation, using a 90x oil immersion objective.

8.3 RESULTS

8.3.1 OPTICAL MEASUREMENTS OF DROPLETS

There are many parameters which influence microscale tipstreaming. Fluid properties, device geometry, and surfactant properties alone make up a large

experimental parameter space. However, the effect that primary operating conditions have on drop size must first be determined. Values for primary operating conditions are easily varied experimentally within the tipstreaming region. This allows their effect on drop size to be readily isolated and measured. Understanding the relationship between operating conditions and drop size will have the largest impact for a range of tipstreaming based applications. Additionally, application specific constraints generally set the properties of the fluids or surfactants used, limiting the number of adjustable parameters for a given system.

Three primary operating conditions are important to the tipstreaming phenomenon. Two of these are the continuous and dispersed phase volumetric flow rates, Q_c and Q_d . In the context of tipstreaming, the continuous phase flow rate, Q_c , and the volumetric flow rate ratio, $\varphi = Q_d / Q_c$ are used to characterize thread formation. This is because tipstreaming only occurs at small flow rate ratio values [7]. The third condition is surfactant concentration. Tipstreaming occurs between 10 and 300 $\mu\text{mol/l}$ for the C_{12}E_8 surfactant used in this study. In this work, the effect of each of these parameters on drop size is determined. Optically measured drop sizes are used to determine the size change of the small droplets produced from thread breakup. Due to optical limits, the fixed conditions are selected for a given experimental series to generate threads and droplets on the larger end of the possible size range. This practice allows for determining the effect of the varied parameter while still producing droplets large enough to measure optically. The

trend in droplet size is expected to be similar when using conditions which generate droplets too small to optically measure.

To vary the flow rate ratio, a fixed continuous phase flow rate of $Q_c = 80 \mu\text{l}/\text{min}$ is selected for all experiments. The dispersed phase flow rate is varied such that $0.011 \leq \varphi \leq 0.025$. An initial dispersed phase flow rate of $Q_d = 2 \mu\text{l}/\text{min}$ is selected to allow steady state to be attained in a reasonable time. The surfactant concentration is fixed at $300 \mu\text{mol}/\text{l}$. Once the microfluidic device has maintained steady state tipstreaming, images of the thread and droplets are recorded. Image analysis detailed in the background section of this work is used to determine the average droplet and thread diameter. Once image acquisition is completed, the dispersed phase flow rate is decreased resulting in new value of φ and the measurement process is repeated after reaching steady state. The resulting sizes measured for this series of experiments are shown in Figure 8.2.

Figure 8.2 shows the droplet diameter changes by a factor of two over the range of flow rate ratios studied. At values above $\varphi = 0.025$, droplet formation exhibits a jetting form of breakup, no longer producing multiple droplets from a single thread. Additionally, at flow rate ratios smaller than $\varphi = 0.011$, the dispersed phase syringe pump is unable to maintain the pressure needed to sustain the interface position within the flow focusing geometry. The higher pressure from the continuous phase syringe pump forces the dispersed phase liquid up the inlet channel, preventing tipstreaming. The error bars represent the standard deviation in the measured sizes.

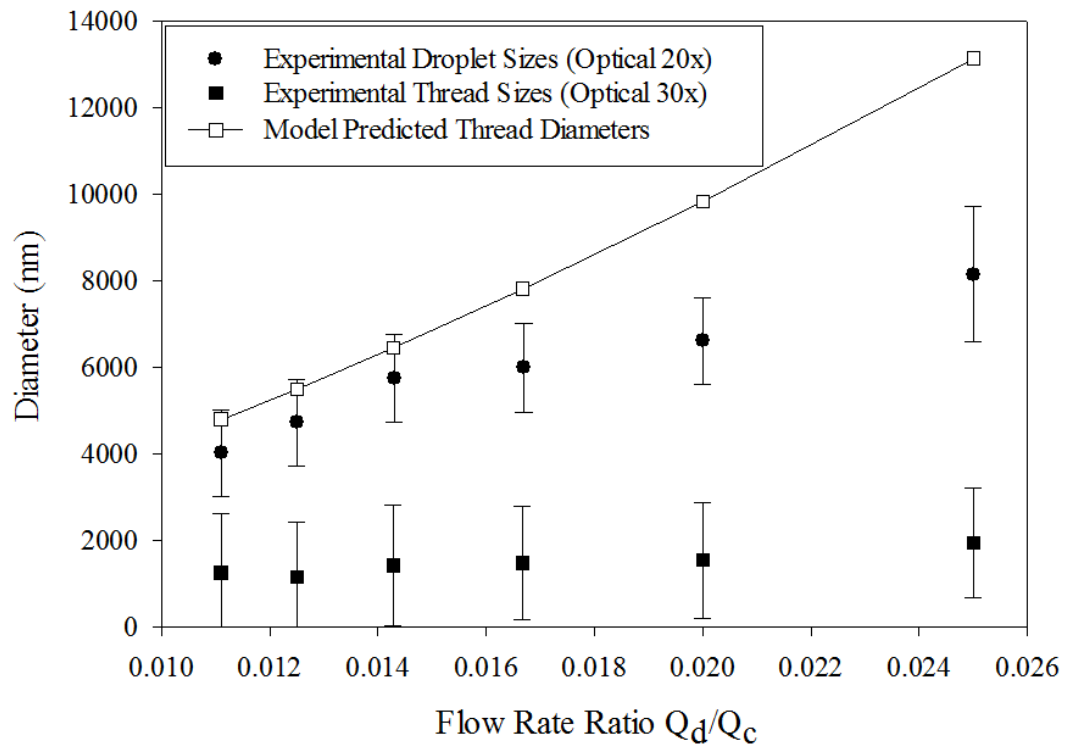


Figure 8.2. On chip optically measured thread and droplet diameters as a function of flow rate ratio. The continuous phase flow rate is kept fixed at $Q_c = 80 \mu\text{l}/\text{min}$ and surfactant concentration is $300 \mu\text{mol}/\text{l}$. Model predicted thread sizes are determined at the location of the open symbols for different flow rate ratio values. The line is added to indicate the estimated model result between calculated points.

Figure 8.2 shows no trend in thread diameter with changing flow rate ratio. However, a trend in thread size is potentially concealed by measurement error due to small thread sizes close to the measurement limit of the optical technique. An important detail is the measured size distribution of droplets within a single thread. For a single thread, the droplet size of the final 3 to 4 droplets is noticeably smaller than the average droplet sizes. The reason is due to pinch off effects as the thread detaches from the upstream interface. To reduce the impact of this effect, only droplets formed from the middle of the droplet train are used in determining the

average droplet size reported. This mitigates effects not associated with altering the tipstreaming conditions.

We have previously developed a model capable of predicting microscale tipstreaming conditions [11]. The model is able to determine conditions appropriate for thread formation to occur. The basis for the model is to determine if the cone shape required for tipstreaming is able to form. The model allows for predictions of the tipstreaming operating conditions and thread diameter. The predicted thread diameters from the tipstreaming model are also shown in Figure 8.2. Similarly to the experimental results, the thread size is predicted to increase with increasing flow rate ratio. Here, the open symbols represent conditions where the model was solved to determine the predicted thread diameter. The line is used as an approximation of model results between the calculated points. The agreement indicates that the model captures the upstream physics responsible for changing the droplet size. The results also indicate that φ impacts the flow field and interfacial dynamics during tipstreaming, as shown experimentally in previous work [7]. Lastly, the agreement is further evidence that the tipstreaming model captures the important physics of the tipstreaming mechanism.

The model predicts thread sizes much larger than those measured. However, the model does not account for the elongational effects of the exit channel geometry. The model only captures physics that effect the upstream formation of the cone. The elongational effect from fluid flow in the downstream exit channel causes significant thinning of the thread diameter. However, altering φ does not have a significant effect on the flow field downstream of the flow focusing orifice.

The total flow rate of the exit channel is only altered by 2.5% over the range of φ values tested. As a result, the thinning effects on the thread in the exit channel are similar for the entire series of experiments. Due to this, the trend in thread size predicted by the model is still expected experimentally and is a result of upstream effects during thread formation.

In addition to flow effects, surfactant concentration is known to impact the tipstreaming mechanism. The effect of surfactant concentration on drop size is an important relationship to determine. In another series of experiments, flow rate values were again selected to generate droplets large enough to be optically measured. These flow conditions, $Q_c = 80 \mu\text{l}/\text{min}$ and $\varphi = 0.025$, are the same as the largest droplet size reported in Figure 8.2. In this experiment series, droplet sizes are measured for surfactant concentrations ranging from $60 \mu\text{mol}/\text{l}$ to $300 \mu\text{mol}/\text{l}$. Experiments and measurements are performed in an identical manner to those for the φ series. Figure 8.3 shows the results of drop size measurements for different values of surfactant concentration in the dispersed phase.

Surfactant concentration has a significant effect on the size of the droplets. The results show the droplet diameter changes by a factor of 4 over the surfactant concentration range studied. Surfactant concentrations above $300 \mu\text{mol}/\text{l}$ approach the limit of the tipstreaming operating space while concentrations lower than $60 \mu\text{mol}/\text{l}$ generate droplets too small to be optically measured. Thread diameters are below measurement limits of the optical technique and are not reported. The tipstreaming model is used to predict the effect of changing surfactant concentration. The model results shown in Figure 8.3 indicate that higher

surfactant concentration require a larger conical tip in order to maintain the balance between viscous and Marangoni stresses. This increased volume of dispersed phase fluid results in the predicted thread size increasing with increasing concentration.

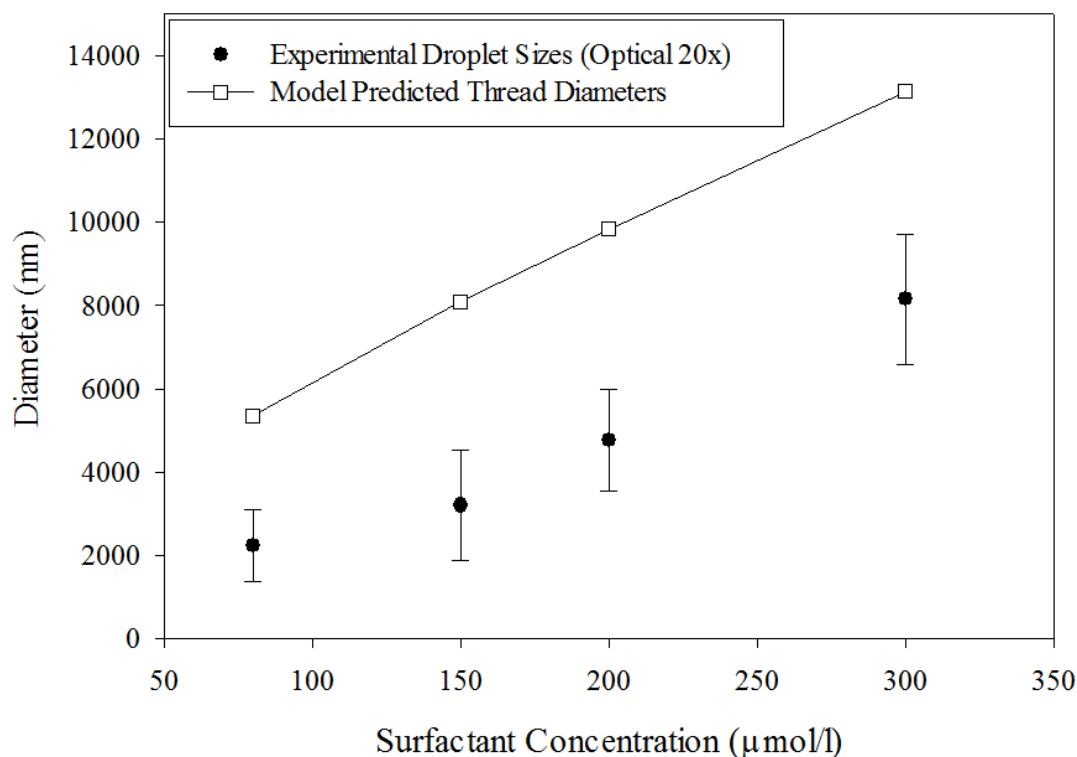


Figure 8.3. On chip optically measured droplet diameter as a function of surfactant concentration. The continuous and dispersed phase flow rates are kept fixed at $Q_c = 80 \mu\text{l/min}$ and $Q_d = 2 \mu\text{l/min}$. Model predicted thread sizes are determined at the location of the open symbols for different surfactant concentrations. The line is added to indicate the estimated model result between calculated points.

The predicted increase in thread size is similar in magnitude to the size increase observed experimentally. The agreement suggests the model captures the interfacial physics important to tipstreaming. Again, the predicted thread size is larger than measured drop size due to the lack of downstream thinning effects in the model. However, as in the case of varying φ , the flow field downstream of the flow focusing orifice is similar for the entire series of experiments. This allows the

trend in droplet size resulting from surfactant effects to be observed without changes in downstream thinning effects.

As with surfactant concentration, the magnitudes of fluid flow rates is important in the thread formation process. The effect of altering the flow rate magnitude of both phases simultaneously is investigated. The flow rate ratio is fixed at $\varphi = 0.025$ and a surfactant concentration of $300 \mu\text{mol/l}$ is used. These conditions are again selected to generate droplets large enough to measure optically. The range of flow rates tested spans the operating region of tipstreaming. The size of the resulting droplets as a function of the magnitude of the continuous phase flow rate are shown in Figure 8.4.

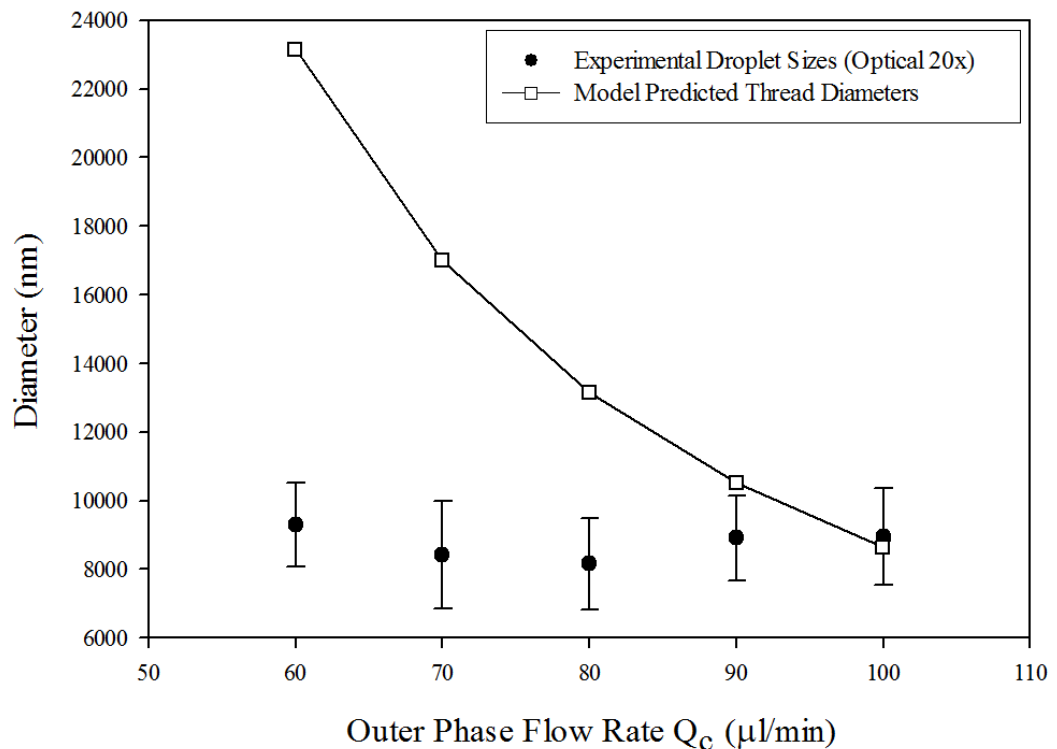


Figure 8.4. On chip optically measured droplet diameter as a function of flow rate magnitude. The flow rate ratio is kept constant such that $Q_d = Q_c / 40 \mu\text{l/min}$ and surfactant concentration is $300 \mu\text{mol/l}$. Model predicted thread sizes are determined at the location of the open symbols for different flow rate magnitudes

at constant φ . The line is added to indicate the estimated model result between calculated points.

Figure 8.4 shows little change in experimentally measured droplet size over the flow rate magnitudes tested. Flow rates smaller than $Q_c = 60 \mu\text{l}/\text{min}$ result in a squeezing mode of droplet breakup. Flow rates larger than $Q_c = 100 \mu\text{l}/\text{min}$ result in a jetting mode of droplet breakup. Based on the droplet size measurements, there is no change in droplet diameter with varying the magnitude of the continuous phase flow rate at fixed φ . The nearly constant size is an interesting result since altering both flow rates simultaneously seems to greatly affect the thread formation process. Lee *et al.* have previously characterized the effect altering flow rate magnitudes have on primary droplet sizes and thread length formed during tipstreaming [8]. Those results show a significant change in primary droplet diameter and thread length, both of which are also observed in the current experiments. However, there is no noticeable difference in the droplet size produced from thread breakup.

A possible reason why drop size is independent of the magnitude of the continuous phase flow rate at fixed φ is the coupling of upstream and downstream effects. In the surfactant concentration and flow rate ratio experimental series, upstream and downstream effects are present. However, the downstream thinning effect is essentially the same across each series of experiments. That is not the case for altering the magnitude of the continuous phase flow rate at fixed φ . A significant change in the downstream thinning effect occurs over the range of flow rates studied. The volumetric flow rate of the fluid in the exit channel increases by

over 50% across the experimental series. Since the measured drop size does not change with flow rate magnitude, it is possible changes in the upstream thread formation process are offset by changing downstream exit channel elongation effects. The predictions from the tipstreaming model do not agree with the measured drop size for changing flow rates. This reinforces the hypothesis that the downstream flow field is having a significant role in setting the droplet size. In the previous two cases the model is able to capture the trend in size. However, in the case where the downstream flow field change is more significant, the model is unable to predict the unchanging droplet size.

8.3.2 MEASUREMENT OF HYDROGEL PARTICLES

The results of these series of experiments is a guide to generate droplets over a range of sizes. To demonstrate the use of this guide, polymer hydrogel particles are formed from the droplets generated via tipstreaming. Hydrogel particles are formed by adding a photo crosslinkable polymer to the dispersed phase. The hydrogel particle experiments focused on polymerizing droplets smaller than the optically measurable limit. Results from these experiments will determine if the size trends measured for micron sized drops translate to submicron length scales.

Care must be taken in equating the size of the particles measured to the size of the droplet produced via tipstreaming. There are several post formation processes that potentially lead to a difference between droplet and particle sizes. This includes a potential change in the size upon polymerization and effects from

the additional off chip processing. Once collected off chip, the particles are centrifuged to remove larger particles formed from primary droplets. The supernatant containing the micron sized particles is then collected and transferred to a light scattering cuvette. These processes have the potential to alter the size of the particles. Additionally, the amount of water swelling the particles can change the size distribution during the time delay between formation and size measurement. As a result of these factors, a direct link from particle size to droplet size is not made.

A suitable dispersed phase formulation of surfactant, UV crosslinkable polymer, and photoinitiator is used to polymerize the droplets into hydrogel particles. It is important that the surfactant controls the interfacial physics of the tipstreaming process. This requires low polymer and photoinitiator concentrations such that the $C_{12}E_8$ surfactant dictates the interfacial physics. Figure 8.5 shows the measured operating diagram for the PEG-DA/ $C_{12}E_8$ system compared with the operating diagram for the pure $C_{12}E_8$ system available in the literature [11]. Good agreement is observed between the two operating diagrams indicating the tipstreaming mechanism is not disrupted by the presences of the polymer and photoinitiator. Any deviation is likely the result of small device geometry effects since different soft lithography molds were used.

The size of hydrogel particles polymerized from tipstreaming droplets is investigated while altering the flow rate ratio and surfactant concentration. Results are shown in Figures 7 and 8. Figure 8.6 shows the size of polymerized drops formed at different flow rate ratios over the same range as the optical size

measurements with $Q_c = 80 \mu\text{l}/\text{min}$. A surfactant concentration of $80 \mu\text{mol}/\text{l}$ is used to generate smaller droplets based on the results shown in Figure 8.3. After thread formation has reached steady state, the UV light is applied to the exit section of the channel. The resulting polymerized hydrogel particles are then collected off chip. The sizes of the particles are measured using dynamic light scattering (DLS) to obtain better size resolution at these length scales. The mobile interface formulation of Stokes-Einstein is used since particles still containing over 95% water and a mobile interface is expected.

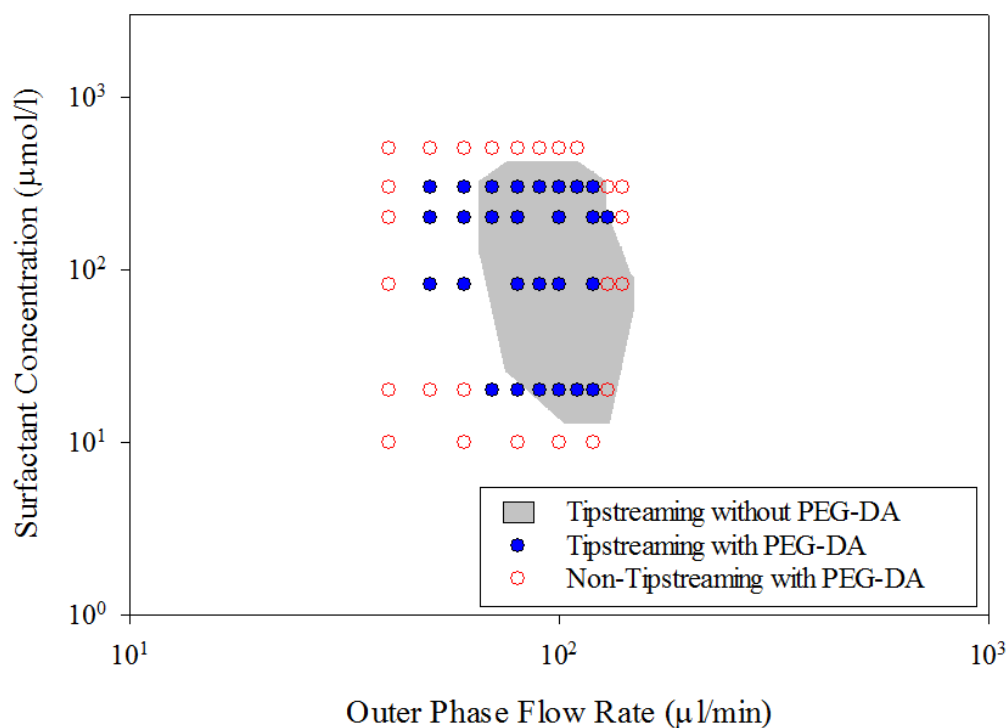


Figure 8.5. Tipstreaming operating diagram for both pure C_{12}E_8 system and for PEG-DA/ C_{12}E_8 system. The pure C_{12}E_8 operating diagram is reproduced from data in Ref. [11]. The shaded region represents conditions where tipstreaming is observed. Experiments using the PEG-DA/ C_{12}E_8 are plotted over the original operating diagram. Filled symbols represent conditions where tipstreamed is observed and open symbols represent some other mode of droplet breakup occurring.

In Figure 8.6, we see that particle sizes range from approximately 200 nm in diameter to over 1.5 microns. This indicates a large range in particle size is attainable over the range of φ . The error bars in Figure 8.6 represent one standard deviation of the DLS measured size distributions. This gives an indication of the polydispersity of particles made using tipstreaming. Figure 8.7 shows four representative DLS distributions for four of the data points given in Figure 8.6. The trend in size with changing φ is similar to the results observed by Jeong *et al.* for polymerized droplets [10]. Jeong *et al.* observe a decrease in particle size from approximately 380 nm in diameter to 170 nm when decreasing the flow rate ratio. These size ranges are similar to those presented in Figure 8.6. Further comparison of results is difficult since Jeong *et al.* only report the driving pressure for fluid flow and not flow rate value.

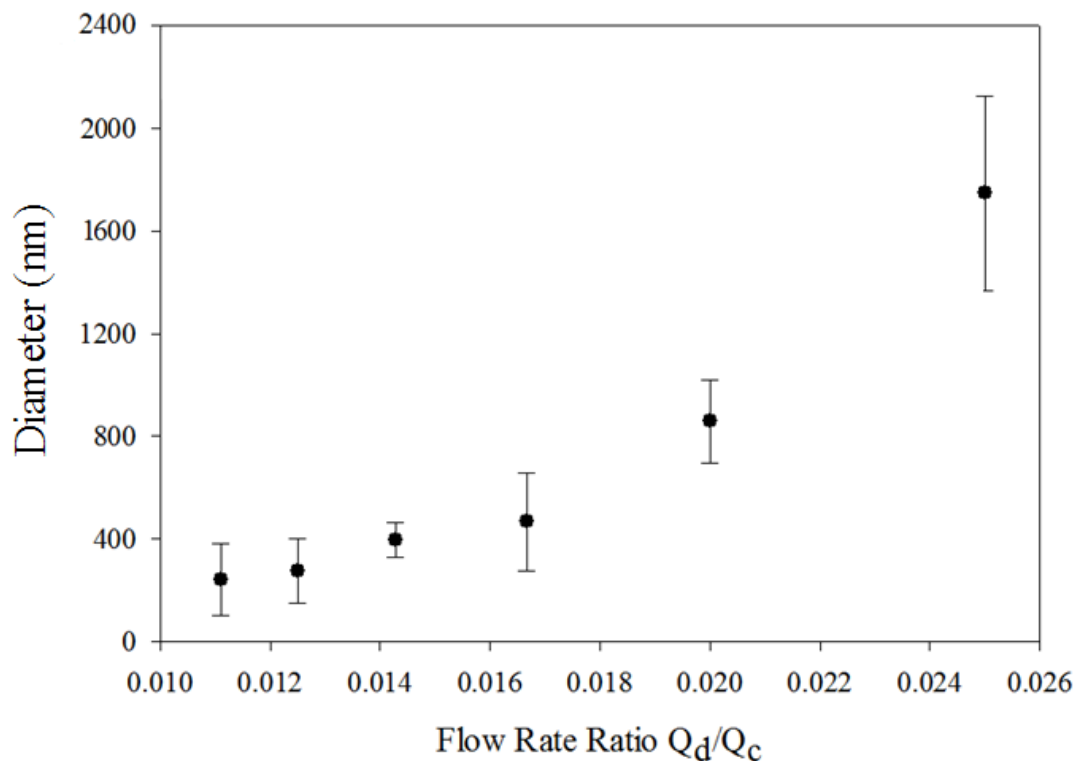


Figure 8.6. DLS measured post processed particle diameter as a function of flow rate ratio. The continuous phase flow rate is kept fixed at $Q_c = 80 \mu\text{l}/\text{min}$ and surfactant concentration is $80 \mu\text{mol}/\text{l}$. The error bars indicate one standard deviation in the particle size distributions measured using dynamic light scattering.

Figure 8.8 shows experimentally measure polymer particle sizes formed using different surfactant concentrations. The results show the particle diameter increases by over a factor of 4 across the surfactant concentration range studied. As in the case of optical size measurements, flow rates are fixed at $Q_c = 80 \mu\text{L}/\text{min}$ and $Q_d = 2 \mu\text{L}/\text{min}$. Particles generated at these conditions are larger than those in the previous case. As a result, two size measurement techniques are used to determine the particle diameter.

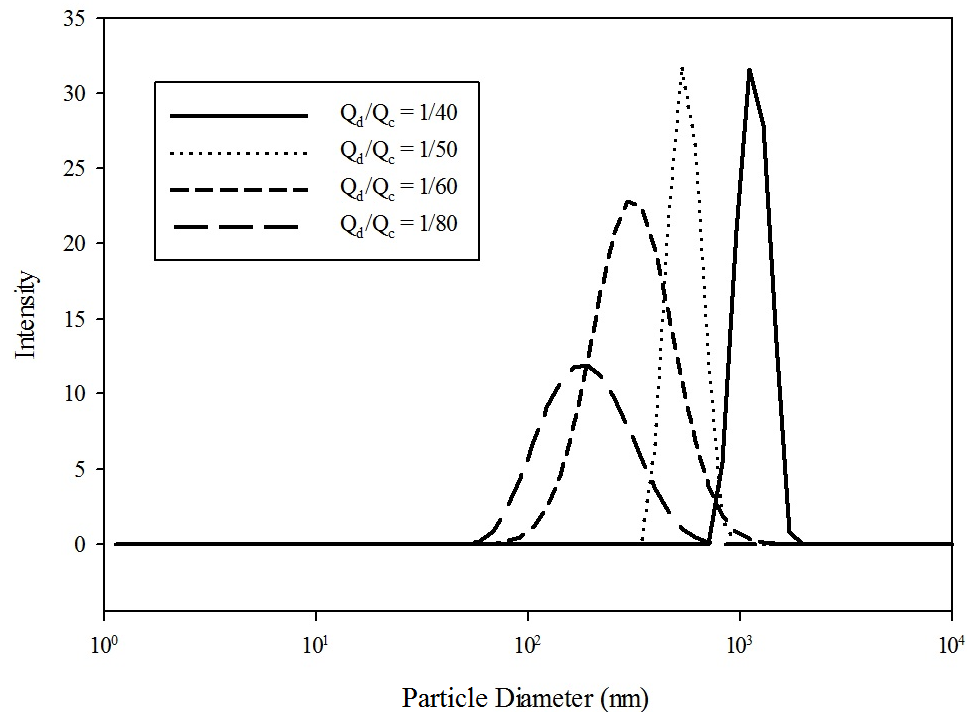


Figure 8.7 Dynamic light scattering intensity based size distributions determined using the mobile interface variant of the Stokes-Einstein relationship for flow rate ratios values of 1/40, 1/50, 1/60, and 1/80.

The smaller sizes are measured using DLS and larger droplets are measured off chip using bright field microscopy and a 90x magnification oil immersion objective. The results of both size measurement techniques for various surfactant concentrations are shown in Figure 8.8. The results again show the utility of tipstreaming as a tool to generate particles over a range of sizes. Particle sizes range from hundreds of nanometers to several microns in diameter.

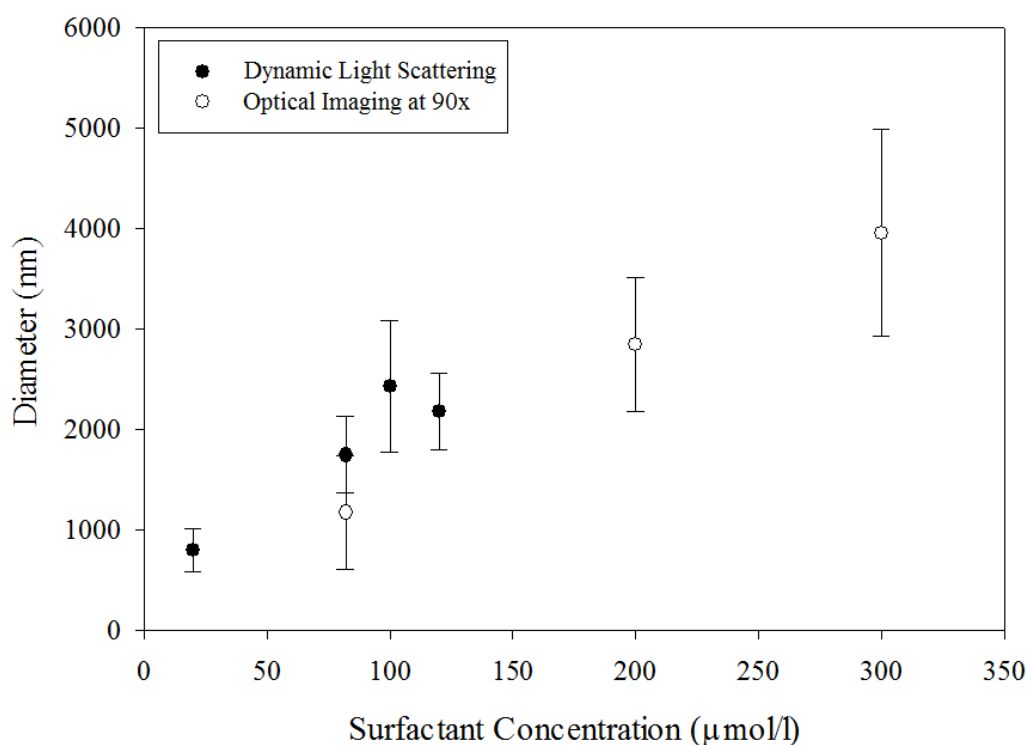


Figure 8.8. DLS and off chip optically measured post processed particle diameters as a function of surfactant concentration. The continuous and dispersed phase flow rates are kept fixed at $Q_c = 80 \mu\text{l/min}$ and $Q_d = 2 \mu\text{l/min}$. Filled in symbols represent measurements made using DLS and open symbols represent off chip optical measurements using a 90x magnification oil immersion objective.

8.4 DISCUSSION

Results show the ability to control droplet size by altering conditions within the tipstreaming operating region. The operating conditions that are observed to

generate the greatest change in the resulting droplet diameter are the flow rate ratio and the surfactant concentration. The availability of multiple parameters to alter droplet size is advantageous to comply with other application specific constraints. In the case of the volumetric flow rate ratio, increasing φ results in increased droplet diameters. The droplet diameter is observed to change by factor of two over the range of flow rate ratios studied while polymerized particle diameter changes by almost an order of magnitude.

The observed size change agrees with the physical picture of lower flow rate ratios resulting in smaller droplets. Based solely on a mass balance of the dispersed phase liquid, there are three potential effects of decreasing the flow rate ratio. First, the larger primary droplets decrease in size. Second, the rate at which the larger primary droplets are produced decreases. Finally, the diameter of the threads produced decreases. All three of these effects are observed during the experiments used to construct Figure 8.2. Additionally, similar relationships between droplet size and flow rate ratio have also been reported for non-tipstreaming droplet breakup modes in flow focusing geometries [20].

Similarly, tipstreaming at higher surfactant concentrations leads to larger droplet sizes. Initially, the trend in size is counterintuitive to what is expected physically. With additional surfactant in the system, the interfacial tension at the tip of the cone should be able to maintain very high curvatures, resulting in very small threads. However, as previous modeling work has shown, the interface near the tip becomes highly packed with surfactant, essentially reaching the maximum packing concentration [11, 21]. Additional surfactant at the interface would then

equate to a larger portion of the tip covered with the maximum amount of surfactant. As viscous forces pull a thread from the cone tip, a larger portion of the cone has a low enough interfacial tension to become part of the thread. This results in larger thread sizes and larger droplets resulting from thread breakup as the amount of surfactant is increased.

Our previously developed tipstreaming model is able to capture the effects of altering the surfactant concentration and the flow rate ratio. In both cases the predicted increase or decrease in size agrees with experimental results. The agreement indicates the model captures the upstream physics responsible for changing the droplet size. Upstream and downstream effects are both significant in determining the final size of the droplets generated. Upstream effects are changes in the tipstreaming cone as a result of changing operating conditions. Downstream effects are thinning of the thread caused by the exit channel flow field. The model used to predict thread sizes only accounts for upstream effects resulting in over predicting the thread diameters. However, in the experimental series where flow rate ratio and surfactant concentration were altered, downstream effects remained approximately constant.

In these cases, the upstream impact on drop size is expected to be observed and the model predicts the size change trends. In the changing flow rate magnitudes at fixed ϕ case, the upstream and downstream effects are both significantly altered across the experimental data series. As a result, the model is unable to predict the observed size trend. This indicates downstream effects have a significant impact on thread size. Additionally, Lee *et al.* measured thread length as a function of the

width of the exit channel [8]. Smaller exit channel widths were observed to generate longer threads, indicating exit channel elongational effects are important in determining thread size. Incorporating downstream dynamics within the tipstreaming model would allow for more accuracy in predicting experimental sizes.

Lastly, the size trends observed in the optical measurements are similar for the smaller polymer particle size measurements. The optically measured trends are expected to be similar for conditions which produce smaller drops. This is anticipated since the tipstreaming mechanism relies on physics which do not change in the hundred nanometer length scale range. Thread formation is observed to produce barely visible threads with diameters smaller than one micron in diameter. In this region of thread formation, the same physical principles apply and the insight gained from experiments presented here is still valid. Drop and particle sizes are observed to decrease with decreasing flow rate ratio. Additionally, the polymer particles and drops increase in size with increasing concentration. These results are significant in demonstrating tipstreaming as a technique to generate nanoscale materials. Also, the results validate the ability to select tipstreaming conditions to generate droplets or particles of a desired size. Small size differences between Figure 8.3 and Figure 8.8 are attributed to effects of the polymerization and measurement process discussed earlier. Production and measurement of these particles demonstrate tipstreaming as a viable tool to generate nanoscale materials.

8.5 CONCLUSIONS

The utility of tipstreaming is to make sub-micron droplets or particles. The results presented in this Chapter develop a guide to altering the tipstreaming conditions to change droplet size. Altering tipstreaming conditions are typically the easiest parameters to control and have the smallest impact on application specific constraints. Using these conditions to tune droplet size allows for tipstreaming to serve as a robust source of micron and sub-micron sized droplets. Three key results have come from the study of these two systems. First, the two most influential operating conditions on droplet size are the flow rate ratio and surfactant concentration. These parameters effect the size of both droplets generated and particles formed from droplets.

Second, the smallest of droplet and particle sizes occur at low values for both these parameters. Increasing these parameters results in larger droplets or particles generated. This allows for selecting conditions to generate droplets of a desired size. The range of droplet or particle sizes which can be made covers both nanometer and micron length scales. This shows tipstreaming offers flexibility to produce a large range of different sized droplets. Finally, trends in size are consistent for different systems. This implies the trends presented in this work have the ability to be applied to a lot of systems relevant to important applications.

The result of this Chapter is a guide to aid in the designed production of nanoscale materials relevant to a wide area of current research. Other parameters aside from operating conditions affect droplet size as well. Additional conditions which may impact drop size include surfactant type [22], liquid viscosities [23],

and device geometry [24]. These parameters are more system specific and typically more difficult to alter for a specific application. The effect of these parameters on the size of tipstreaming droplets requires further study.

1. Anna, S.L., N. Bontoux, and H.A. Stone, *Formation of dispersions using "flow focusing" in microchannels*. Applied Physics Letters, 2003. **82**(3): p. 364-366.
2. Link, D.R., et al., *Geometrically mediated breakup of drops in microfluidic devices*. Physical Review Letters, 2004. **92**(5): p. 054503.
3. Squires, T.M. and S.R. Quake, *Microfluidics: Fluid physics at the nanoliter scale*. Reviews of Modern Physics, 2005. **77**(3): p. 977-1026.
4. Dollet, B., et al., *Role of the channel geometry on the bubble pinch-off in flow-focusing devices*. Physical Review Letters, 2008. **100**(3).
5. Duffy, D.C., et al., *Rapid prototyping of microfluidic systems in poly(dimethylsiloxane)*. Analytical Chemistry, 1998. **70**(23): p. 4974-4984.
6. Whitesides, G.M. and A.D. Stroock, *Flexible methods for microfluidics*. Physics Today, 2001. **54**(6): p. 42-48.
7. Anna, S.L. and H.C. Mayer, *Microscale tipstreaming in a microfluidic flow focusing device*. Physics of Fluids, 2006. **18**(12): p. 121512.
8. Lee, W., L.M. Walker, and S.L. Anna, *Role of geometry and fluid properties in droplet and thread formation processes in planar flow focusing*. Physics of Fluids, 2009. **21**(3).
9. Ward, T., M. Faivre, and H.A. Stone, *Drop Production and Tip-Streaming Phenomenon in a Microfluidic Flow-Focusing Device via an Interfacial Chemical Reaction*. Langmuir, 2010. **26**(12): p. 9233-9239.
10. Jeong, W.C., et al., *Controlled generation of submicron emulsion droplets via highly stable tip-streaming mode in microfluidic devices*. Lab on a Chip, 2012. **12**(8): p. 1446-1453.
11. Moyle, T.M., L.M. Walker, and S.L. Anna, *Predicting conditions for microscale surfactant mediated tipstreaming*. Physics of Fluids, 2012. **24**(8): p. 082110-21.
12. Krechetnikov, R., *Structure of Marangoni-driven singularities*. Physics of Fluids, 2012. **24**(2): p. 022111.
13. Rayleigh, L., *On the capillary phenomena of jets*. Proceedings of the Royal Society of London, 1879. **29**: p. 71-97.
14. Tomotika, S., *Breaking up of a drop of viscous liquid immersed in another viscous fluid which is extending at a uniform rate*. Proceedings of the Royal Society of London Series a-Mathematical and Physical Sciences, 1936. **153**(A879): p. 0302-0318.

15. Meister, B.J. and G.F. Scheele, *Generalized Solution of Tomotika Stability Analysis for a Cylindrical Jet*. Aiche Journal, 1967. **13**(4): p. 682-&.
16. Young, Y.N., et al., *Influence of surfactant solubility on the deformation and breakup of a bubble or capillary jet in a viscous fluid*. Physics of Fluids, 2009. **21**(7).
17. Walker, J.R., *The Effect of Surfactants on the Breakup of an Axisymmetric Laminar Liquid Jet*, in *Department of Chemical and Biomolecular Engineering* 2012, University of Maryland: College Park.
18. Kwak, S., M.M. Fyrillas, and C. Pozrikidis, *Effect of surfactants on the instability of a liquid thread - Part II: Extensional flow*. International Journal of Multiphase Flow, 2001. **27**(1): p. 39-60.
19. Hansen, S., G.W.M. Peters, and H.E.H. Meijer, *The effect of surfactant on the stability of a fluid filament embedded in a viscous fluid*. Journal of Fluid Mechanics, 1999. **382**: p. 331-349.
20. Ward, T., et al., *Microfluidic flow focusing: Drop size and scaling in pressure versus flow-rate-driven pumping*. Electrophoresis, 2005. **26**(19): p. 3716-3724.
21. Eggleton, C.D., T.M. Tsai, and K.J. Stebe, *Tip streaming from a drop in the presence of surfactants*. Physical Review Letters, 2001. **87**(4): p. 048302.
22. Lee, W., *Microscale thread formation as a mechanism to generate submicron droplets*, 2010, Ph.D. thesis, Department of Chemical Engineering, Carnegie Mellon University: Pittsburgh, PA. p. 186.
23. Nie, Z., et al., *Emulsification in a microfluidic flow-focusing device: effect of the viscosities of the liquids*. Microfluidics and Nanofluidics, 2008. **5**(5): p. 585-594.
24. Chen, J.M., M.C. Kuo, and C.P. Liu, *Control of Droplet Generation in Flow-Focusing Microfluidic Device with a Converging-Diverging Nozzle-Shaped Section*. Japanese Journal of Applied Physics, 2011. **50**(10).

CHAPTER 9**CONCLUSIONS**

Tipstreaming is a unique method to generate micron sized droplets with many potential uses. This work provides several critical advances in the understanding and implementation of tipstreaming. The result is a useful tool to generate both droplets and particles over a range of sizes. The work presented in this thesis addresses several technical challenges which prevent using tipstreaming in important applications. The first of these challenges addresses developing a model capable of predicting tipstreaming for a given oil-water-surfactant system. The second challenge is developing a technique to remove the primary droplets from the sub-micron sized droplets of interest. Lastly, characterizing droplet size and how these sizes change with operating conditions is needed. Resolving these issues greatly increases the practicality of tipstreaming as a technique to generate micron sized droplets for specialized applications.

A solution to the first technical challenges is presented in Chapter 4. This work describes the development of a model capable of predicting concentration and flow rate values that will result in the microscale tipstreaming. The model is based on a conical interfacial geometry, a unique feature of tipstreaming in experiments. An interfacial mass balance of surfactant is used to determine conditions where the conical shape of the interface is able to be maintained. Physical constraints are applied which limit the feasible region for tipstreaming. These constraints include a global surfactant mass balance, the transition to jetting as inertia begins to influence drop breakup, and a dispersed phase fluid mass balance.

Experimental observations of microscale tipstreaming show good agreement with the predicted physical boundaries for tipstreaming. The agreement indicates the formulated interfacial surfactant mass balance adequately captures the important physics needed to maintain a conical interface. Additional simplification using a Henry's law formulation for the interfacial equation of state allows for rapid estimation of the tipstreaming boundaries. The linearized boundaries also readily show the role of device geometry and surfactant properties in the tipstreaming process. The results allow for rapidly determining conditions required to observe tipstreaming, greatly reducing the need for experimental testing of operating conditions. Additionally, the model has provided insight into the tipstreaming mechanism and increased the current understanding of the physics occurring at surfactant covered interfaces.

Chapters 5 and 6 present two different solutions to the second technical challenge, removing the larger primary droplets. Chapter 5 describes the development and implementation of a control system able to continuously generate a stream of micron sized droplet. This is accomplished through the use of a proportional active feedback control loop designed to maintain the position of the conical interface within the flow focusing geometry. Controlling the dispersed phase flow rate allows for continued thread production for several hours.

Experimental tuning of the control parameters is also performed. The proportional gain constant and set point value are systematically varied to determine the effect on thread formation. The standard deviation of the process value is used to determine controller stability. A range of operating parameters are

found to control thread formation in a stable manner with relatively small oscillations in the interface position. The result is a system capable of generating a continuous thread and thus stream of micron sized droplets. This greatly reduces the need for additional processing downstream as well as decreases waste of the feed stock chemicals. These features are important for applications which produce fragile material that could be damaged during primary droplet separation. The controller is another tool developed by this work to facilitate the use of tipstreaming in important applications.

The work in Chapter 6 develops and implements an alternative technique to eliminate the larger primary droplets from the micron sized drop stream. This is accomplished through the addition of an inline droplet separator located downstream of the flow focusing geometry. Details and principles of the design are outlined as well as efficiency of the separation at different flow conditions. Tuning the resistance to flow in one of the exit channels allows for manual manipulation of the flow profile within the separator geometry. When properly tuned, all of the larger primary droplets are eliminated from the micron sized droplet stream. The efficiency of the separation is found to depend on device operating conditions. This is likely due to increased interaction between the small drops and the larger primary droplets. On chip separation reduces post processing of the droplets and simplifies device parallelization. Additionally, primary droplets can potentially be collected and recycled, reducing feedstock chemical waste.

Experiments described in Chapter 7 show the universality of microscale tipstreaming. Tipstreaming has been observed for many different surfactant types,

fluid properties, and geometries. The work in this Chapter examines one of those alternative geometries in greater detail. Tipstreaming from the rear of an accelerating droplet is observed at a range of surfactant concentrations and drop velocities. The capillary number is used to characterize the effects of viscous stresses and capillary pressure acting on the drop interface. The analysis shows tipstreaming occurs at similar capillary numbers for experiments with different surfactant concentrations and drop velocities. The interesting result is the critical capillary number for tipstreaming increases with increasing additional fluid flow rate values. It is hypothesized that drop confinement is the cause for the observed dependence, however additional work is needed to confirm this idea. The results presented in this work demonstrates one of the many different systems in which tipstreaming is observed. Additionally, tipstreaming from the rear of a droplet has potential to increase micron size droplet production rates within a single microfluidic network.

Chapter 8 develops a guide to generate droplets of a desired size based on changing the tipstreaming operating conditions. The effect of surfactant concentration, flow rate, and flow rate ratio on droplet size is examined. Sizes examined are in the larger range of those possible to allow for optical measurements. It is found that both surfactant concentration and flow rate ratio have a significant impact on drop size. Conditions tested remained within the region of tipstreaming. Decreasing surfactant concentration and flow rate ratio results in a droplet size decrease by as much as a factor of two. Altering flow rate magnitude is not observed to have an impact on drop size. As a proof of concept,

hydrogel particles are generated from the micron sized drops. Particle size is observed to follow similar trends in size as the optically measured droplets. These results demonstrate the ability to use the observed size trends as a guide to generate drops or particles of a desired size for a given application. Additionally, the use of multiple tuning parameters allows for adhering to application specific constraints.

Collectively, this work addresses and solves multiple technical challenges inherent to microscale tipstreaming. These achievements include 1) a model capable of reducing the cost of determining tipstreaming conditions, 2) a controller capable of reducing feedstock waste and decreasing the need for additional product processing, 3) a separator which can be readily implemented in parallel systems to increase production rates, and 4) a design scheme to control the size of the micron sized drops being produced. These techniques and tools are critical to the implementation of microscale tipstreaming to generate nanoscale structures and materials.

APPENDIX A**MATLAB CODE FOR THE TIPSTREAMING MODEL**

This Appendix contains a copy of the Matlab code used to solve the tipstreaming model presented in Chapter 4 of this work. The first step taken by the model is to import all surfactant, fluid and geometric parameters. These parameters are defined within the sub-function `getvariables`. This allows for quickly changing parameters to observe the impact on the predicted operating diagram. Next, parameter matrices are defined which set the operating space the model will examine, shown in Figure 4.5. These parameters are the dimensionless flow rate, DES and dimensionless concentration, BCS.

The model looks for solutions to the mass balance equation at every combination of operating points within these matrices. Two for loops are used to vary the location within the two dimensional operating diagram. For a specific set of operating conditions, the model uses `fzero`, a root finding command, to attempt to find the cone angle. Here Eq. 4.17 is rearranged such that one side of the equation equals zero. The cone angle is then calculated by finding the root of the equation. The bounds of the search region are set such that one value is the upper limit on the cone size. This limit is represented by Eq. 4.20. The other limit is such that other physical boundaries prevent tipstreaming before this cone size is reached.

Once the cone angles is determined, individual physical properties based on the cone size are calculated. These properties include the cutoff radius, the interfacial tension and surfactant coverage profiles, and the number of moles of surfactant on the interface. The interfacial tension profile is determined by solving

Eq. 4.12. This is done for discretized r value points along the interface once the cutoff radius is known. The interfacial tension profile is converted to the interfacial surfactant concentration profile using the interfacial equation of state, Eq. 4.5. Calculating the surfactant concentration profile from the interfacial tension profile requires the use of an additional `fzero` command. The command is needed since Eq. 4.5 cannot be solved for Γ analytically. Both functions solved using `fzero` are monotonic, indicating the solution the model finds is the only possible solution. Numerical integration of the profile is used to determine the number of moles of surfactant on the interface.

Once the interfacial tension profile is known, conditions which require values below the minimum interfacial tension, Eq. 4.22, are eliminated. The estimated flux leaving the interface on the thread is determined. This is determined from the velocity of the interface at the cutoff radius and the value of the interfacial coverage profile at the cutoff radius. The flux leaving is compared to the flux of surfactant into the cone region supplied by the dispersed phase liquid. Conditions where the flux of surfactant leaving is greater than the flux in violate the physical boundary described in Eq. 4.21 and are thus unfeasible for tipstreaming.

Next, flow conditions within the thread are estimated. These are used to determine the flux of dispersed phase fluid through the thread. Conditions where the thread fluid flux is greater than the flow rate into the device are conditions which violate the physical boundary given by Eq. 4.24. Several different flow conditions are considered including plug flow, Hagen Poiseuille flow, and Dagan flow.

Conditions where the physical boundary is violated are identified to indicate conditions where tipstreaming is not plausible.

Solutions for the specific operating conditions are then reported in an external data file and the model continues on to the next set of conditions. The resolution of the model can be increased or decreased by altering the number of points within the operating condition matrices. The constructed operating diagram is plotted once all operating conditions have been tested. Standard run times are 2 to 3 hours for the operating condition matrix sizes in the code below using an Intel Core i5 2.54GHz dual core CPU with 3 GB of RAM.

Begin Model Code:

```
%Mass Bal. Model 10/31/2011 Developed by Todd Moyle C12E8
%Comment lines are marked via % Symbols

%Clear previous variables
clear
clc

%Open Parallel cores
matlabpool close
matlabpool open

%Start Timer
tic;

%Recent Edits: Comp ready, Conversion from cone to thread
%at center of orifice, General clean up
%File Name
%Par_Unbounded_r_c_Solver
```

```

% Get the date
thedata = datestr(now);
thedata(12) = '_';
thedata(15) = '-';
thedata(18) = '-';

%Properties of the system C12E8 Import
[mu_o, mu_i, delta_mu, a, b_orf_hw, w_or, R, T, gamma_inf, kappa, n, h
, ST_0, z, D_h, flow_ratio, w_c, gamma_EQ_Scale, beta, t_or] =
getvariables;

%Flow rate ratio factor
Flow_Factor = 1;

%Set up Dimensionless # Check Matrix
mat_length = 25;
min_DES = -2;
max_DES = 1;
min_BCS = -7;
max_BCS = 0;

%Conditions for Exp Region Only
% mat_length = 10;
% min_DES = -0.6;
% max_DES = -0.1;
% min_BCS = -4;
% max_BCS = -2;

%Dimensionless Concentration matrix
BCS_mat = logspace(min_BCS, max_BCS, mat_length);
%Dimensionless Flowrate matrix
DES_mat = logspace(min_DES, max_DES, mat_length);

%Check Solution to every matrix point
for ji = 1:length(DES_mat)
    %Set loop dimensionless flow rate
    DES = DES_mat(ji);

```

```

%Display Progress
clc
Percent = j i;
display(Percent)
parfor j k = 1:length(BCS_mat)
    clc

    %Set Sub-loop dimensionless concentration
    BCS = BCS_mat(j k);
    % Determined actual concentration
    C_inf = (R*T*gamma_inf*BCS)/(beta*mu_o*a);
    % units of mol/m^3

    %Determine actual flow rate
    Q_0 =
    (DES*R*T*gamma_inf*z*D_h^3)/(20/3*flow_ratio*mu_o*a^2*
    (1-w_or/(2*w_c))); % m^3/s

%=====

%Calculate capillary Number
Ca = mu_o*Q_0*a/(gamma_EQ_Scale*h*z)*(1/w_or-1/(2*w_c));
Time_abs = 0.15*(D_h)^3/(flow_ratio*Q_0*Ca); % Seconds

%=====

%Use try loop to obtain cone solution
try

%=====

%Find Solution to cone angle
theta_c_solution = fzero(@(theta_c)
beta*C_inf*gamma_inf*Time_abs*(2*pi*a^2) -
N_needed_fun(theta_c, DES, Flow_Factor), [atan((a-
w_or/2)/z), atan(a/(z+b_orf_hw))]);

%=====

```

```

%Find number of surfactant moles needed to maintain cone
[N_needed, ijk, max_gamma_grad, max_gamma] =
N_needed_fun2_mod(theta_c_solution, DES, Flow_Factor);

%Find number of surfactant moles that adsorbe in time
N_abs = beta*C_inf*gamma_inf*Time_abs*(2*pi*a^2);

%Fine cutoff radius
r_c = ((a/tan(theta_c_solution) - z-
b_orf_hw)/cos(theta_c_solution));

%Find Total interface length
s = a/sin(theta_c_solution);

%Determine plug flow in thread
FLOW_PLUG =
(Q_0/(w_or*h))*pi*(r_c*sin(theta_c_solution))^2;
FLOW_ACTUAL = flow_ratio*Q_0;
ST_r_c = ST_0 -
((3*delta_mu*Flow_Factor*Q_0*r_c^2*sin(theta_c_solution)*co
s(theta_c_solution)*(1/r_c^2-
1/s^2))/(w_or*h*(3*(cos(theta_c_solution))^2-1)));
hyd_r = 0.5*D_h;

%+++++

%No Delta P outside
Delta_P_outside_t_0 = 0;
P_thread_minus_P_Cone_tau_0 =
(ST_r_c)/(r_c*sin(theta_c_solution)) -
(ST_r_c*(cot(theta_c_solution)/r_c) -
2*delta_mu*Flow_Factor*Q_0/(w_or*h*r_c))+Delta_P_outside_t_
0;

%-----

```

```

FLOW_DELTA_P_0 =
(pi *(r_c*sin(theta_c_soluti on))^4*P_thread_mi nus_P_Cone_tau
_0)/(8*mu_i*t_or); %STILL HP
    FLOW_EFF_0 = FLOW_PLUG - FLOW_DELTA_P_0;

    if FLOW_ACTUAL < FLOW_EFF_0
        PHYSICAL_FLOW_0 = 1;
    el sei f FLOW_EFF_0 < 0
        PHYSICAL_FLOW_0 = 2;
    el se
        PHYSICAL_FLOW_0 = 0;
    end

%+++++
%Flow in Hagen-Poiseuille case
Delta_P_outsi de_t_HP = (-8*mu_o*Q_0*t_or)/(pi *hyd_r^4);
P_thread_mi nus_P_Cone_tau_HP =
(ST_r_c)/(r_c*sin(theta_c_soluti on)) -
(ST_r_c*(cot(theta_c_soluti on)/r_c) -
2*del ta_mu*Fl ow_Factor*Q_0/(w_or*h*r_c))+Del ta_P_outsi de_t_
HP;
%-----
    FLOW_DELTA_P_HP =
(pi *(r_c*sin(theta_c_soluti on))^4*P_thread_mi nus_P_Cone_tau
_HP)/(8*mu_i*t_or);
    FLOW_EFF_HP = FLOW_PLUG - FLOW_DELTA_P_HP;

    if FLOW_ACTUAL < FLOW_EFF_HP
        PHYSICAL_FLOW_HP = 1;
    el sei f FLOW_EFF_HP < 0
        PHYSICAL_FLOW_HP = 2;
    el se
        PHYSICAL_FLOW_HP = 0;
    end

%+++++

```

```

%Dagan flow case
dp_over_dl =
(mu_o*Q_0)/(D_h^3)*(128/(pi*D_h)+24/t_or+(2*(1-
mu_i/mu_o)*(D_h^3))/(w_or*h*r_c*t_or))-
(ST_r_c*tan(theta_c_soluti on/2))/(t_or*r_c);

%-----

FLOW_DELTA_P_D =
((pi*(r_c*sin(theta_c_soluti on))^4)*dp_over_dl)/(8*mu_i);
%STILL HP

    FLOW_EFF_D = FLOW_PLUG + FLOW_DELTA_P_D;

    if FLOW_ACTUAL < FLOW_EFF_D
        PHYSICAL_FLOW_D = 1;
    elseif FLOW_EFF_D < 0
        PHYSICAL_FLOW_D = 2;
    else
        PHYSICAL_FLOW_D = 0;
    end

%+++++

%Estimate rate of surfactant removal
rate_of_surf_removal =
2*pi*r_c*sin(theta_c_soluti on)*max_gamma*(2.14*Q_0/(w_or*h)
);

%Rate of surfactant in
surf_rate_in = C_inf*Q_0*flow_ratio;

%+++++

SOLUTIONS1 = r_c;
% Cut off Radius
SOLUTIONS2 = theta_c_soluti on;
% Cut off Angle
SOLUTIONS3 = BCS;

```

```

% Dimensionless Concentration
SOLUTIONS4 = DES;
% Dimensionless Flowrate
SOLUTIONS5 = ijk;
% if 1, ST < R*T*gamma_inf (Set to R*T*gamma_inf)
SOLUTIONS6 = N_needed;
% Moles needed to create profile (From Isotherm)
SOLUTIONS7 = N_abs;
% Moles that can adsorb in set time period
SOLUTIONS8 = P_thread_minus_P_Cone_tau_0;
SOLUTIONS9 = P_thread_minus_P_Cone_tau_HP;
SOLUTIONS10 = 1;
SOLUTIONS11 = Delta_P_outside_t_0;
SOLUTIONS12 = Delta_P_outside_t_HP;
SOLUTIONS13 = 1;
SOLUTIONS14 = FLOW_EFF_0;
SOLUTIONS15 = FLOW_EFF_HP;
SOLUTIONS16 = FLOW_EFF_D ;
% Flow rate for v_interface*pi*r_c^2
SOLUTIONS17 = PHYSICAL_FLOW_0;
% 1 if Plug Flow is greater than actual flow
SOLUTIONS18 = PHYSICAL_FLOW_HP;
SOLUTIONS19 = PHYSICAL_FLOW_D;
SOLUTIONS20 = max_gamma_grad;
SOLUTIONS21 = rate_of_surf_removal;
SOLUTIONS22 = surf_rate_in;
SOLUTIONS23 = Percent;
clc

%Report Solutions
%Separate print function needed for par for loop
printsol (SOLUTIONS1, SOLUTIONS2, SOLUTIONS3, SOLUTIONS4, SOLUTIONS5, SOLUTIONS6, SOLUTIONS7, SOLUTIONS8, SOLUTIONS9, SOLUTIONS10, SOLUTIONS11, SOLUTIONS12, SOLUTIONS13, SOLUTIONS14, SOLUTIONS15, SOLUTIONS16, SOLUTIONS17, SOLUTIONS18, SOLUTIONS19, SOLUTIONS20, SOLUTIONS21, SOLUTIONS22, SOLUTIONS23, thedate);

%=====

```

```

catch ME
%If no solution exists for cone angle
%clc
%Cone angle violates physical bound
%Signals model to move onto next set of conditions
display(ME.message);
end
    end
end

%Plot Results
NEWSOLUTIONS =
load(['UNBD_SOLUTIONS_C12E8_', thedate, '_Surfoverlap.txt']);

PLOT_SOLUTIONS = [NEWSOLUTIONS(:, 4), NEWSOLUTIONS(:, 3)];

loglog(PLOT_SOLUTIONS(:, 1), PLOT_SOLUTIONS(:, 2), 'b*');
xlabel('DES')
ylabel('BCS')

axis([1*10^(min_DES), 1*10^(max_DES), 1*10^(min_BCS),
1*10^(max_BCS)])

%End Timer
toc

%New Scrip Function

function
[mu_o, mu_i, delta_mu, a, b_orf_hw, w_or, R, T, gamma_inf, kappa, n, h
, ST_0, z, D_h, flow_ratio, w_c, gamma_EQ_Scale, beta, t_or] =
getvariables

%Define all variables
mu_o = 0.04; %Pa*s
mu_i = 0.001; %Pa*s
delta_mu = mu_o - mu_i; %Pa*s
a = 94e-6; %m

```

```

%a = 60e-6 ;
b_orf_hw = 15e-6; %m
w_or = 38e-6; %m
h = 141e-6; % m
% w_or = 85e-6;
% h = 205e-6; % m
%s = 211e-6; %m
R = 8.314; %J/(mol *K)
T = 295; %K
gamma_inf = 2.25e-6; % mol/m^2
kappa = 10.3; %Dimensionless
n = 0.46; %Dimensionless
ST_0 = 0.050; % N/m actually ST_0 = 0.062
z = 190e-6; % m
D_h = 2*w_or*h/(w_or+h); %hydraulic diameter m
w_c = 285e-6; %m
flow_ratio = 1/40; % Dimensionless Q_inner/Q_outer
%gamma_EQ_Scale = 0.008;
gamma_EQ_Scale = R*T*gamma_inf;
beta = 22.1; % m^3/(mol *s)
t_or = 30e-6; %orifice thickness %m

%New Scrip Function

function [N_needed,ijk, max_gamma_grad, max_gamma] =
N_needed_fun2_mod(theta_c, DES, Flow_Factor)

%Number of discretized locations on interface
Points = 500;

%Get variables
[mu_o, mu_i, delta_mu, a, b_orf_hw, w_or, R, T, gamma_inf, kappa, n, h
, ST_0, z, D_h, flow_ratio, w_c, gamma_EQ_Scale, beta, t_or] =
getvariables;

%Initialize solution matrix
PLOT_ST = zeros(Points, 1);
PLOT_R = zeros(Points, 1);

```

```

PLOT_Gamma = zeros(Points, 1);
gamma_grad = zeros(Points, 1);
%Flow_Factor = 1;

%Determine cut off
r_c = ((a/tan(theta_c) - z - b_orf_hw) / cos(theta_c));

%Length of interface
s = a/sin(theta_c);

%Geometric discretization
matrix_r = linspace(r_c, s, Points);

%Determine flow rate
Q_0 =
(DES*gamma_EQ_Scale*z*D_h^3) / (20/3*flow_ratio*mu_o*a^2*(1-
w_or/(2*w_c))); % m^3/s %I <3 Nichole

ijk = 0;

%Step Size
dr = matrix_r(2) - matrix_r(1);

for j = 1:length(matrix_r)
    r = matrix_r(j);

%Find Coverage as a function of r
ST_r = ST_0 -
((3*delta_mu*Flow_Factor*Q_0*r_c^2*sin(theta_c)*cos(theta_c)
)*(1/r^2 - 1/s^2)) / (w_or*h*(3*(cos(theta_c))^2 - 1));

%Determine if surface tension goes too low
    if ST_r < 0.005
        ST_r = 0.005;
        ijk = 1;
    end

    try
%Find Surface coverage from interfacial EOS

```

```

    gamma_new = fzero(@(gamma) (log(1-gamma/gamma_inf) -
kappa*n/(n+1)*(gamma/gamma_inf)^(n+1) - (ST_r-
ST_0)/(R*T*gamma_inf)), [0, 0.9999999999999999*gamma_inf]);
    catch NONE
    gamma_new = 0;
    end

    PLOT_ST(j) = ST_r;
    PLOT_R(j) = r;
    PLOT_Gamma(j) = gamma_new;

    if j==1
    gamma_grad(j) = 0;
    else
    gamma_grad(j) = (PLOT_Gamma(j-1) - gamma_new)/dr;
    end
end

%Find max coverage
max_gamma = max(PLOT_Gamma);
max_gamma_grad = max(gamma_grad);

%Integrate interfacial coverage profile
N_needed =
trapz(2*pi *PLOT_Gamma. *PLOT_R*sin(theta_c) *(matrix_r(2) -
matrix_r(1)));

```